STARS

University of Central Florida
STARS

Electronic Theses and Dissertations, 2004-2019

2018

Multi-Scale Fluid-Structure Interaction Model Analysis of Patient-Specific Geometry for Optimization of LVAD Outflow Graft Implantation: An Investigation Aimed at Reducing Stroke Risk

Ray Prather
University of Central Florida

 Part of the Mechanical Engineering Commons
Find similar works at: https://stars.library.ucf.edu/etd
University of Central Florida Libraries http://library.ucf.edu

This Doctoral Dissertation (Open Access) is brought to you for free and open access by STARS. It has been accepted for inclusion in Electronic Theses and Dissertations, 2004-2019 by an authorized administrator of STARS. For more information, please contact STARS@ucf.edu.

STARS Citation
Prather, Ray, "Multi-Scale Fluid-Structure Interaction Model Analysis of Patient-Specific Geometry for Optimization of LVAD Outflow Graft Implantation: An Investigation Aimed at Reducing Stroke Risk" (2018). *Electronic Theses and Dissertations, 2004-2019*. 5829.
https://stars.library.ucf.edu/etd/5829

MULTI-SCALE FLUID-STRUCTURE INTERACTION MODEL ANALYSIS OF PATIENT-SPECIFIC GEOMETRY FOR OPTIMIZATION OF LVAD OUTFLOW GRAFT IMPLANTATION: AN INVESTIGATION AIMED AT REDUCING STROKE RISK

by

RAY OTTO PRATHER
B.S. University of Central Florida, 2013
M.S. University of Central Florida, 2015

A dissertation submitted in partial fulfillment of the requirements
for the degree of Doctor of Philosophy
in the Department of Mechanical and Aerospace Engineering
in the College of Engineering and Computer Science
at the University of Central Florida
Orlando, Florida

Spring Term

2018

Major Professor: Alain Kassab

© 2018 Ray Otto Prather

ABSTRACT

A Left Ventricular Assist Device (LVAD), is a mechanical pump capable of providing circulatory myocardium relief when used as bridge-to-transplantation by reducing the workload of a failing heart, with the additional bonus of allowing for cardiac recovery when used as destination therapy. The newer generations of continuous flow VADs are essentially axial or radial flow pumps, and while these devices are capable their efficiency depends upon fluid composition and flow field patterns. The most devastating complication of VAD therapy is caused by embolization of thrombi formed within the LVAD or inside the heart into the brain leading to stroke. Anticoagulation management and improved LVADs design has reduced stroke incidence, however, investigators have recently reported the incidence of thromboembolic cerebral events is still significant and ranges from 14% to 47% over a period of 6-12 months [1, 2]. Blood clots may cause obstruction of critical vessels, such as cerebral arteries, reducing brain oxygenation and resulting in devastating consequences like major neurocognitive malfunction and complications which can be fatal.

The hypothesis that incidence of stroke can be significantly reduced by adjusting the VAD outflow cannula implantation to direct dislodged thrombi away from the cerebral vessels has been recently supported by a series of steady flow computations assuming rigid vessel walls for the vasculature. Such studies have shown as much as a 50% reduction in embolization rates depending on outflow cannula implantation [3, 4, 5, 6]. In this study, a pulsatile fully compliant vessel wall model is developed to further establish this hypothesis. A time-dependent multi-scale Eulerian Computational Fluid Dynamics (CFD) analysis of patient-specific geometry models of the VAD-bed vasculature is

coupled with a 3D Finite Element Analysis (FEA) of the mechanical response of the vascular walls to establish the VAD assisted hemodynamics. A Lagrangian particle tracking algorithm is used to determine the embolization rates of thrombi emanating from the cannula or other possible thrombogenic locations such as the aortic root. This multiscale Eulerian-Lagrangian pulsatile fluid-structure coupled paradigm allows for a fully realistic model of the hemodynamics of interest.

The patient-specific geometries obtained from CT scan are implemented into the numerical domain in two modes. In the 3D CFD portion of the problem, the geometry accounts solely for the flow volume where the fluid is modelled as constant density and non-Newtonian under laminar pulsatile flow conditions. The blood-thrombus ensemble in treated as a two-phase flow, handled by an Eulerian-Lagrangian coupled scheme to solve the flow field and track particle transport. Thrombi are modelled as constant density spherical particles. Particle interactions are limited to particle-to-wall and particle-to-fluid, while particle-to-particle interaction are neglected for statistical purposes. On the other hand, with the help of Computer Aided Design (CAD) software a patient-specific aortic wall geometry with variable wall thickness is brought into the numerical domain. FEA is applied to determine the aortic wall cyclic displacement under hydrodynamic loads. To properly account for wall deformation, the arterial wall tissue incorporates a hyperelastic material model based on the anisotropic Holzapfel model for arteries. This paradigm is referred to as Fluid Structure Interaction (FSI) and allows structural analysis in conjunction with flow investigation to further monitor pathological flow patterns. The FSI model is driven by time dependent flow and pressure boundary conditions imposed at the boundaries of the 3D computational domain through a 50 degree of freedom 0D lumped

parameter model (LPM) electric circuit analog of the peripheral VAD-assisted circulation.

Results are presented for a simple vessel model of the ascending aorta to validate the anisotropic fiber orientation implementation. Arterial wall dilation is measured between 5-20% in the range reported in literature. Hemodynamics of the VAD assisted flow in a patient-derived geometry computed using rigid vessels walls are compared to those for a linearly elastic vessel wall model and a hyperelastic anisotropic vessel wall model. Moreover, the thromboembolization rates are presented and compared for pulsatile hemodynamics in rigid and compliant wall models. Pulsatile flow solutions for embolization probabilities corroborate the hypothesis that tailoring the LVAD cannula implantation configuration can significantly reduce thromboembolization rates, and this is consistent with indications from previous steady-flow calculations.

ACKNOWLEDGMENTS

I thank my advisor Dr. Alain Kassab, and my collaborator Dr. William DeCampli for their guidance and support throughout this project. For their combined extensive understanding of fluid mechanics, numerical methods, medical knowledge and intuition proved to be of great help.

I dedicate my hard work to the undying support of my father and mother, who relentlessly sustained me.

The great assistance provided by Steven Dick in handling the computer cluster and support in generating the codes to facilitate simulations.

I thank my collaborator, Dr. Marcus Ni, for his assistance in programming and troubleshooting codes.

TABLE OF CONTENTS

LIST OF FIGURES

LIST OF TABLES

LIST OF ABBREVIATIONS/ACRONYMS

AO	Ascending Aorta
BC	Boundary Condition
C	Capacitance
CAD	Computer Aided Design
CFD	Computational Fluid Dynamics
CS	Coordinate System
DA	Descending Aorta
EDV	End-Diastolic Volume
EF	Ejection Fraction
ESV	End-Systolic Volume
DEM	Discrete Element Method
DOF	Degrees Of Freedom
FEA	Finite Element Analysis
FEM	Finite Element Method
FSI	Fluid Structure Interaction
HF	Heart Failure
HHT	Hilber-Hughes-Taylor
HR	Heart Rate
L	Inductance
LCA	Left Carotid Artery
LCOR	Left Coronary Artery
LPM	Lumped Parameter Model

LSA	Left Subclavian Artery
LVAD	Left Ventricular Assist Device
LVERT	Left Vertebral Artery
MI	Myocardial Infarction
R	Resistance
RCA	Right Carotid Artery
RCOR	Right Coronary Artery
RSA	Right Subclavian Artery
RVERT	Right Vertebral Artery
SPL	Space Conservation Law
STK	Stokes Number
WSS	Wall Shear Stress

1 CHAPTER: INTRODUCTION

1.1. Introduction

Among all possible malfunctions of bodily organs, heart failure, a condition wherein cardiac output cannot satisfy corporal requirement, is the most disconcerting. Dependent upon the condition of the heart, a by-pass is one consideration. In extremis, transplant becomes the best probable solution. Donor compatibility is necessary in order for this procedure to be successful leading to long wait times while seeking donor compatibility and availability. In such cases, a Ventricular Assist Device (VAD) can be implemented as a bridge to transplantation (Figure 1, 2). Continuous axial or radial flow pumps have shown to be a promising and durable destination therapy. Depending on the workload they almost entirely nullify pulsatile effects, which have been a major cause to thrombo-embolism. In addition, VADs have been effectively employed to enable myocardial recovery. While Ventricular Assist Devices are capable, their efficiency depends upon fluid composition and flow mechanics, and despite improved device design and anti-coagulation treatment, a patient is likely to suffer a thrombo-embolism within a 6 month to a one-year period.

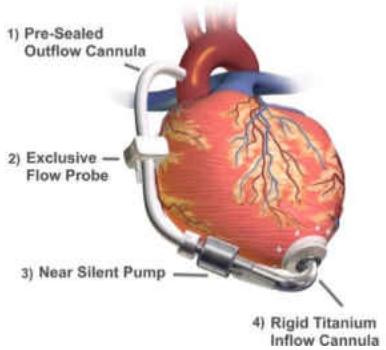

Figure 1 - LVAD implantation curtesy of http://blausen.com/.

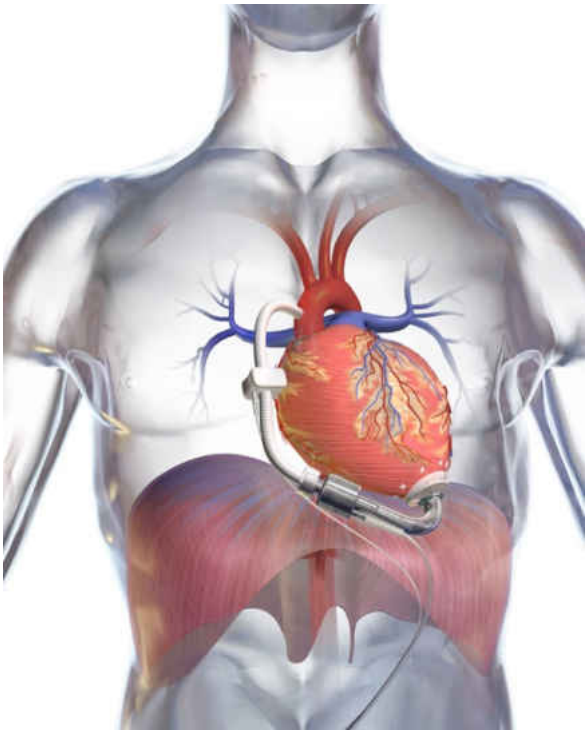

Figure 2 - LVAD implantation schematic curtesy of http://blausen.com/.

The hypothesis that incidence of stroke can be significantly reduced by adjusting the VAD outflow cannula implantation to direct dislodged thrombi away from the cerebral vessels has been recently supported by a series of steady flow computations assuming rigid vessel walls for the vasculature. Such studies have shown as much as a 50% reduction in embolization rates depending on outflow cannula implantation [1, 2].

1.2. Vascular Diseases

In this study, several different types of vascular diseases are investigated. Heart failure is the prime cause for the LVAD implantation which may carry health risks associated with the host's thermogenic response: namely stroke and myocardial infarction. Notably, deep vein thrombosis may also be cause for concern, however it will not be subjected to scrutiny in this endeavor.

1.2.1. Heart Failure

Heart failure (HF) occurs when the heart is unable to provide sufficient blood flow output to satisfy corporeal requirements. This condition, diagnosed by physical examination, is confirmed by echocardiography. Causes include may include heart attack, hypertension, valvular heart disease and cardiomyopathy. In general, it is possible to quantify heart failure by means of Ejection Fraction (EF), which simply relates the stroke volume (SV) to the end-diastolic volume (EDV) and end-systolic volume (ESV) as in Equation 1**.**

$$EF(\%) = \frac{SV}{EDV}100 \tag{1}$$

$$SV = EDV - ESV \tag{2}$$

A typical healthy patient has values ranging from 50 – 70 %. An EF below this range represents a state of cardiomyopathy. An individual's EF tends to decrease gradually due to aging, as the heart's efficiency tends to decrease. In fact, HF is the leading cause of hospitalization for subject of 65 years of age and older. However, impaired EF or a sharp inefficiency are consistent indicators of heart failure. A VAD device is usually implemented in this case to support the workload and supply the appropriate amount of blood to regulate bodily functions.

1.2.2. Stroke

There are essentially two types of stoke which are accountable for the majority of fatalities, ischemic strokes and hemorrhagic strokes (Figure 3). The first is the subject of this study and is due to vessels occlusion. The latter is caused by vessel rupture (may be

due to tissue weakening or excessive mechanical loads) leading to blood leaking and pooling in critical areas.

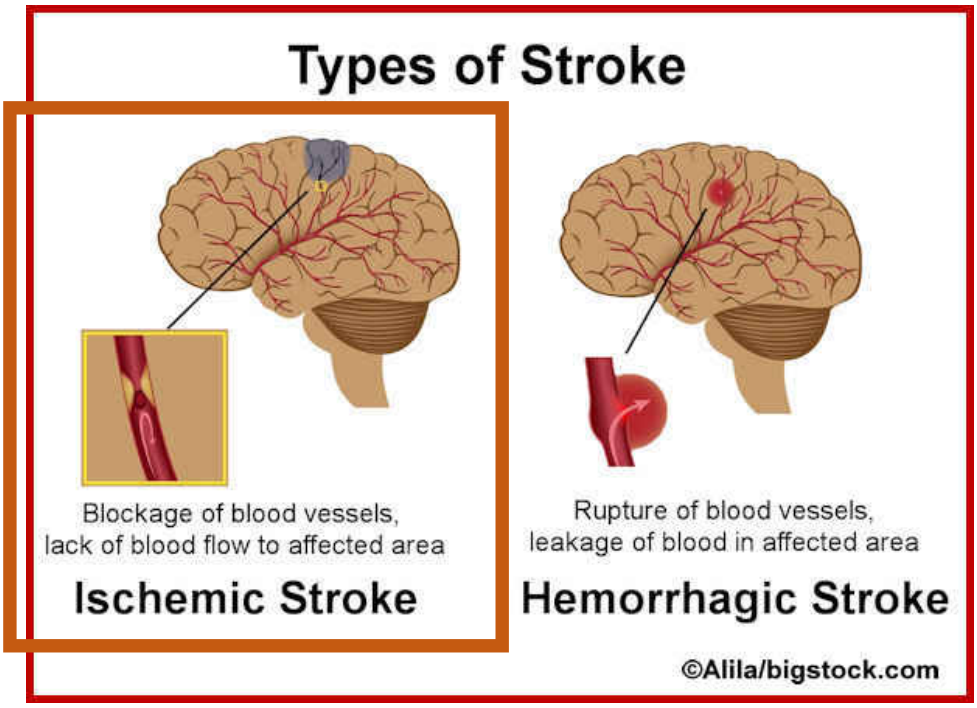

Figure 3 - Types of stroke.

Blood clotting, an essential occurrence for homeostasis is a normal process, but vessel deterioration and tissue malfunction can induce undesirable clotting, which may result in stroke, embolism or heart attack. Thrombi generate in two ways: rupture from arteriosclerotic plaques or coagulated masses and fatty deposits dislodged from implanted devices such as VADs (Figure 4).

Thrombus formation in the inflow conduit of a MicroMed DeBakey VAD.

Thrombus formation around the impeller of an exchanged MicroMed DeBakey VAD.

Figure 4 - Blood cloths generation by arteriosclerotic plaques and blood cloths [7].

Thrombi generated by either mechanism and that obstruct flow in key vessels can be fatal. A subject can suffer a stroke in which case cerebral vessels have been occluded or a heart attack in which case coronary flow is hindered. In depth understanding of both cases reveals specific flow patterns in regions of branching, bends, recirculation, and low flow. A detailed flow analysis could help optimizing the implementation of VADs to reduce chances of stroke caused by thrombosis.

1.2.3. Myocardial Infarction

Myocardial infarction (MI), referred also as a heart attack, occurs when blood supply to a part of the heart is hindered, causing local heart tissue damage (Figure 5). The condition most commonly presents symptoms such as chest pain or discomfort which may travel into the shoulder, arm, back, neck, or jaw. Typically, the mechanism of an MI involves the occlusion of a coronary vessel caused by either the rupture of an atherosclerotic plaque or, in the case of a patient implanted with an LVAD, the

occlusion may be caused by a dislodged thrombus originating from the VAD itself, VAD outflow graft, the left ventricle, the aortic root or other potential thrombogenic sites.

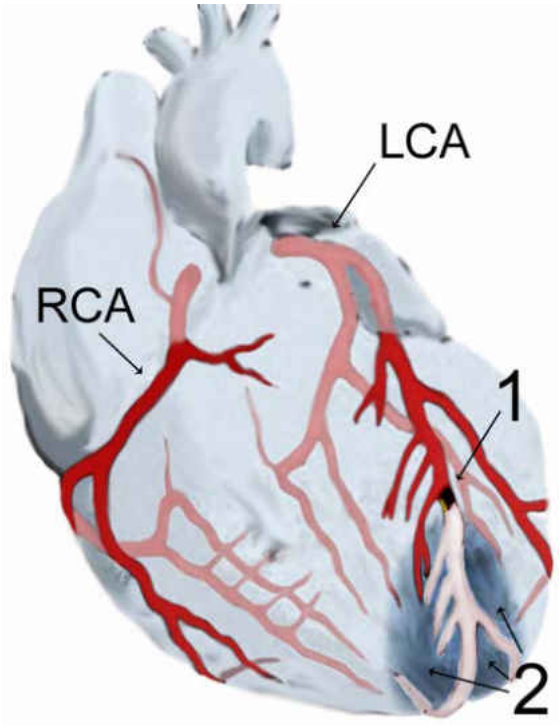

Figure 5 - Diagram displaying blockage of a branch of the Left Coronary Artery (LCA) causing muscle tissue death (by J. Heuser JHeuser - Own work, CC BY-SA 3.0, https://commons.wikimedia.org/w/index.php?curid=878493).

2 CHAPTER: LITERATURE REVIEW

Recently, new concerns have been raised regarding thromboembolisms in VAD patients as reported in two large studies published in 2014 in The New England Journal of Medicine [8] and The Journal of Heart and Lung Transplantation [9]. According to clinical data, continuous flow VAD pumps have a higher thrombus incidence rate than previously recorded. Moreover, it has been reported from clinical studies that cannula implantation configurations play a major role in VAD thromboembolic events [10, 11], as suggested by previous studies from our group [3, 4, 5, 6]. A large Intermacs study reports in 2017 that thrombosis persists as a critical problem in VADs [12]. This compels additional research effort dedicated to study the root causes of this phenomenon as well as possible surgical solutions that may reduce stroke risk in VADs.

Given the current rate of cerebral thromboembolism in the VAD patient population, this dissertation investigates a practical preventive measure: a deliberate surgical manoeuver whereby the VAD outflow graft (VAD-OG) implantation is optimally positioned so as to redirect thrombi along the aortic arch such that the rate of thromboembolism to the cerebral vascular supply (carotid and vertebral arteries) is significantly reduced. Simple but intentional adjustment to the VAD-OG may serve to be just as fundamental as anticoagulation measures and advancements in pump design in order to reduce overall risk of stroke in the long-term VAD recipient. Decreasing the risk of stroke would benefit every patient with a VAD. As VAD technology improves the prevalence of VAD therapy could potentially increase to include most of the 250,000 patients in end stage heart failure.

Previous work carried out by our research group, employing steady flow Computational Fluid Dynamics (CFD) analysis have indicated that reduction of stroke incidence can vary by as much as 50%, upon varying cannula implantation configurations [3, 4, 5, 6]. Follow-up work by the author successfully performed a multi-scale CFD simulation for 2 different LVAD implantation configurations on patient-specific geometries showing variance of cerebral embolization rates [13].

A large portion of research conducted on cardiovascular system typically focuses on very specific topics such as tracing the origin and transport of thrombi in the cardiovascular system [14, 15] or determine qualitative and quantitative characteristics of flow patterns induced by the implantation of VADs [14, 16]. For a long period of time, the notion of shear stress as indicator for platelet activation dominated the literature and many research groups focused on modeling particle-to-particle interaction at the platelet level to induce clusters in a region removed from the vessel walls. In more recent studies, it was observed however that not only this threshold spans over a large range but that also such large values that rarely occur in the flow region outside of the boundary layer. In addition, computational efforts involving CFD to track shear stress fields in rigid vessel structures have been shown to provide significant overestimates due to the strong interaction between the fluid and the solid wall [17]. In fact, these new studies found near vessel wall dynamics to be more significant and lead investigators to focus on tracking transport of a molecule which activates thrombin largely responsible for the thrombogenic cascade. In doing so, potentially thrombogenic locations along the vessel wall can be identified. Along with thrombus origin, thrombus transport should be modelled as well. From a macroscopic perspective, a multi-phase flow must have a series of constraints

and relations which regulate the interaction between phases. Traditionally for any Eulerian-Lagrangian coupling, drag and lift are accounted having gravity as an additional variable and the particulate dynamically interacts with the solid boundaries based on either energy dissipation or restitution coefficients. However, for a larger number of particulate phase, an additional modelling scheme is available to track and modulate how particle interact among them, The Discrete Element Model (DEM). The DEM model makes available various approaches based on viscous damping where the particles are modeled based on a viscoelastic model or based on restitution coefficients for both the normal and tangential direction. These models differ in computational expenses as well as in their ability to handle a large number of particle. The viscous model carries out integrations based on the energy equation which for a large number of particles becomes very expensive. Often in literature it is preferred to prescribe a range of restitution coefficients [15]. On the other hand, blood is known to be a multi-phase fluid having shear-thinning properties. However, depending on the scale of the study and to save computational resources, in various studies it has been and it still is being modeled as a Newtonian fluid having constant viscosity. This approximation does not allow to fully characterize localized flow patterns which may be pathological and would require closer inspection. A variety of models have been developed to essentially curve fit clinical data relating shear rate to viscosity and implement the relationship in computational software. As such these efforts bring forth a great variety of different modeling techniques allowing detailed description of phenomena which were previously poorly understood. However, these efforts are examples of studies that have very strict constraints dictated by the modeling techniques themselves and computational power forcing, the investigators to

only characterize localized events. In our study, we aim at building model which takes into account all these observations to predict thormbo-embolic events on a patient-specific base. This effort will result in a model capable of accurately represent localized flow patterns, compute a multi-phase flow solution, track thrombus transport with wall-to-particle, particle-to-particle interaction and wall compliance. In addition, a comparison to previous result obtained from steady and unsteady flow conditions with rigid wall will establish the degree of modeling required to accurately and consistently predict thrombo-embolizations rates. Such inferences may affect the computation expenses required to carry out other studies of similar nature.

An additional feature of this study includes aortic wall compliance in response to loads applied at the fluid interface. From a physiological perspective, this region presents a multi-layered tissue with fiber driven mechanical properties requiring a model centered on the mechanics of fiber-reinforced composites theory. In order to represent the hyperelastic behavior of the great aortic vessels the Holzapfel-Gasser-Ogden model is adopted. This model utilizes the same blended strain-energy function for each layer which accounts for isotropic properties due to non-collagenous matrix and anisotropic properties for orientated collagenous fibers [18, 19]. As mentioned, the inclusion of vessel wall compliance will adjust previous near wall measurements to be more accurate and realistic.

The coupling of the fluid domain and the solid domain form a paradigm know as Fluid Structure Interaction (FSI) that allows for the structural analysis of the solid response to loads interface applied by the fluid at the interface. This degree of modelling could provide for more accurate thrombus tracking scheme.

3 CHAPTER: METHODS

3.1. Preliminary Studies

Previous work by the authors [13, 20] successfully carried out a multi-scale CFD simulation for 2 different LVAD implantation configurations on patient-specific geometries obtained from CT scans utilizing the 0-D LPM of the VAD and circulatory system to generate requisite waveform boundary conditions supplied to the 3-D CFD of a patient-specific aortic arch-VAD bed geometry (Figure 6).

Figure 6 - Patient specific geometries investigated showing two different angle of outflow cannula implantation.

Preliminary runs revealed attempts to introduce pulsatility to be successful, as flow parameters such as pressure and flow rates retain physiological fidelity and respect prescribed flow requirements. The model also proved to be rather adjustable to user-desired conditions and geometries, making the process readily available for future medical research and as an aid to treatment planning.

The research undertaken in this dissertation builds upon previous work by the authors and addresses the following three aims:

1) Implement Lagrangian thrombus transport model in the multi-scale fluid-structure CFD model and introduce thrombi particles of an expected range of sizes and randomized time at the inlet plane of the cannula and carry out statistical analysis of stroke.
2) Explore design space computationally by considering: (a) cannula angle of implantation relative to ascending aorta, (b) distance of the conduit from the take-off of the innominate, and (c) location along the coronal plane. Test various implantation configurations of the LVAD outflow cannula under pulsatile conditions.
3) Carry out the analysis for risk for several patient-specific geometries, establishing that there is a statistically significant reduction in incidence of stroke under pulsatile conditions under multi-scale CFD determined optimal configuration for each patient-specific model.
4) The de-identified CT scans utilized in this study are provided by our medical partners at OrlandoHealth, and solid models were rendered using the MIMICS medical segmentation software (Materialize, Leuven, Belgium).

In previous studies blood was modelled as Newtonian fluid (with constant density) which has been taken as an accepted approximation for the majority of studies that were reported in the literature. However, for completeness in this investigation, the blood model

will be updated to account for the non-Newtonian rheology of blood, based on clinical data extracted from literature for strain rate versus viscosity (Figure 7) [16].

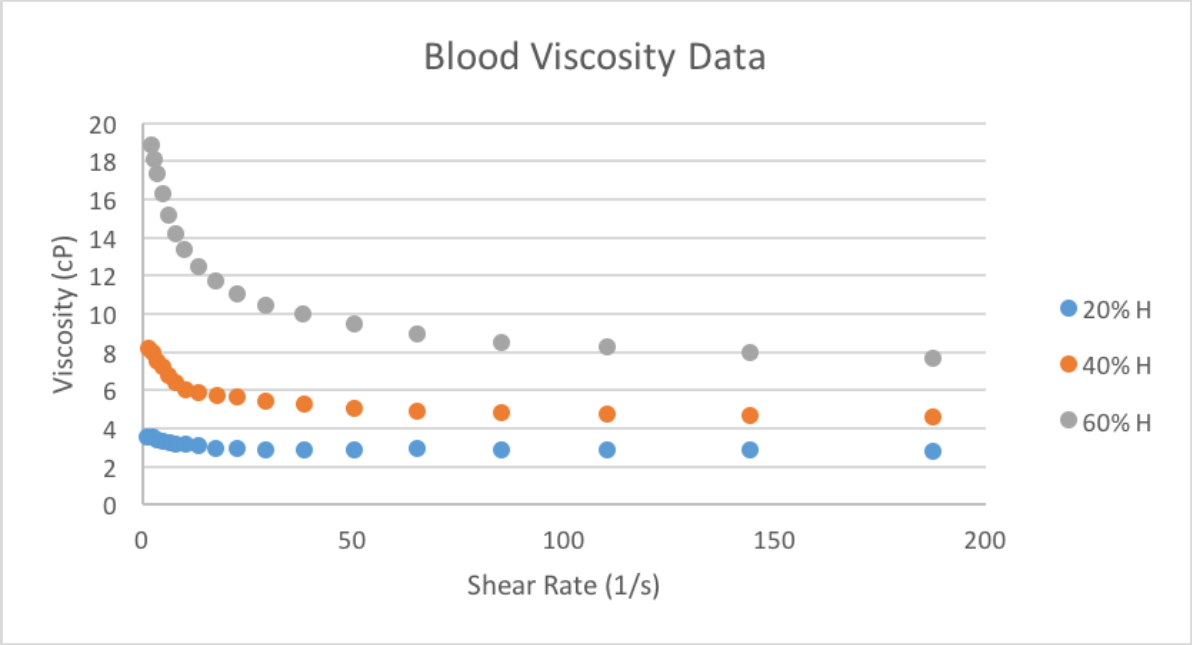

Figure 7 - Nonlinear viscosity relation based on hematocrit percentage [16].

Following existing methodologies outlining non-Newtonian modeling of blood and clinical data extrapolated from literature, we build our own 3-parameter model driven by hematocrit level based on the Carreau-Yasuda approach.

$$\mu(\dot{\gamma}) = \mu_\infty + (\mu_o - \mu_\infty)\frac{1}{[1+(\lambda\dot{\gamma})^2]^{\frac{1}{3}}} \tag{3}$$

where $\dot{\boldsymbol{\gamma}}$ is the shear rate that is evaluated in terms of the invariants of the deformation tensor, $\boldsymbol{\mu_\infty}$ is the free-stream viscosity, $\boldsymbol{\mu_o}$ is the near-wall viscosity and $\boldsymbol{\lambda}$ is the time-relaxation parameter. Depending on the hematocrit level each constant was computed by

mean of the least squares method using a MatLab script found in Appendix A, and these are compiled in the following table.

Table 1 - Tabulated constants obtained from curve fitting Carreau-Yasuda model.

Hematocrit [%]	μ_∞ [cP]	μ_o [cP]	λ [s]
20	2.7459	3.5832	-0.2783
40	4.3989	8.4248	0.3103
60	7.0151	19.8035	0.2646

This model will be implemented in our multi-scale problem for a 40% hematocrit level and will characterize the viscosity on a local level allowing for more precise statistical inferences. This displays the ability to implement a patient-specific blood model based on clinical data, when available. A large variety of blood disorders can potentially be simulated when necessary. This provides for a very dynamic modelling approach.

3.2. Methods

This research project is designed to be a multi-scale simulation which essentially combines a 0-D Lumped Parameter Model (LPM) of the circulatory system including the LVAD, which has been developed and tuned in previous studies, with a 3-D simulation where the fluid domain is coupled to the compliant vessel wall domain. There are essentially three phases to this study:

1) Iterate the multi-scale simulation to obtain converged solution for the flow fields;
2) Enable FSI coupling to generate initial deformed geometry and pre-stressed structure

3) Activate the Lagrangian particle tracking scheme and release particles in the domain;
4) Conduct statistical analysis to test a significant correlation between steady, unsteady and compliant unsteady models.

Due to the nature and complexity of the problem steps 2-3 are the most computationally expensive parts. In this study parallelization is required to make the solution achievable within a reasonable time reasonable.

3.3. Geometry Rendering

Geometries consist of patient specific models extracted from retrospective (de-identified) patient CT scans. The aortic arch (and major cerebral vessels) circulation geometry is gathered through CT scans. CT scan images are then converted to 3-D geometric solid models by propagating surfaces across each image. This is achieved by the combined use of 3-Matic© and Mimics© (Materialize, Leuven, Belgium). Mimics is a medical segmentation software specialized to permit this operation while 3-Matic is an advanced CAD software for capable of performing complex design operations on the rendered 3D solid model. This 3-D geometry is then used to model the fluid domain at the area of interest (Figure 8). The following vessels have been traced: ascending aorta, coronaries, common carotids, subclavian and vertebral (Appendix C: Figure 80). The LVAD inflow cannula has been then added using Solidworks (Dassault Systemes, Waltham, MA).

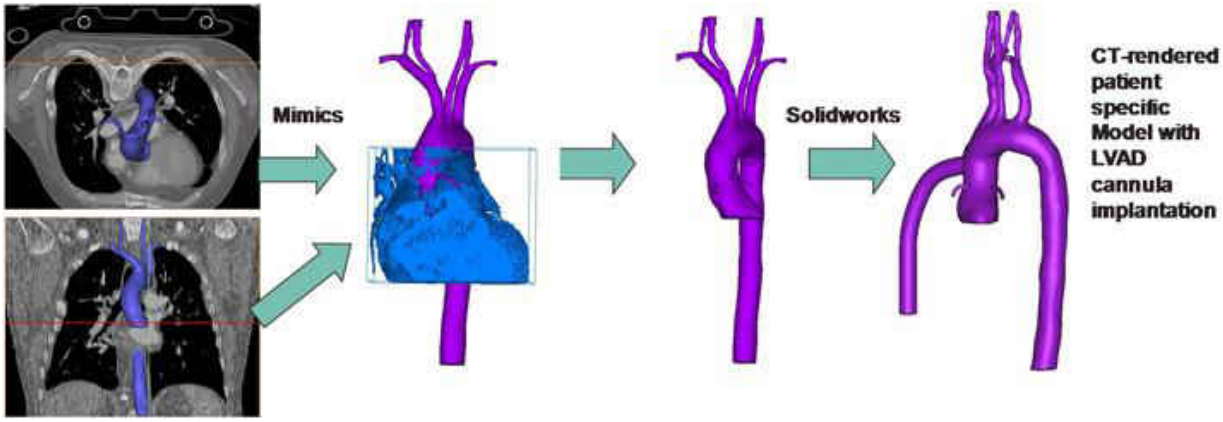

Figure 8 - Anatomy reconstruction procedure.

The process utilized to generate the aortic wall geometry to be imported into Abaqus is outlined in the schematic below. I required the combination of several separate CAD software aimed mainly at either creating a surface offset, generating a thickness volume and creating appropriate file formats.

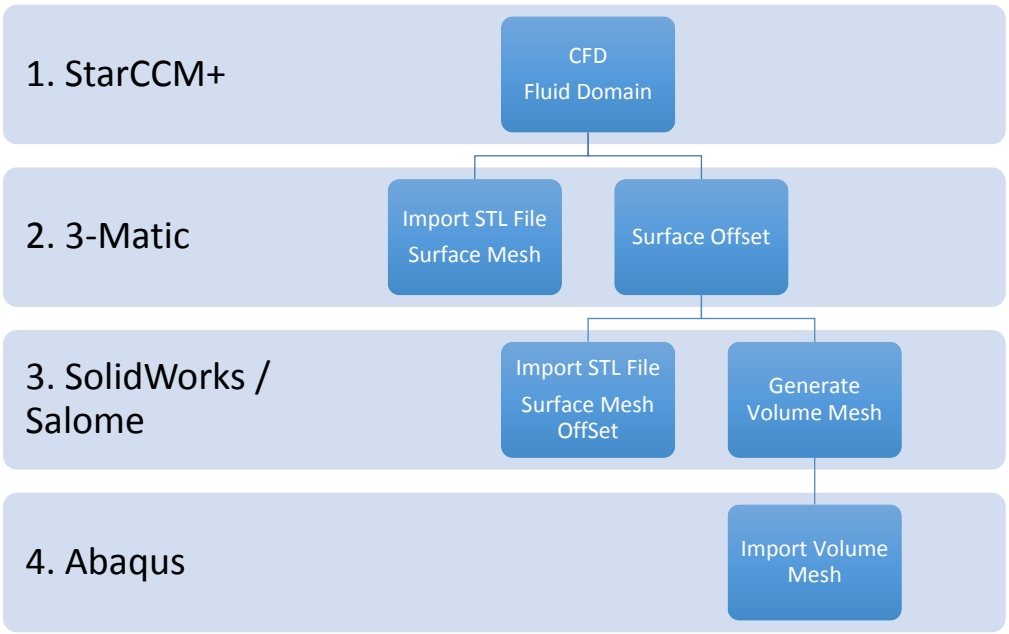

Figure 9 - Aortic wall rendering procedure schematic.

3.3.1. Step 1-2: from StarCCM+ to 3-Matic

Given the fluid domain generated from the anatomical reconstruction, the resulting STL carrying data on surface topology in imported in both Mimics and 3-Matic (Figure 11-a).

By a similar approach the wall geometry is generated. First by using Mimics, the centerline for each blood vessel is determined along with the hydraulic dimeter at discrete intervals along the vessel's centerline. This data is exported in the format of a CSV file from Mimics to 3-Matic. The data relative to hydraulic diameter data is then used to divide portions of the geometry were diameter has low variance, then selectively offset the original wall boundary surface (of the fluid domain) by 10% of the local computed hydraulic diameter (Figure 11-b, c). Figure 10 displays the computed average hydraulic diameter for each subsection accompanied by the relative standard deviation. Local surface offsets are then voided of poor features by wrapping the surface (Figure 11-d). Once all separate entities have been adjusted, they are combined into a global geometry. In order to obtain a smooth surface and eliminate any sharp transition between sections edge smoothing is employed which produces an optimal geometry ready to be imported in the FEA software (Figure 11-e). To avoid any sharp transition in mesh due to edge smoothing refinement (refines the local mesh) it may be sound to apply a final wrap onto the unified geometry. The most important surface in the geometry is the interface between the fluid and the solid, hence to limit the round-off error due to geometric Boolean operations the fluid volume is subtracted from the surface offset to ensure the interface is in fact correctly located. The sequence of this construction of the vessels is provided in Figure 11.

Hydraulic Diameter [mm]	
DA	
1	22.36±0.66
2	19.77±0.48
3	18.58±0.6
DA to LSA	
1	15.95±0.62
2	8.57±0.15
LSA	
1	4.86±0.44
L Vert	
1	4.1±0.19
2	4.92±0.29
3	3.91±0.17
LCA	
1	15.31±0.44
2	5.86±0.38
3	4.94±0.14
4	5.5±0.21
Innominate	
1	11.54±0.2
RCA	
1	4.93±0.2
2	6.28±0.35
RCA to RSA	
1	9.4±0.36
RSA	
1	5.62±0.48
R Vert	
1	4.1±0.12
2	3.92±0.19
LVAD to Innominate	
1	26.61±0.43
L Cor	
1	2.98±0.02
R Cor	
1	2.98±0.02
AO to Coronaries	
1	24.23±3.72

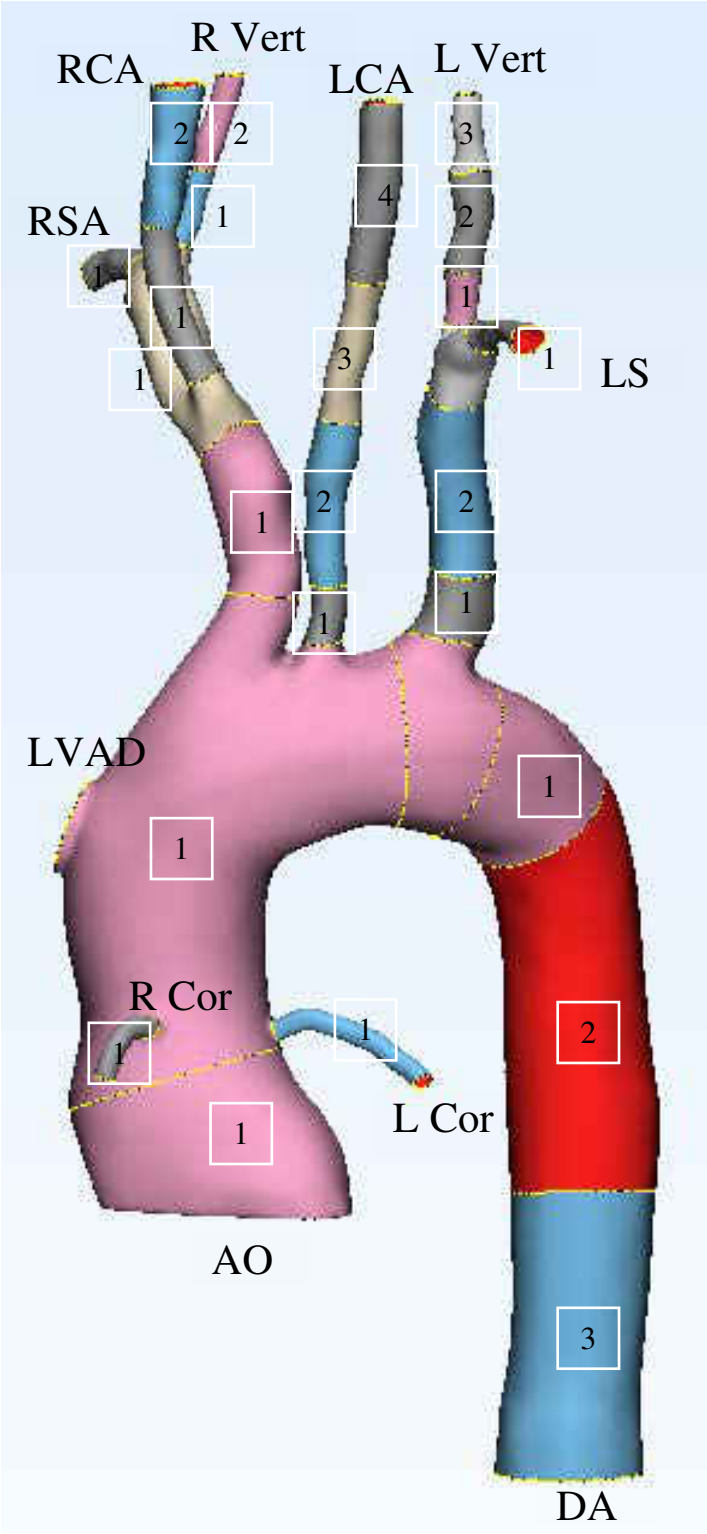

Figure 10 - Averaged hydraulic diameter data relative to local subsections.

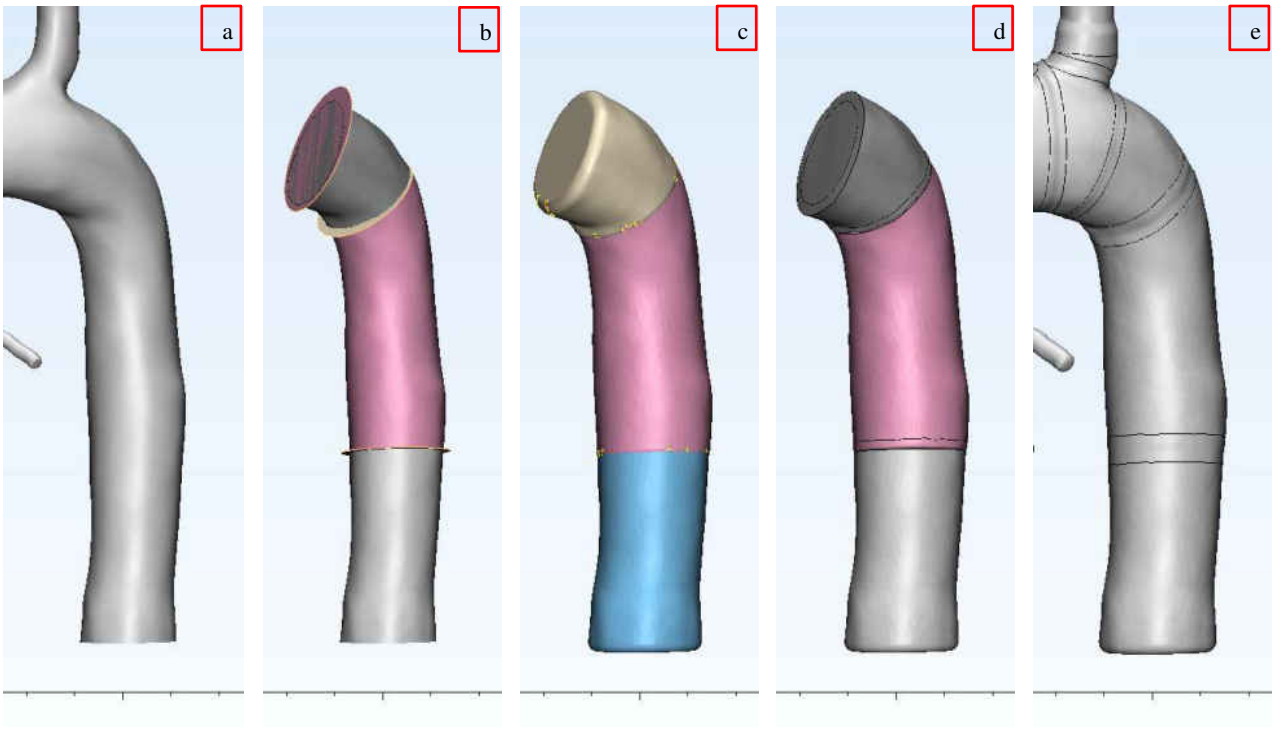

Figure 11 - Wall geometry construction sequence.

3.3.2. Step 3-4: SolidWorks (Salome) to Abaqus

The most desirable file format to be imported into the finite element method (FEM) commercial code Abaqus (Dassault Systemes, Waltham, MA) would be one which contains a volumetric representation of the geometry. However, the available version of 3-Matic the only export available is in the STL format which only provides the surface topology (as a surface-mesh). Hence intermediate step must be taken to generate a volume mesh from the given surface mesh.

The first option employs an open-source CAD software Salome (https://www.salome-platform.org/). Salome can import STL file and directly generate an arbitrary volume mesh to be exported in the form of a STEP or IGES files (well accepted by Abaqus). However, the computation expenses involved with this transition are directly

correlated to the surface mesh refinement. Fine meshes will take a very long time to be processed.

The second option is to import the STL into Solidworks and by means of the Scan to 3D tool reconstruct a viable surface. Once any gaps of surface intersections are healed, the internal volume can be filled by using the boss/base → Thicken tool which essentially detects a closed surface contour and fills it to become a solid. The solid body may now be exported in either STEP or IGES format to be finally imported into Abaqus (Figure 12).

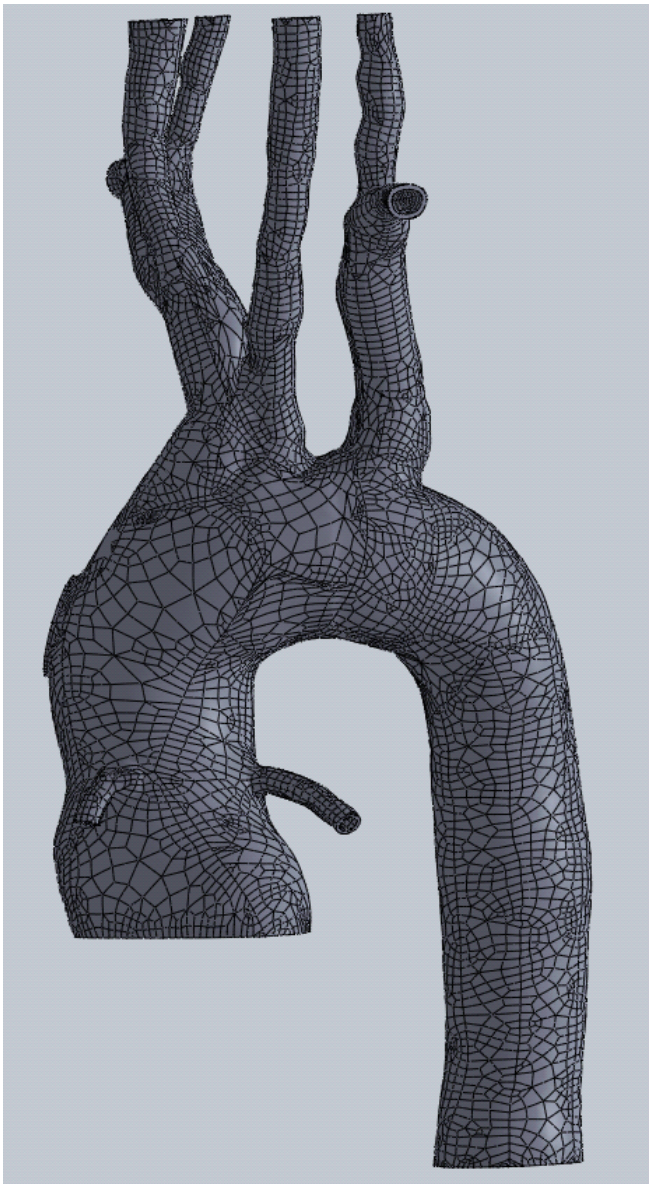

Figure 12 - SolidWorks finalized geometry.

To be noted, there is a likelihood that the walls generated by the outlined procedure present excessively fine tessellation which may become problematic when meshing into Abaqus. This can be overcome directly into the destination software by simply combing faces of each separate surface of interest (inner wall, interface wall and boundaries) using the Virtual-Topology tool (Figure 13).

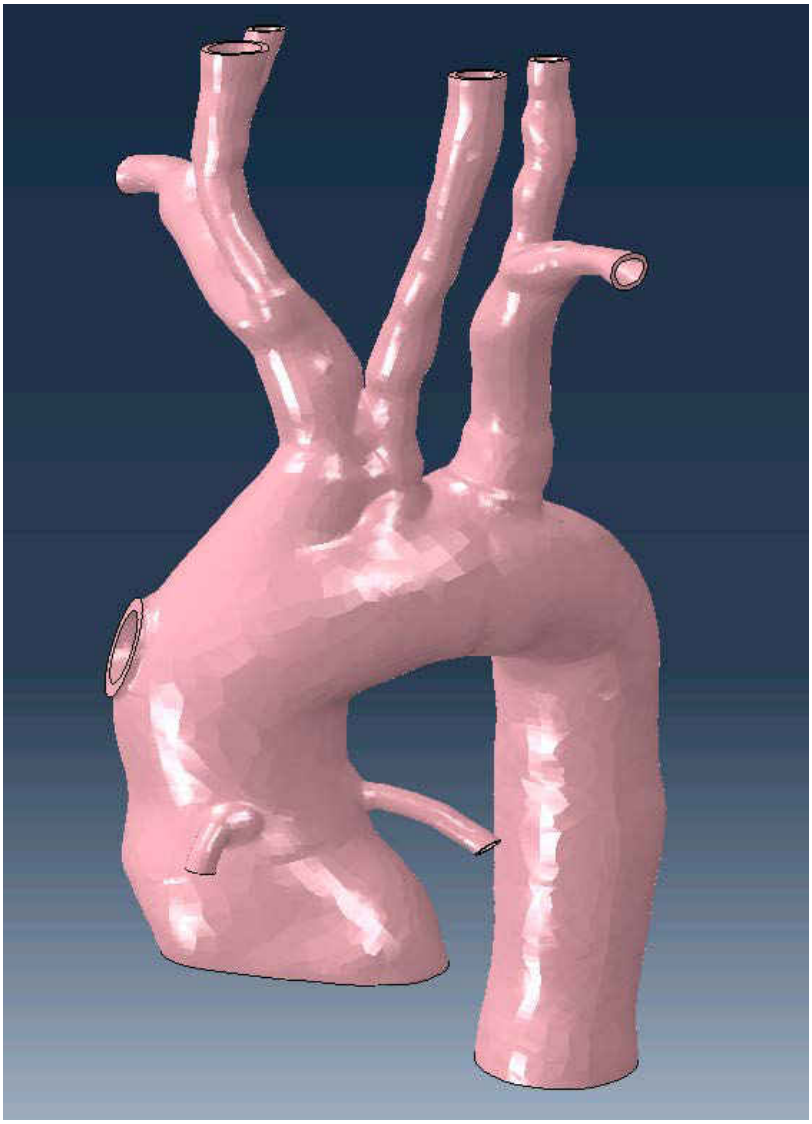

Figure 13 - Abaqus geometry post-surface treatment.

Once any trace of excessive tessellation has been eliminated from both inner and outer surface, meshing operations yield a very homogeneous tetrahedral mesh ideal for solid deformation (Figure 14).

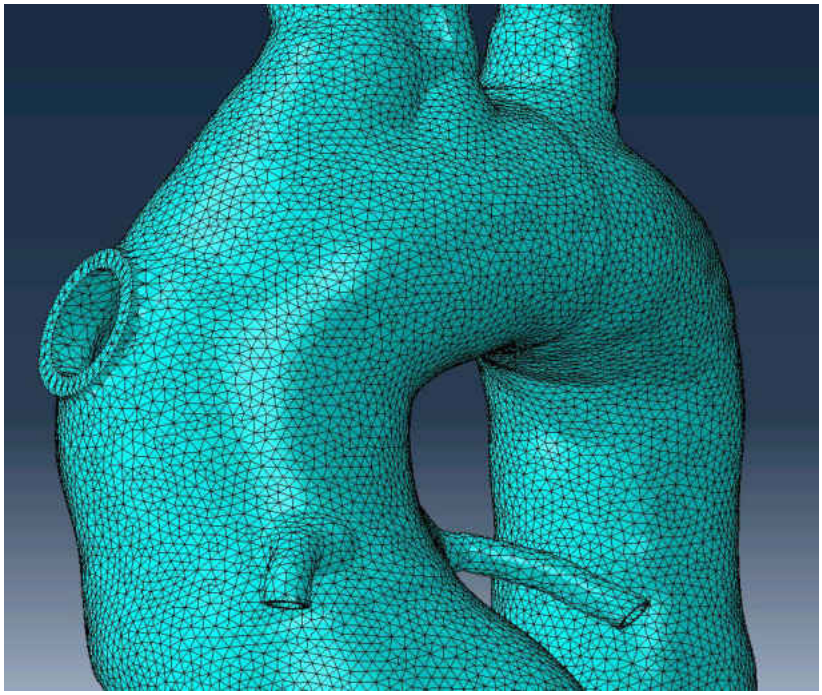

Figure 14 - Mesh close-up on cannula anastomosis post-surface treatment.

3.4. Lumped Parameter Model

The post-op circulation can be modeled using multi-degree of freedom (DOF) Windkessel models, where an electric circuit analogy based on the Greenfield and Fry approach is implemented. The LPM used derives from previous studies that our research group carried out at the University of Central Florida in order to impose pulsatile boundary conditions (BC) to the CFD simulations to determined embolization rates. This replica of the cardio vascular system is based on a so-called LRC compartment model that utilizes simple basic circuit elements of an inductor (L), a resistor (R), and a capacitor (C), to model the flow in a specific region of the vasculature as depicted in Figure 15.

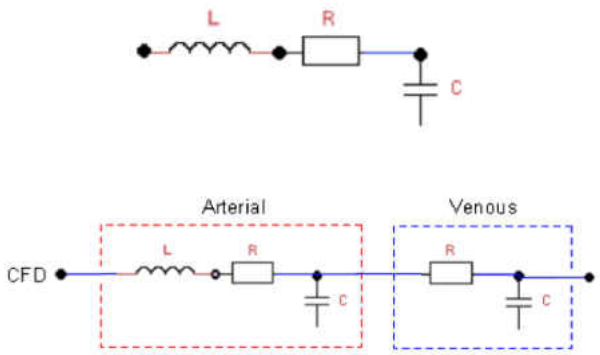

Figure 15 - Basic circulatory circuit element and arterial and venous basic circuit schemes.

This LRC compartment element is repeatedly used throughout the system for both arterial and venous beds peripheral to the region of interest in the CFD, namely the aortic arch and main branching vessels (Carotids, Vertebral, Subclavian, Coronaries and a portion of the descending aorta). The resistor accounts for the pressure drop due to viscous effects as a function of the geometrical features of the vessel (length, cross-sectional area), the capacitor implements vessel compliance (the ability of vessel to passively expand and contract), the inductor reproduces inertial effect of the flow. Additionally, diodes are utilized to simulate the presence of valves ensuring unidirectional flow through the heart. At the venous level, inertial effect can be neglected and the finalized model in depicted in Figure 15.

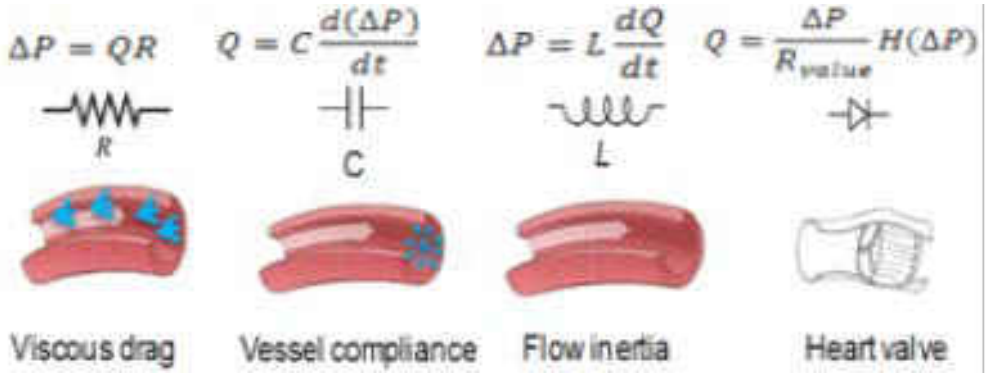

Figure 16 - Hydraulic analogy.

These elements are illustrated in Figure 16, where Q is the flow-rate mL/min, Δp is the pressure difference [mmHg]. A time dependent capacitance is utilized to model the heart pumping action driving the circulation. The elastance ($E_n(t_n)$) is the ratio of ventricular pressure to ventricular volume, which is the inverse of the capacitance and drives the pulsatile flow (Figure 17). This function was essentially obtained by curve fitting a partitioned function to physiological human data. Upon closer inspection, this function traces to separate regimes, systolic and diastolic. In the systolic phase, there is a power based growth controlled by the expression contained in the first set of brackets. The rate of growth may be controlled by changing the exponent. In diastole, the function is required to rapidly decrease, hence the large power function found in the denominator of the expression in the second set of brackets. The pulse wave is bound by an upper E_{max} and lower E_{min} limits determined in previous studies [13, 20, 21]. These values allow to simulate heart failure (HF), for example by sharply decreasing E_{max} therefore reducing the ejection fraction and modeling systolic failure.

$$E_n(t_n) = 1.55 \cdot \left[\frac{\left(\frac{t_n}{0.7}\right)^{1.9}}{1+\left(\frac{t_n}{0.7}\right)^{1.9}}\right] \cdot \left[\frac{1}{1+\left(\frac{t_n}{1.17}\right)^{21.9}}\right] \tag{4}$$

$$E(t) = (E_{max} - E_{min}) \cdot E_n(t_n) + E_{min} \tag{5}$$

Time appears in a non-dimensional manner, where $t_n = \frac{t}{t_c}$ and $t_c = \frac{60}{HR}$, with HR being the heart rate. The normalized time t_n allows the user to either increment or decrement the cycle's period based on the HR.

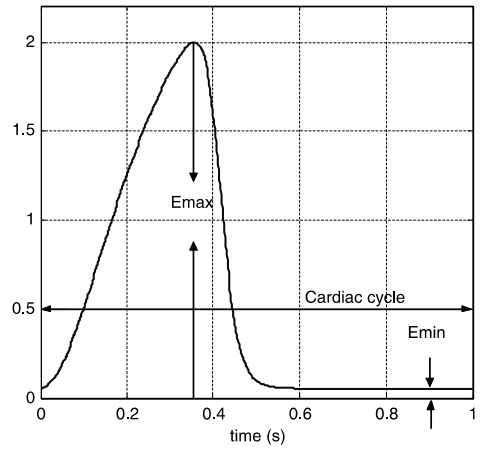

Figure 17 - Elastance function plot.

The basic relations utilized to determine flow rates and pressure across the basic LRC circuit element such that the pressure drop is given by $\Delta P = L\frac{dQ}{dt} + RQ$ and the flow rate across a compliance is $Q = C\frac{dP}{dt}$ (Figure 18). Using the Kirchhoff node and loop laws (Equations 6,7), the circuit is reduced to a closed-loop representation of the circulation modeled by a set of coupled linear ordinary differential equations that are solved by an in-house 4th order Runge-Kutta adaptive time stepping scheme. Appendix E contains all equations relative to the LPM circuit.

$$y_{i-1} = C\frac{dy_i}{dt} + y_{i+1} \rightarrow \frac{dy_i}{dt} = \frac{1}{C}[y_{i-1} - y_{i+1}] \tag{6}$$

$$y_i = y_{i+2} + Ry_{i+1} + L\frac{dy_{i+1}}{dt} \rightarrow \frac{dy_{i+1}}{dt} = \frac{1}{L}[y_i - Ry_{i+1} - y_{i+2}] \tag{7}$$

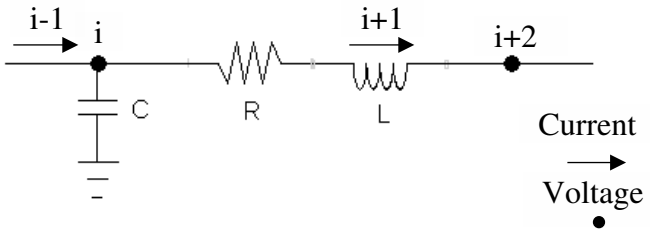

Figure 18 - Circuit schematic related to Equations 6 and 7 where y can either be current of voltage.

The circuit is tuned to output flows and pressure waveforms matching similar waveforms obtained from catheter studies and clinical criteria, inlet boundary conditions are then imposed on the CFD from the tuned circuit.

In the fluid domain, only resistances are accounted for and are iteratively computed during the coupling process until the flow field settles to a consistent sustained periodic solution. Once this occurs, the Lagrangian particle tracking scheme is activated and a successive phase of the study begins where several runs of 3-5 cardiac cycles are completed in order to collect data on thrombus transport. To determine fluid domain resistances flow rates and pressure are collected at specific location in the domain corresponding to the circuit's nodes (Figure 19). These CFD output are them time averaged and the segment resistance is computed using the following relation:

$$R = \frac{P_i - P_{i+1}}{\dot{m}_i} \tag{8}$$

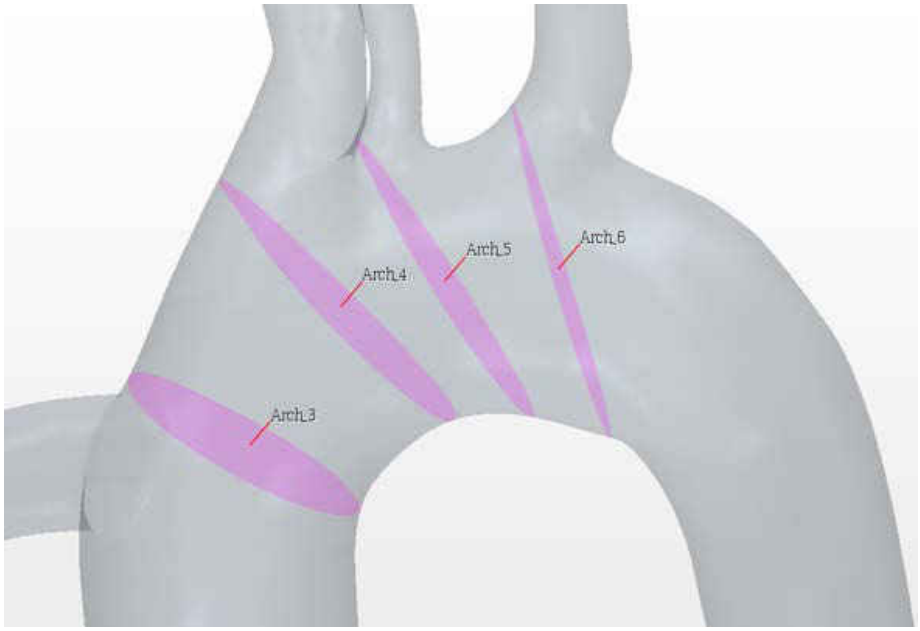

Figure 19 - Nodal representation of fluid domain.

The resultant 0D LPM representation of the LVAD peripheral circulation is a 50 degrees-of-freedom LPM model that is found in the following schematic display that illustrates how the basic circuit element has been iteratively used to form arterial and venous beds to form a closed loop approximating the vascular system.

It is important to note the LVAD itself is modeled in this this circuit. The relation for the pressure rise from the left ventricle to the aorta across the LVAD is taken as PLV(t)-PAo(t)=R*Q+L*(dQ/dt)-Ω*i*(t)/Q, where *i*(t) is the current supplied to the LVAD, and Ω, R* and L* are characteristic of the LVAD head (H), cannula resistances, and inductances [20, 21].

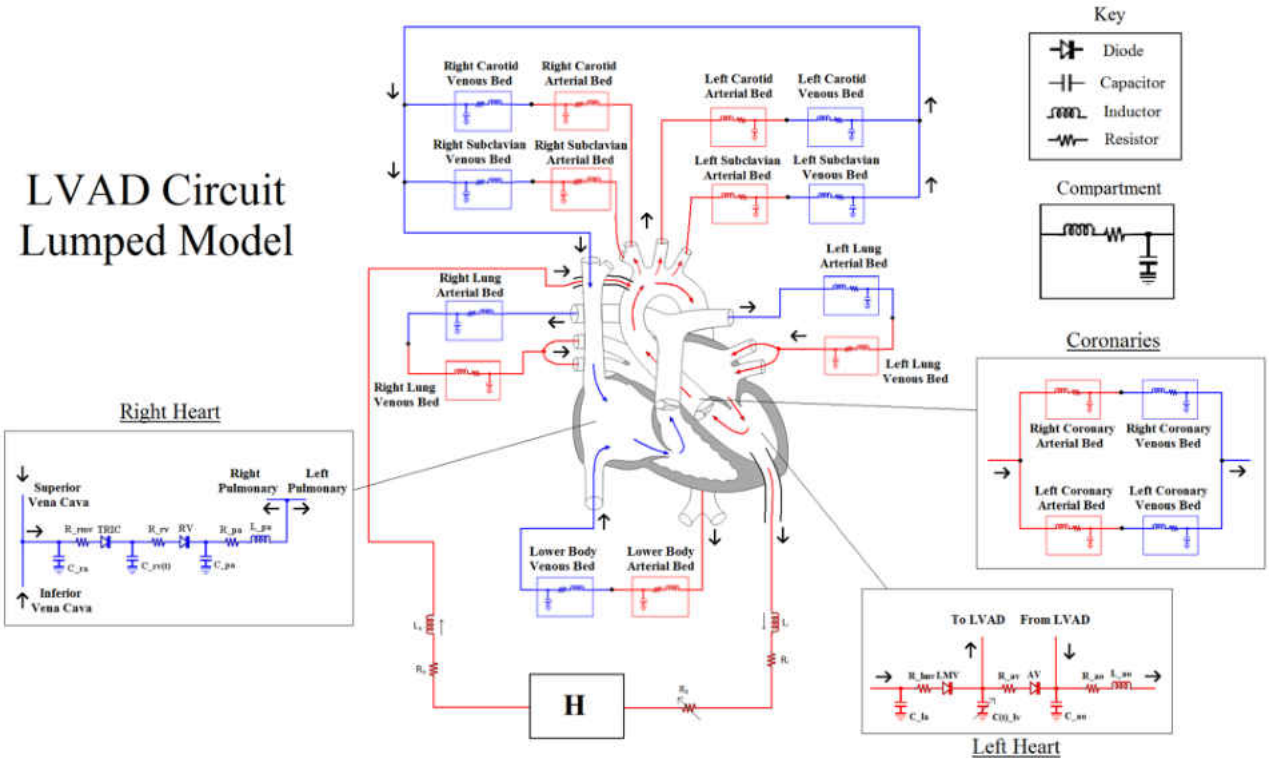

Figure 20 - LPM vascular circuit, including the LVAD pump model.

3.5. Computational Fluid Dynamics Model

In this multi-disciplinary research effort, the patient-specific geometries obtained from CT scan are implemented into the numerical domain in two modes. In the CFD portion of the problem, the geometry accounts solely for the flow volume where the fluid is modelled as having constant density of $1060\frac{Kg}{m^3}$ (incompressible) and non-Newtonian, using the modified (reduced 3 parameter) Carreau-Yasuda model based on hematocrit level for a healthy adult under laminar flow conditions (Equation 3 combined with Table 1). This model is a curve fit with values limited by μ_∞ being the centerline viscosity, μ_o the wall viscosity and λ the relaxation time. The blood-thrombus ensemble in treated as a two-phase flow, handled by a Eulerian-Lagrangian coupled scheme to solve the flow field and track particle transport using commercial computational fluid dynamics software StarCCM+© (2018 Siemens Product Lifecycle Management Software Inc., Munich, Germany). StarCCM+ is a finite volume multi-physics CFD software capable of modeling 2D and 3D flows, steady-state and transient simulations, viscous, laminar and turbulent flows, subsonic, transonic and supersonic flow, among other capabilities. Codes such as StarCCM+ use algorithms to solve the mass and momentum conservation equations governing fluid mechanics, namely the continuity and the Navier-Stokes equations:

$$\nabla \cdot \vec{V} = 0 \tag{9}$$

$$\rho \frac{\partial \vec{V}}{\partial t} + \rho\left(\vec{V} \cdot \nabla\right)\vec{V} = -\nabla p + \nabla \cdot \bar{\bar{\sigma}} + \overrightarrow{F_b} \tag{10}$$

For completeness, the forces considered in this model are body forces such as added mass, gravity (direction shown in Figure 21), buoyancy and surface forces, namely drag, Saffman lift and pressure gradients (Equation 12,13). The gravity vector may be

oriented in any desired direction based on the study to represent either a supine or stating patient position. In this study it is assumed that the patient is standing, hence the descending aorta may be thought as aligned with the z-axis.

$$m_p \frac{d\overrightarrow{V_p}}{dt} = \overrightarrow{F_{body}} + \overrightarrow{F_{surface}} \tag{11}$$

The right-hand side body force and surface force can be further subdivided in the following summation of loads:

$$\sum \vec{F}_{body} = \vec{F}_{gravity} \tag{12}$$

$$\sum \vec{F}_{surface} = \vec{F}_{drag} + \vec{F}_{added\,mass} + \vec{F}_{saffman} \tag{13}$$

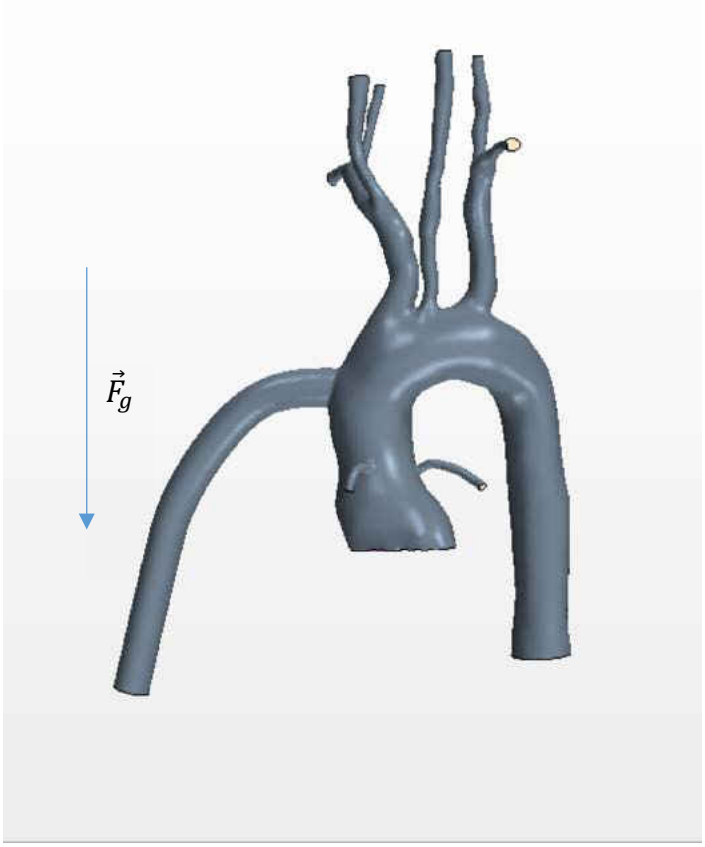

Figure 21 - Gravity direction applied to model for a standing patient.

Thrombi are modelled as non-interacting non-deforming solid spheres of set density ($1116.73\,\frac{Kg}{m^3}$) obtained from coagulating constituents of blood and of varying size tracked throughout the domain with a Lagrangian scheme. To conform to a previous study carried out by our group particle size is be set at, 2mm, 4mm and 5mm in diameter. Particle transport is regulated by gravity, aerodynamic forces (drag and lift) as well as 2 types of possible interactions: particle-to-wall regulated by normal restitution coefficients ranging from (0.5-1) for partially elastic collisions. In order to determine where these particles exit the fluid domain, at each outlet a particle counter is applied. This method allows to keep track of particles exiting and entering the domain in a time accurate manner.

The domain is discretized using an unstructured mesh with tetrahedral elements and near wall prism cell layers (Figure 22). The prism cell layer ensures high accuracy at the interface required for the FSI. In addition, to improve the near-wall flow solution accuracy for pressures in the fluid domain a prism layer has been included. This prism layer in the fluid domain is controlled by several parameters:

- Total layer thickness
- number of cell layers: number of substrates across total thickness
- layer thickness stretching factor: control over how much each subsequent layer stretches

The number of layer is user defined, in this study we retain 6 layers.

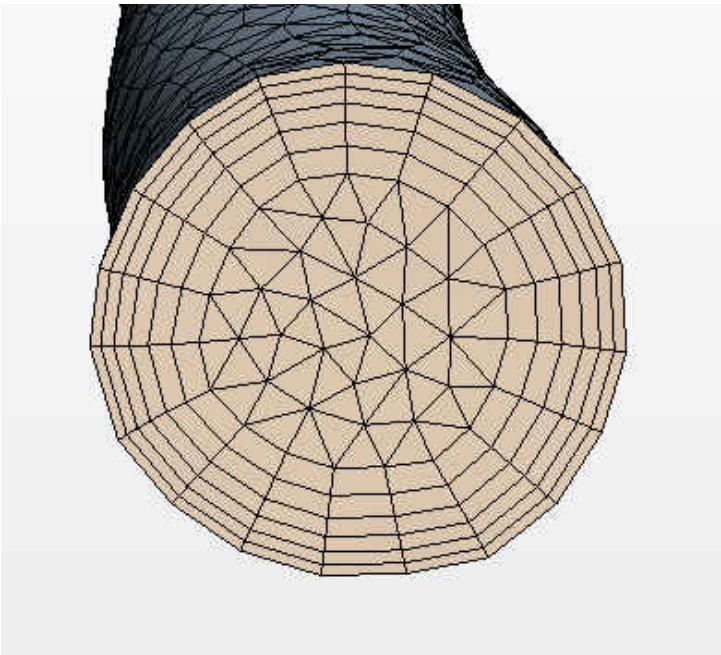

Figure 22 - Prism cell layer mesh at right coronary.

Given the vessel diameter range variability encountered in this study, from the aortic arch ~24mm down to the coronaries ~3mm a single mesh base size is not sufficient to ensure an overall proper mesh. Hence volumetric mesh refinement is applied in this case specifically at the coronaries with a 50% reduction in base size. A set of rectangles encasing the coronaries are used (Appendix C: Figure 81).

In this study, the segregated flow solver was chosen, based on the SIMPLE algorithm and combined with an implicit unsteady solver. The following equations represent the integral form StarCCM+ employs which retain transient and convective terms on the left-hand side, pressure gradient, viscous and load (body and surface forces) terms on the right-hand side.

$$\frac{\partial}{\partial t}\left(\iiint \rho dV\right) + \oiint \rho\left(\vec{v} - \vec{v}_g\right) \cdot dA = 0 \tag{14}$$

$$\frac{\partial}{\partial t}\left(\iiint \rho \vec{v} dV\right) + \oiint \rho \vec{v} \otimes \left(\vec{v} - \vec{v}_g\right) \cdot dA = -\oiint pI \cdot dA + \oiint T \cdot dA + \iiint \sum F dV \tag{15}$$

Since this study is study considers only laminar flow conditions, the stress tensor T is taken as

$$T = \mu\left[\nabla\vec{v} + (\nabla\vec{v})^T - \frac{2}{3}(\nabla\cdot\vec{v})I\right] \tag{17}$$

where the viscosity $\mu(\dot{\gamma})$ is given by Equation (3). These equations are then put in a discrete form. To retain great accuracy second order temporal discretization is employed for the transient term. Convective terms are resolved with to a second order upwind scheme.

The discrete conservation of mass equation requires closer inspection. In the absence of any mass sources within the domain the continuity equation is expressed in the following equations along with the pressure and velocity correction equations, core of the SIMPLE algorithm.

$$\sum_f \dot{m}_f = \sum_f\left(\dot{m}_f^* + \dot{m}_f'\right) = 0 \tag{18}$$

$$p = p^* + \omega_p p' \tag{19}$$

$$v = v^* + \omega_v v' \tag{20}$$

where the uncorrected face mass flow rate $\dot{m}_f^*$ is computed after solving the velocity and pressure flow fields from the momentum equation and $\dot{m}_f'$ is the correction required to satisfy continuity. Likewise, the $'$ and the $*$ indicate the corrected and uncorrected terms in the pressure and velocity equations. While inner-iterating within a time-step, to retain stability, an under-relaxation factor ω is introduced. The uncorrected mass flow rate at a cell face is written as

$$\dot{m}_f^* = \rho_f\left[\vec{A}\cdot\left(\frac{\vec{v}_0^* + \vec{v}_1^*}{2}\right) - G_f\right] - \Upsilon_f \tag{21}$$

where $\vec{v}_0^*$ and $\vec{v}_1^*$ are the uncorrected cells velocities, $G_f = \left(A \cdot \vec{v}_g\right)_f$ is the grid flux ($\vec{v}_g$ the grid velocity), $\vec{A}$ the directional area and Υ_f the Rhie-and-Chow dissipation at the face. This study implements a moving grid due to the fluid-structure interaction that is the centerpiece of the flow simulation so that additional consideration over the grid flux term must be clarified.

In this study, the solution domain changes with time as the fluid-solid interface moves, hence the grid moves (especially near the interface). Since the mesh moves mass conservation is not ensured due to an artificial "added-mass" effect. For uneven mesh motion at the cell level a mass source is observed [22, 23, 24]. In the following example for a single 2D cell using a first order Euler scheme, it is shown how this added mass appears and how it can be manipulated to obtain a correct solution (Figure 23).

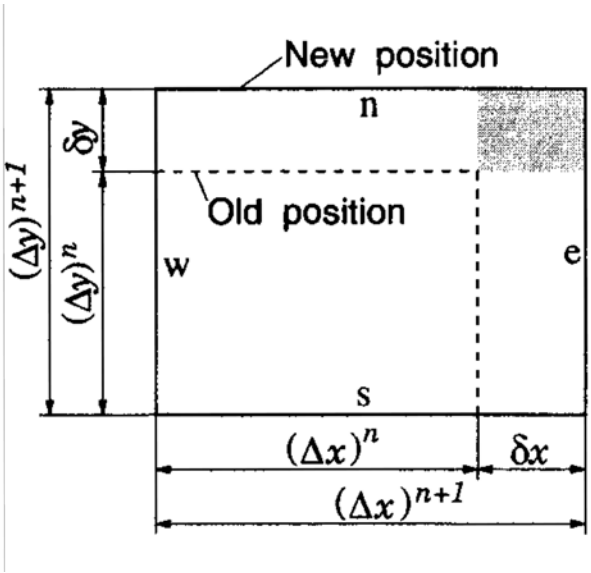

Figure 23 - Control Volume for moving cell boundaries [22].

$$\rho\frac{[\Delta V^{n+1}-\Delta V^n]}{\Delta t}+\rho[(u-u_b)_e-(u-u_b)_w]^{n+1}\Delta y^{n+1}+\rho[(v-v_b)_n-(v-v_b)_s]^{n+1}\Delta x^{n+1}=0 \quad (22)$$

where u and v are the cell velocities and u_b and v_b are the boundary velocities. Upon simplification, the mass conservation is indeed not respected and a source term appears.

$$\delta\dot{m} = \rho\big(u_{b,e} - u_{b,w}\big)\big(v_{b,n} - v_{b,s}\big)\Delta t \tag{23}$$

For constant grid velocity, this term disappears. However, in complex 3D geometries with an unstructured mesh this term cannot be ignored even for very small time-steps, as the added mass simply adds up for a large cell count. Mass conservation can be enforced by implementing the Space Conservation Law (SPL) similar to cell volume continuity equation of the following form

$$\frac{\partial}{\partial t}\oiiint dV - \oiint \vec{v}_b \cdot d\vec{A} = 0 \tag{24}$$

or in the discrete form

$$\frac{[\Delta V^{n+1} - \Delta V^n]}{\Delta t} = \sum_f\big(\vec{v}_b \cdot \vec{A}\big) = \frac{\sum_f \delta V_f}{\Delta t} \tag{25}$$

where δV_f represents the volume swept by the boundary motion in one direction which gives origin to a "sweep rate" $\frac{\delta V_f}{\delta t} = \vec{v}_b \cdot d\vec{A}$. Moving back to the continuity equation this term appears in the discrete form when computing the mass fluxes at the cell face as

$$\dot{m}_f = \oiint \rho(\vec{v} - \vec{v}_b) \cdot d\vec{A} \cong \rho\vec{v} \cdot d\vec{A} - \rho\dot{V}_f \tag{26}$$

For an incompressible flow that last term (volume sweep rate) in Equation (26) cancels the transient term in Equation (14) effectively deleting any grid flux terms from our computations. Failure to omit these grid movement terms from the flow solver would cause the uncorrected mass flow computation (Equation (21)) to make an undesired adjustment which in turn would cause the pressure correction to be largely over-estimated inducing pressure spikes. Strong under-relaxation or time-step manipulation will not help the solution recover. Hence the user must take care in omitting the grid flux terms.

To quantify particle behavior in relation to the local flow field the Stokes number (STK) is typically used. It represents the ratio of the particle relaxation time to the local fluid relaxation time (Equation 27).

$$STK = \frac{\tau_p U_f}{d_h} \tag{27}$$

Where $U_f = \left|\vec{U}\right|$ is the local fluid velocity and d_h the hydraulic diameter. The p-subscripts refers to particle quantities whereas the f-subscript refers to the fluid. The particle relaxation time τ_p can be expressed as follows:

$$\tau_p = \frac{\rho_p d_p^2}{18\mu} \tag{28}$$

To obtain localized STK values the hydraulic diameter d_h must be computed locally when sampling each particle STK. It can be defined as the ration of the local cross-sectional area to the local perimeter (Equation 29).

$$h_d = 4 \cdot \frac{A_{lumen}}{P_{lumen}} \tag{29}$$

Given the complex topology and in order to sample the correct lumen area and perimeter in StarCCM+ section planes and perimeters where generated at various location in the domain (Figure 24).

Figure 24 - Sample cross-section plane (top) and perimeter (bottom) at the DA.

Contour and surface integrals were then computed given the local perimeter and cross-section as follows:

$$A_{lumen} = \oiint dA \tag{30}$$

$$P_{lumen} = \oint dL \tag{31}$$

Figure 25 - Sample of patient specific geometry obtained from CT scans with LVAD cannula anastomosed to the ascending aorta.

Boundary conditions derived from the LPM model for all outlets include the total pressure at the aortic root, and mass flow rates at all other boundaries (inlet and outlet alike). The LPM model imposes a 4-1 L/min flow ratio on the system, 4 L/min provided by the LVAD and 1 L/min ejected by the left ventricle, this scenario represents an acute heart failure.

3.6. Solid domain material model

With the help of Computer Aided Design (CAD) software (3-Matic© and Mimics©) a patient-specific aortic wall geometry with variable thickness is brought into the numerical domain. This was achieved by first determining the hydraulic diameter thought the fluid

domain model at small interval along the vessels' centerline, then applying a 10% offset (based on the hydraulic diameter) and finally wrapping the geometry to smooth out the surfaces.

This study is an example of nonlinear mechanics analysis. Nonlinearity in this case generates from the material properties of the aortic wall (hyperelastic) and the geometry (non-uniform deformation).

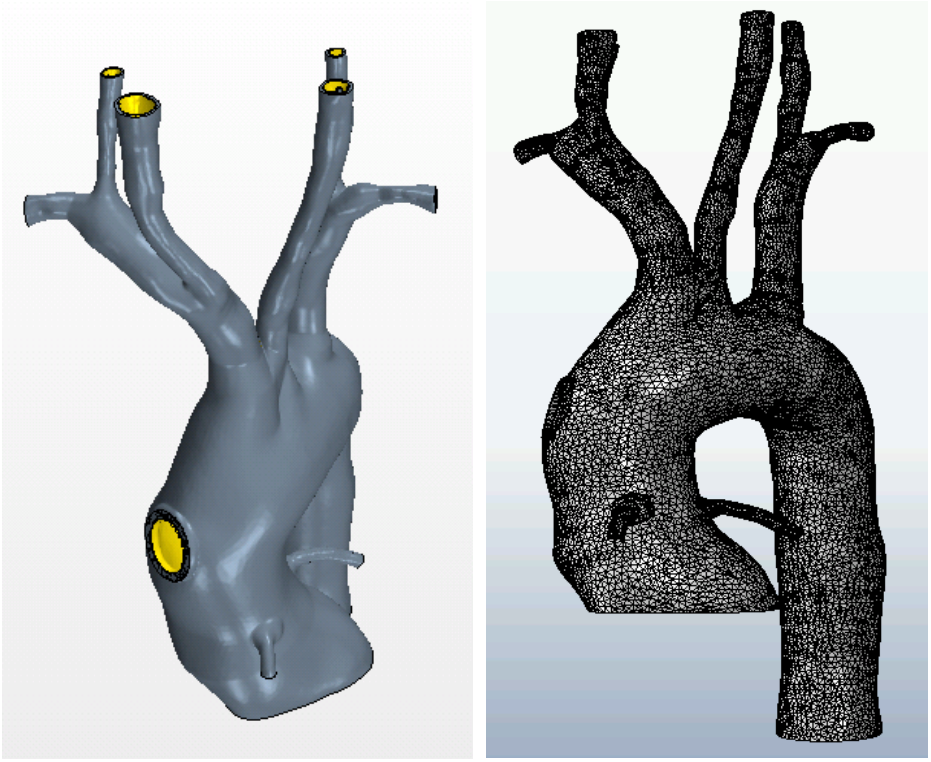

Figure 26 - Aortic wall model (left) and aortic wall mesh (right).

Given a solid geometry the material behavior must be modelled (Figure 26). In principle, this study aims at understating what kind of assumptions can be made when molding this type of FSI problem. From a material modelling standpoint, we will compare a linear elastic model to a hyperelastic model which is typically preferred.

For a linear elastic model, the traditional formulation is used where one specifies the Youngs's modulus, *E*, and the Poisson ratio, ν, to determine the stress field and resulting strains. The stress σ is then linearly related to the strain ϵ as

$$\sigma = E\varepsilon \tag{32}$$

In this case a linear elastic model will be applied to regions where the hyperelastic model can hardly be implemented due to failure to establish a clear fiber orientation. Physiological values for Young's modulus and Poisson's ratio are found to greatly vary in range between $E = 0.1 - 0.9\ MPa$ and $\nu = 0.48$ depending on fiber activation [25, 26]. A value of $0.4\ MPa$ would be both conservative and within the physiological loading range described in literature [19]. It must be kept in mind that the arterial wall presents an anisotropic material which deforms in response to internal vessel pressure loads hence a multi-layer constitutive model centered on the mechanics of fiber-reinforced composites is required. In addition, in absence of loads the arterial walls retain residual stresses. This can be noted as one would cut open an artery along its longitudinal axis, the vessel would spring open.

The typical geometry presents the symmetries of a cylindrical orthotropic material. From a physiological point of view, the arterial wall is made of three major thick-walled layers (Intima (I), media (M), and adventitia (A)).

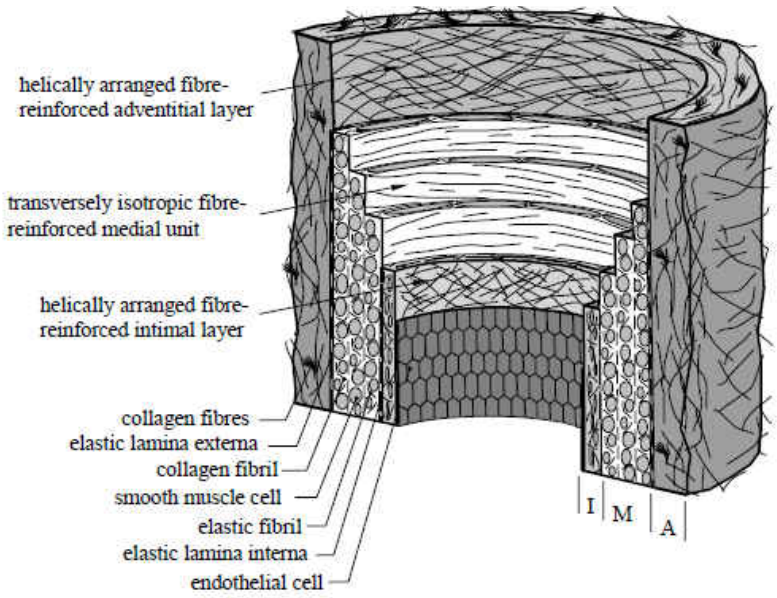

Figure 27 - Histo-mechanical idealization of a healthy elastic artery [19].

Due to the layered structure the stress-strain curve will be inevitably dictated by the combined response of all layers. Extensive material testing conducted in literature identifies arterial wall behavior has hyperelastic. Such a material exhibits a reversible but non-linear stress-strain relation that is inherently described by an underlying potential, the so-called strain-energy function, whose derivatives with respect to the Lagrangian-Green or Cauchy-Green strain provide the components of the respective stress tensor. Figure 28 displays the typical behaviors observed, distinguishing an elastic or visco-elastic regime and an inelastic interval which may lead to stress-softening followed again by an elastic or visco-elastic regime.

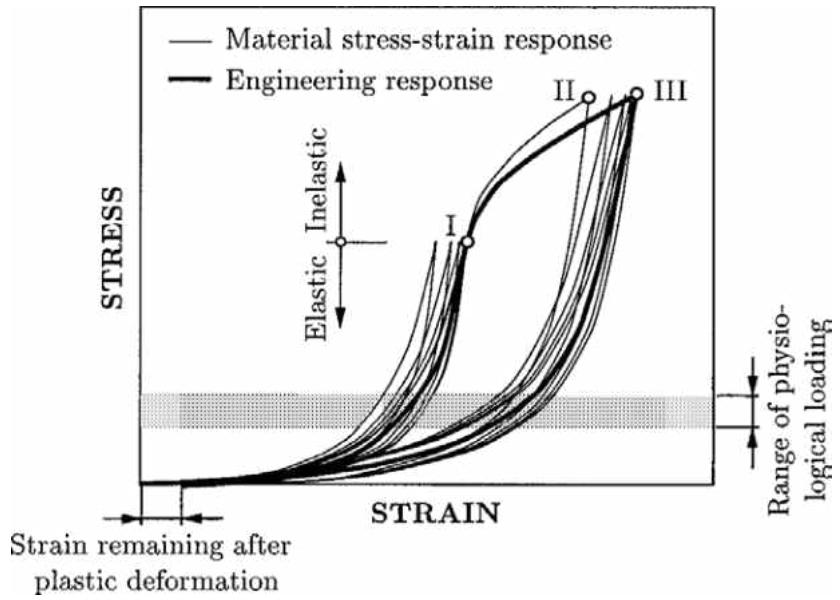

Figure 28 - Uniaxial stress-strain curve for circumferential arterial sample from [19].

In order to accurately display the hyperelastic behavior of the arterial wall in the solid domain the Holzapfel built-in model in ABAQUS will be used. Each layer can be treated as a composite reinforced by two types of collagen fibers arranged in symmetrical spirals. Given similar mechanical behaviors each layer can be modelled using the same strain-energy function with different material parameters for each separate layer [19].

The Holzapfel model separates the isochoric strain-energy function ψ into Ψ_{iso} which associates the isotropic non-collagenous material matrix mechanical response and Ψ_{aniso} due to anisotropic resistance to stretch at high pressures associated with collagenous fibers [19]. Hence the potential strain-energy function is written as follows:

$$\overline{\Psi}(\bar{C}, \mathrm{a}_{01}, a_{02}) = \overline{\Psi}_{iso}(\bar{C}) + \overline{\Psi}_{aniso}(\bar{C}, \mathrm{a}_{01}, a_{02}) \tag{33}$$

Where $\bar{C}$ represents the distortional part of the right Cauchy-Green strain tensor and the directional vector $a_{0\mathrm{i}}\ \mathrm{for\ i} = 1{,}2$ characterize the family of oriented fibers with $|a_{01}| = |a_{02}| = 1$. Given these directional vectors structure tensors can be generated,

A_{i} for $\mathrm{i} = 1{,}2$ from the tensor product of $a_{01} \otimes a_{02}$ which characterize the wall structure [19]. In order to represent the response of the fibers the parameters $\bar{C}, \mathrm{A}_1 \text{and } A_2$ are described in the following invariant-based formulation:

$$\bar{\mathrm{I}}_1(\bar{C}) = \mathrm{tr}\,\bar{C} \qquad \bar{\mathrm{I}}_2(\bar{C}) = \frac{1}{2}[(\mathrm{tr}\,\bar{C})^2 - \mathrm{tr}\,\bar{C}^2] \qquad \bar{\mathrm{I}}_3(\bar{C}) = \det \bar{C} = 1 \qquad (34)\ (35)\ (36)$$

$$\bar{\mathrm{I}}_4(\bar{C}, \mathrm{a}_{01}) = \bar{C} : \mathrm{A}_1 \qquad \bar{\mathrm{I}}_5(\bar{C}, \mathrm{a}_{01}) = \bar{C}^2 : \mathrm{A}_1 \qquad (37)\ (38)$$

$$\bar{\mathrm{I}}_6(\bar{C}, \mathrm{a}_{02}) = \bar{C} : \mathrm{A}_2 \qquad \bar{\mathrm{I}}_7(\bar{C}, \mathrm{a}_{02}) = \bar{C}^2 : \mathrm{A}_2 \qquad (39)\ (40)$$

$$\bar{\mathrm{I}}_8(\bar{C}, \mathrm{a}_{01}, \mathrm{a}_{02}) = (\mathrm{a}_{01} \cdot \mathrm{a}_{02})\mathrm{a}_{01} \cdot \bar{C}\mathrm{a}_{02} \qquad \bar{\mathrm{I}}_9(\mathrm{a}_{01}, \mathrm{a}_{02}) = (\mathrm{a}_{01} \cdot \mathrm{a}_{02})^2 \qquad (41)\ (42)$$

Hence the generic strain-energy function becomes

$$\bar{\Psi}(\bar{C}, \mathrm{A}_1, A_2) = \bar{\Psi}_{iso}(\bar{C}) + \bar{\Psi}_{aniso}(\bar{C}, \mathrm{A}_1, A_2) \qquad (43)$$

and given the invariant formulation

$$\bar{\Psi}(\bar{C}, \mathrm{A}_1, A_2) = \bar{\Psi}_{iso}(\bar{\mathrm{I}}_1, \bar{\mathrm{I}}_2, \bar{\mathrm{I}}_3) + \bar{\Psi}_{aniso}(\bar{\mathrm{I}}_1, \bar{\mathrm{I}}_2, \dots, \bar{\mathrm{I}}_8) \qquad (44)$$

Since the $\bar{\mathrm{I}}_3 \text{ and } \bar{\mathrm{I}}_9$ are constants, and $\bar{\mathrm{I}}_4 \text{and } \bar{\mathrm{I}}_6$ are the squares of the stretches in the direction of $\mathrm{a}_{01} \text{and } \mathrm{a}_{02}$ which are sufficient to capture the general anisotropic behavior of the arterial wall the strain-energy (44) can be simplified to

$$\bar{\Psi}(\bar{C}, \mathrm{A}_1, A_2) = \bar{\Psi}_{iso}(\bar{\mathrm{I}}_1) + \bar{\Psi}_{aniso}(\bar{\mathrm{I}}_4, \bar{\mathrm{I}}_6) \qquad (45)$$

$\Psi_{iso}(\bar{\mathrm{I}}_1)$ is defined by using the classical neo-Hookean model for the isotropic response in each layer as follows

$$\bar{\Psi}_{iso}(\bar{\mathrm{I}}_1) = \frac{\mu}{2}(\bar{\mathrm{I}}_1 - 3) \qquad (46)$$

Where $\mu > 0$ represents stress-like parameter of the material and $\bar{I}_1$ is the first deviatoric strain invariant of the distortional part of the right Cauchy–Green tensor $\bar{C}$ [19].

In order to capture the strong stiffening at high pressures $\bar{\Psi}_{aniso}(\bar{I}_4, \bar{I}_6)$ is represented by an exponential function to describe the strain energy stored in the collagen fibers

$$\bar{\Psi}_{aniso}(\bar{I}_4, \bar{I}_6) = \frac{k_1}{2k_2} \sum_{i=4,6} \{\exp[k_2(\bar{I}_i - 1)^2] - 1\} \quad (47)$$

Where $k_1 > 0$ is a stress-like material parameter and $k_2 > 0$ is a dimensionless parameter. When correctly chosen, these parameters show absence of fiber response in the low-pressure domain [19].

The solid models were created using the commercial code Abaqus v6.16. This FEM code offers the user several models to represent the behavior of an anisotropic hyperelastic material. In this particular case, the Holzapfel built-in model was chosen, which uses the strain energy potential function proposed by Holzapfel, Gasser and Ogden (as defined in the software) [18, 19]:

$$U = C_{10}(\bar{I}_1 - 3) + \frac{1}{D}\left(\frac{(J^{el})^2 - 1}{2} - \ln(J^{el})\right) + \frac{k_1}{2k_2} \sum_{\alpha=1}^{N} \{\exp[k_2 \langle \bar{E}_\alpha \rangle^2] - 1\} \quad (48)$$

$$\bar{E}_\alpha \stackrel{def}{=} k(\bar{I}_1 - 3) + (1 - 3k)(\bar{I}_{4(\alpha\alpha)} - 1) \quad (49)$$

$$\bar{I}_{4(\alpha\alpha)} = A_\alpha \cdot \bar{C} \cdot A_\alpha \quad (50)$$

$$k = \frac{1}{4} \int_0^\pi \rho(\Theta) \cdot sin^3\Theta \, d\Theta \quad (51)$$

$$\rho(\Theta) = 4\sqrt{\frac{b}{2\pi}} \frac{\exp[b(\cos(2\Theta)+1)]}{-i \, \mathrm{erf}(\sqrt{2b})} \quad (52)$$

$$J^{el} = \frac{J}{J^{th}} \quad (53)$$

$$J^{th} = (1 + \epsilon_1^{th})(1 + \epsilon_2^{th})(1 + \epsilon_3^{th}) \quad (54)$$

Where U is the strain-energy function (potential) per unit of reference volume, k defines the degree of fiber orientation distribution and $\rho(\Theta)$ is the fiber orientation density function in the range of $[\Theta, \Theta + d\Theta]$; $C_{10} = \frac{\mu}{2}$, $\mathrm{D} = \frac{2}{\mathrm{K_0}}$ with $\mathrm{K_0}$ initial bulk modulus, $\mathrm{k_1}$ and $\mathrm{k_2}$ are temperature-dependent material parameters ; $\mathrm{J^{el}}$ is the elastic volume ratio defined by the ratio of the total volume ratio J and the thermal volume ratio $\mathrm{J^{th}}$ based on the thermal expansion strains; N refers to the number of families of fibers $(N \leq 3)$. $\bar{\mathrm{I}}_1$represents the first deviatoric strain invariant as in Equation (34-42). $\bar{\mathrm{I}}_{4(\alpha\alpha)}$ in (50) are the pseudo-invariants of $\bar{C}$ and A_α. When $k = 0$ fibers are perfectly aligned characterizing the material as isotropic and for $k = 1/3$ fibers are randomly distributed making the material isotropic [27].

Collagen fibers are only activated when undergoing tension loads, buckling would occur under compressive loads. In order to prevent buckling anisotropic contribution occurs when fiber strain in equation (48) is positive, where $\overline{\mathrm{E}}_\alpha > 0$ and $< \overline{\mathrm{E}}_\alpha > = \frac{1}{2}(|\overline{\mathrm{E}}_\alpha| + \overline{\mathrm{E}}_\alpha)$. The D parameter in (48) is thus taken to be approximately zero (set to a value of D=1E-6) to treat this model as an incompressible solid as arteries can be treated as such under physiological loads.

Table 2 - Parameters for the Holzapfel model in Abaqus [28, 29].

Material	μ [MPa]	k_1 [MPa]	k_2	κ	θ [°]	ρ [kg/m^3]
Human Thoracic Artery	0.017	0.56	16.21	0.18	51.0	1080

Given the anisotropic portion of the strain energy function the fiber orientation of the material must be imposed. The fiber stiffening behavior is expressed in the anisotropic

stain energy equation through the deviatoric invariants $\bar{I}_4$ and $\bar{I}_6$ for each family of fibers, calculated from the direction tensors A_1 and A_2. To prescribe fiber orientation, first a material orientation is specified using a cylindrical coordinate system placed on the vessels centerline and applied to the nearby continuum elements (Figure 29).

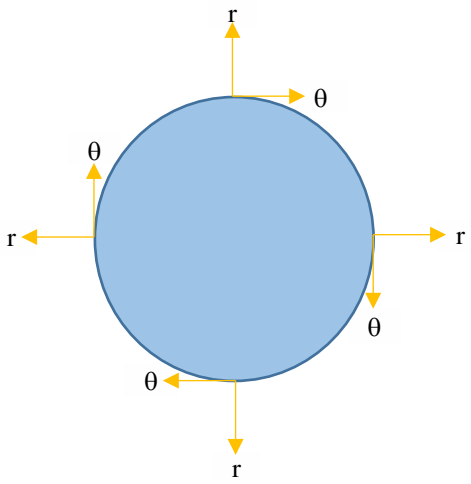

Figure 29 - Material orientation in a conduit cross-section.

Once each element has a local direction, the fiber orientation can be applied by imposing the fiber vector directions in the form of coordinates based on fiber alignment angle. The fiber orientation is assumed constant across the thickness hence the radial direction is omitted, fibers lay in the θ-z plane. Fiber direction dispersion across the arterial wall is accounted by k. Figure 30 offers insight on the fiber (in red) orientation definition expressed as vector quantities evaluated from γ as:

$$a_{0i} = \begin{cases} \begin{pmatrix} 0 \\ \cos(\gamma) \\ \sin(\gamma) \end{pmatrix} if\ i = 1 \\ \begin{pmatrix} 0 \\ \cos(\gamma - 2\gamma) \\ \sin(\gamma - 2\gamma) \end{pmatrix} if\ i = 2 \end{cases} \tag{55}$$

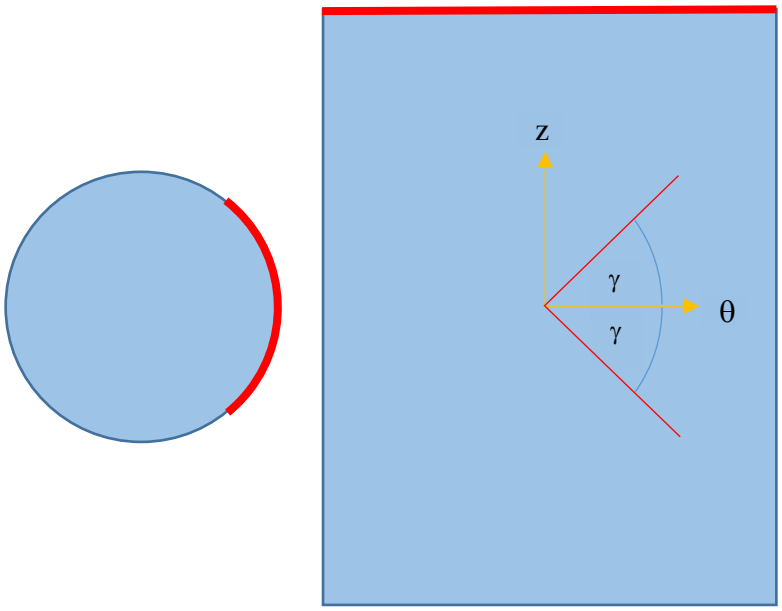

Figure 30 - Fiber orientation in θ-z plane based on inclination angle γ.

This concept is simple to apply to a straight tube. However, for a more complex geometry the model must be partitioned and the abovementioned procedure has to be repeatedly applied for each subdomain. In this case, each distinct vessel has a separate cylindrical coordinate system applied with the same material properties prescribed. Since each separate CS system is defined based on solid geometry nodes, as the model displaces the CS move along with it. This aspect can be of particular use in case bulk motion cannot be neglected. Figure 31 displays the portioned arterial wall geometry.

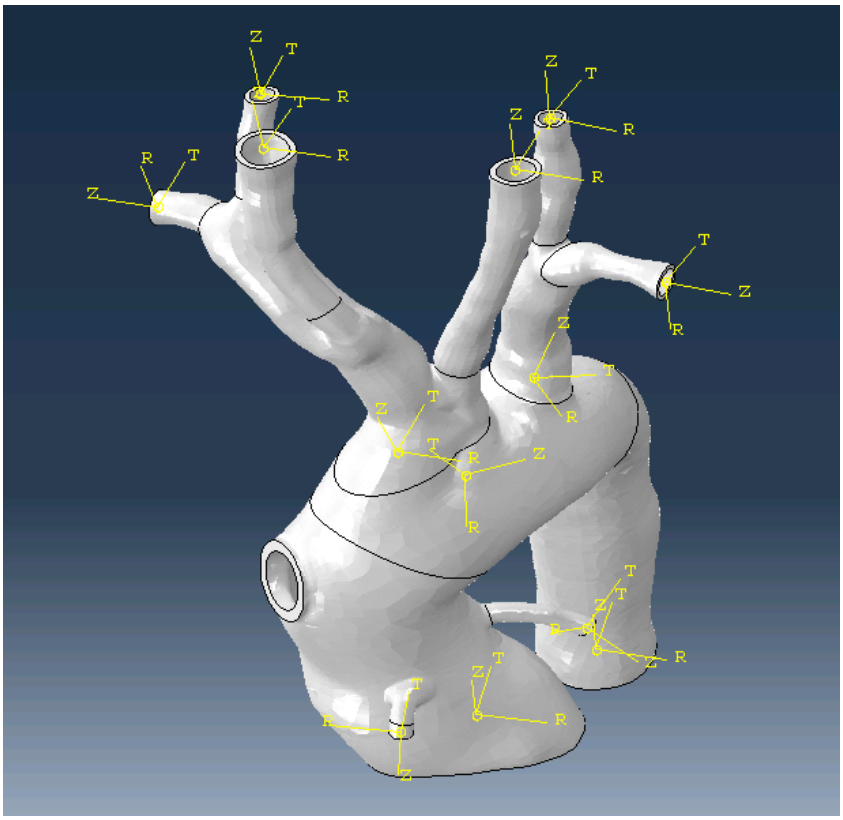

Figure 31 - Partitioned arterial wall geometry.

3.7. Solid domain mesh and solver

The mesh is directly generated in the destination software for FEA. Two types of continuum elements were available to discretize the solid domain: a 20-node quadratic brick which offers more accurate solution (C3D20, traditionally preferred) and a 10-node quadratic tetrahedron (C3D10) mesh that lessens computational expenses which was chose for this study due to the highly irregular topology. Notably all node in a continuum element have 3 translational DOF (Figure 32).

Figure 32 - 20-node brick (left) and 10-node tetrahedron (quadratic elements) [30].

This time accurate Finite Element Method (FEM) code discretizes and solves the governing equations of solid mechanics (56). These equations are discretized and solved subject to boundary conditions including external loads and constraints.

$$\nabla \cdot \sigma + \overrightarrow{F_b} = \rho \vec{a} \tag{56}$$

Inertial effects due to the acceleration of the wall may be neglected compared to that of the fluid despite undergoing cyclical loads. Wall displacement is caused by axial pressure gradients driving the flow with the condition of no slip at the fluid-solid interface. The FSI coupling ensures that the kinematic and dynamic continuity are satisfied at all time. In order to solve the equations of solid mechanics, a constitutive relation must be provided to relate the stress tensor to the deformation, the current model implements an Holzapfel hyperelastic formulation accounting for 2 fiber orientation (combined 3-layer model of the intima, media, and adventitia tunica). In summary, based on pressure measurements deriving from the CFD at the wall boundaries, the FEA software Abaqus© computes nodal displacements and refers them back to the CFD in order to enable mesh morphing schemes. A sample of the geometry obtained is found in Figure 26.

Abaqus, as most FEM solvers, offers two approaches to solving any FE problem, implicit or explicit methods. Implicit methods are unconditionally stable due to stiffness-based solution, computational expenses are typically due to a large number of iterations required for set-convergence. Explicit methods on the other hand use explicit integration,

are conditionally stable and require much less computing power, however, the explicit method is conditionally stable and thus strongly dependent on the integrating time-step for stability. Both methods strongly depend on the mesh size.

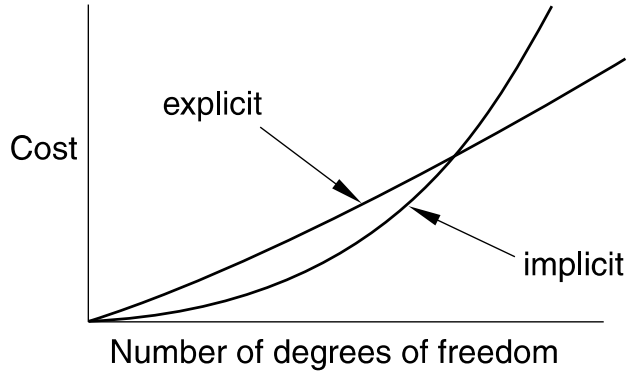

Figure 33 - Cost vs. model DOF for explicit and implicit methods [30].

Figure 33 shows the relation of computational cost to mesh refinement and for a growing DOF count the explicit methods would appear to be more cost effective. However, in this study due to the strong fluid-solid coupling time-step adjustments to maintain explicit stability would ultimately become inconvenient as time-step would become very small due the dominant nonlinearities. Hence the implicit method is used.

The implicit method invokes the use of Hilber-Hughes-Taylor (HHT) method to solve for position, velocity and acceleration at each time-step. The following equations outline the method.

$$Ma^{n+1} = (1+\alpha)F^{n+1} - \alpha F^{n} \tag{57}$$

$$v^{n+1} = v^{n} + \Delta t\big((1-\gamma)a^{n} + \gamma a^{n+1}\big) \tag{58}$$

$$u^{n+1} = u^{n} + v^{n}\Delta t + \frac{\Delta t^{2}}{2}\big((1-2\beta)a^{n} + 2\beta a^{n+1}\big) \tag{59}$$

where $a, v\ and\ u$ are the acceleration, velocity and displacement. The constant α with $\beta = \left(\frac{1-\alpha}{2}\right)^2$ and $\gamma = \frac{1-2\alpha}{2}$ regulates the degree of dissipation, and it is bounded as $-\frac{1}{3} < \alpha < 0$. For $\alpha = 0$ no dissipation occurs. Tabulated values for these constants as used in this study are found in table 3.

Table 3 - HHT dissipation constants.

HHT Dissipation constants	
α	-0.300
β	0.500
γ	0.914

Given a co-simulation time-step Abaqus advances the solution within the time-step with an auto-increment scheme to retain stability. Depending on the deformation Abaqus may increase or decrease the subsequent time step. The user may prescribe an initial time-step, minimum time-step and a maximum time-step (namely the co-simulation time-step).

Given that StarCCM+ applies time-dependent load onto the fluid-solid interface, the equation of motion expressed in Equation 56, can be represented in its most general from for a transient dynamic analysis as

$$[M]\{\ddot{u}\} + [C]\{\dot{u}\} + [K]\{u\} = \{F(t)\} \tag{60}$$

where $[M]$ is the mass matrix, $[C]$ is the damping matrix, $[K]$ the stiffness matrix, $\{\ddot{u}\}$, $\{\dot{u}\}$ and $\{u\}$ the acceleration, velocity and displacement vectors and $\{F(t)\}$ the time-varying load vector. When inertial effect can be neglected, this equation can be used for static

analysis instead where the mass matrix term is omitted. Similar considerations an be made on the damping term.

When invoking a static analysis Abaqus Equation 60 omits inertial effect and can be reduced to

$$[K(u)]\{u\} = \{F\} \tag{61}$$

in which case, due to strong nonlinearities a direct sparse solver is used to solve for the system of equations. The direct solver employs Gauss elimination to solve for displacements.

When inertial effects are considered the nonlinear problem is solved using the Newton-Raphson method at the time-step level (Equation 62 applied in Figure 34).

$$\vec{x}^{n+1} = \vec{x}^{n} - \frac{f(\vec{x}^{n})}{f'(\vec{x}^{n})} \tag{62}$$

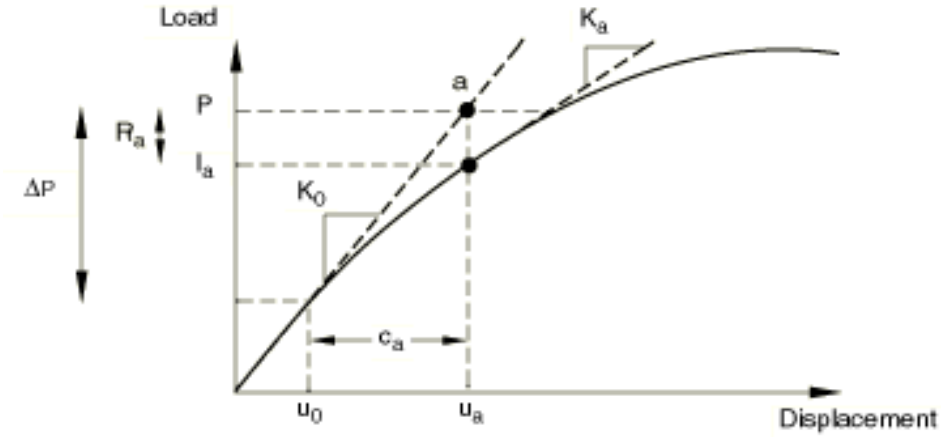

Figure 34 - Sample iterative step employing the Newton method [30].

Once displacements are obtained the configuration is deformed and inertial response is computed. To determine convergence, residual forces are computed as the difference of applied loads to inertial forces. Total increment is also computed for the computed displacements. Residual forces are then compared to tolerance values to

ensure convergence. Abaqus performs an additional check to prevent excessive deformation even for equilibrium condition by checking that the total displacement increment is not exceeded by a local displacement correction. In this study static and dynamic responses are used and compared to estimate the acceptable degree of approximation applicable to the model.

3.8. Boundary Conditions

This paradigm requires 2 separate sets of Boundary Conditions (BCs), BCs applied on the fluid domain and BCs applied on the solid domain. In the fluid domain, BCs are of 2 types: the traditional set which imposes the flow field and another related to the structural coupling constricting the morphing of the mesh. In the solid domain, BCs are uniquely defined to restrict the model's movements in the 3-D space.

3.8.1. Fluid domain BCs

As aforementioned the LPM models the cardiovascular system and provides BC the CFD code requires initiating the flow computations. A total of 11 BCs are needed to fully define the fluid domain as displayed in the following table. In this study only 2 types of BC have been used, namely mass flow inlet/outlet and pressure inlet.

Table 4 - Definition of CFD BC at each boundary.

Boundary	Definition	Quantity
Ascending Aorta (AO)	Stagnation inlet	Pressure
LVAD	Mass flow inlet	Mass flow
Right Coronary (R-Cor)	Mass flow outlet	
Left Coronary (L-Cor)		
Right Carotid (RCA)		
Left Carotid (LCA)		
Right Subclavian (RSA)		
Left Subclavian (LSA)		
Right Vertebral (R-Vert)		
Left Vertebral (L-Vert)		
Descending aorta (DA)		

In StarCCM+, in order to define a CFD problem one must implement BCs defined at all the geometry boundaries. This software allows the user to split the imported geometry into separate boundaries and specify their nature (wall, mass flow inlet, pressure outlet, ect.). In addition, when the motion option is updated to Morphing, indicating any type of mesh deformation relative to specific region, morpher BCs must be specified. In the solid domain, it is assumed that axial displacement can be neglected, since the solid domain solver leads the simulation BC applied to the fluid domain can either be a boundary plane constraint (Figure 35) or floating. The first type of constraint indicates that elements' vertices can only move in the plane of the boundary (an infinite

plane which coincides with the chose boundary). This constraint is valid for all boundaries except for the LVAD, which is kept fixed.

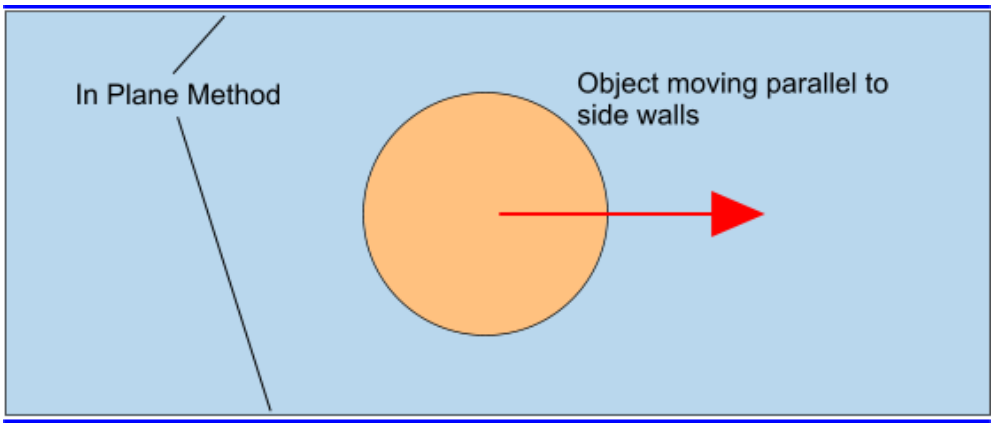

Figure 35 - Boundary Plane constraint [31].

The floating boundary constraint allows the vertices at the boundaries to move according to the displacement imposed by the displacement vector field imported from Abaqus and applied by the morpher interpolation. This approach decreases the chances of heavy mesh distortion near the boundaries as well as avoiding the amount of artificial displacement constraint the user has to apply to the model. Given the strong time-dependent response of the solid domain and subsequent mesh motion, local displacement may be unpredictable, especially in the initial phase to obtain a deformed and pre-stressed geometry. Hence in this study boundaries will be allowed to “float”.

3.8.2. Solid Domain Constraints

In the solid domain, it is assumed that radial displacements are in magnitude much larger than any axial displacement, hence the latter are neglected. To achieve this on a patient-specific geometry, a set of local coordinate systems (CS) have been defined at each boundary (Figure 37). The x-y plane is made coincident with the boundary plane and the tested BCs applied are of two types: the translation/rotational type and

axisymmetric type. Each CS has been placed in the approximate center of the vessel lumen.

To define these local CS, we first partition the internal vessel lumen edge in 2 parts. Using the two opposing points generated we define a midpoint between the two edge points. This midpoint will be the origin of the local CS. To ensure the CS is independent of the geometry, it is necessary to retrieve the midpoint coordinates and use them to separately generate a new reference point. Based on the latter we can generate a Cartesian system and use boundary nodes to define the x-y plane. This process is carried out for each inlet/outlet.

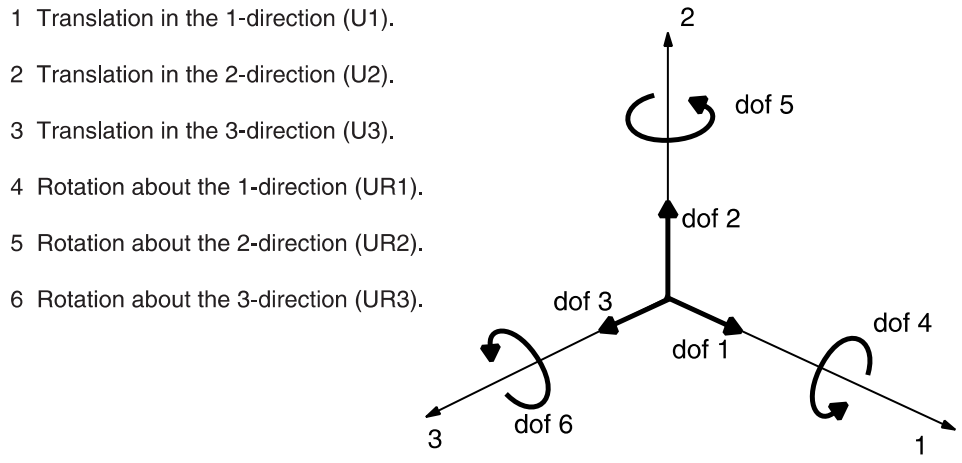

Figure 36 - Displacement and rotational degrees of freedom [32].

In figure 36, 1-direction being the x-axis, 2-direction being the y-axis and the 3-directoin being the z-axis. In Abaqus this scheme allows to constrain the model in each degree of freedom (DOF). To ensure planar displacement only, all but DOFs 1 and 2 have been defined as zero.

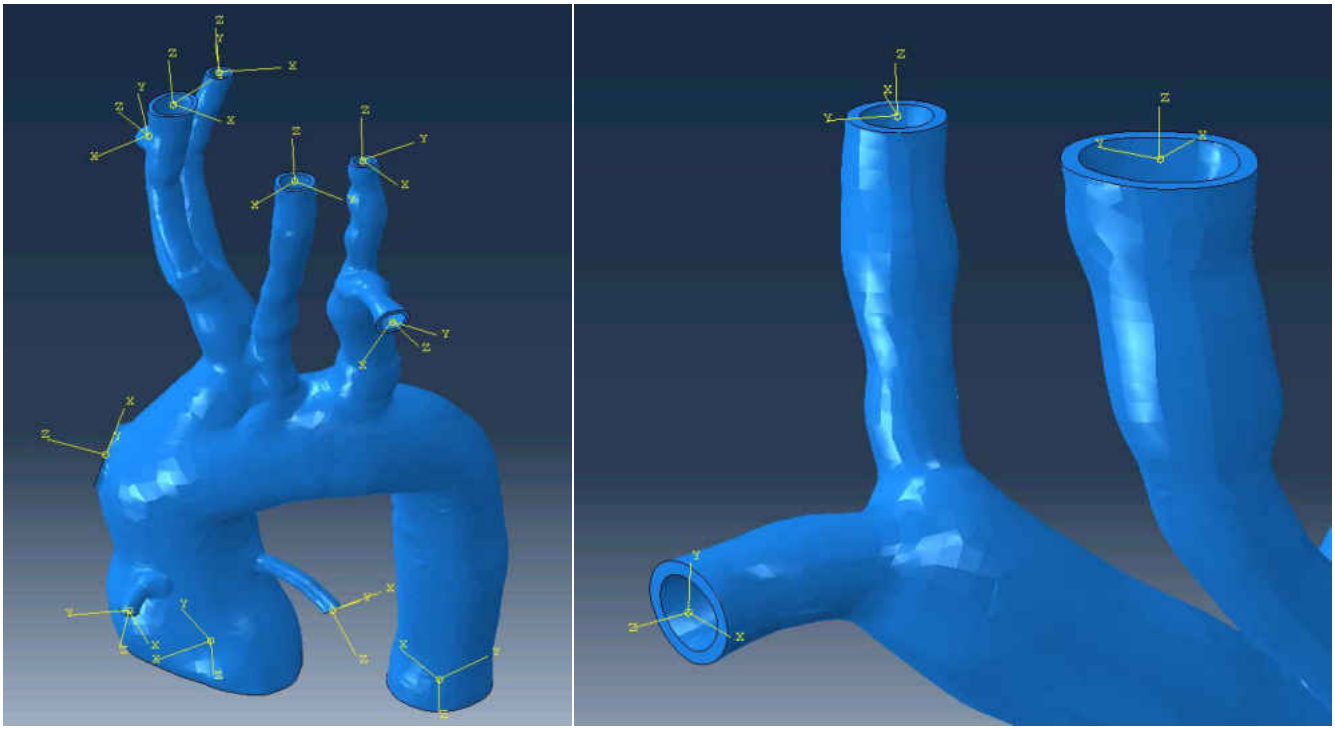

Figure 37 - Global view of local CS (left) and close-up on right cerebral vessels (right).

All boundaries at the exception of the LVAD boundary have been defined with planar constraints. For the LVAD the boundary is completely restricted (pinned) to reflect rigid nature of the cannula and respect the coupling condition with the fluid domain. Table 5 presents a summary of all solid domain BCs.

Table 5 - Generic FE displacement/rotational and axisymmetric boundary constraint conditions.

Boundary	U1	U2	U3	UR1	UR2	UR3
Ascending Aorta (AO)	↑↓	↑↓	0	0	0	0
LVAD	0	0	0	0	0	0
Right Coronary (R-Cor)	↑↓	↑↓	0	0	0	0
Left Coronary (L-Cor)	↑↓	↑↓	0	0	0	0
Right Carotid (RCA)	↑↓	↑↓	0	0	0	0
Left Carotid (LCA)	↑↓	↑↓	0	0	0	0
Right Subclavian (RSA)	↑↓	↑↓	0	0	0	0
Left Subclavian (LSA)	↑↓	↑↓	0	0	0	0
Right Vertebral (R-Vert)	↑↓	↑↓	0	0	0	0
Left Vertebral (L-Vert)	↑↓	↑↓	0	0	0	0
Descending aorta (DA)	↑↓	↑↓	0	0	0	0

This FSI coupling allows for the solid domain to move in the all degrees of freedom, hence entire vessel may experience bulk motion. In particular, bulk motion becomes accentuated at the boundary, therefore to limit boundary vessel motion a parallel combination of spring and dampers are introduced at each boundary (Figure 38). Each node at the external edge of a boundary is grounded by said constraints and allowed to move in the 6 DOF imposed by the local coordinate system. Table 6 summarizes the values for stiffness and damping at each boundary.

Table 6 - Boundary constraint spring/damper constants.

Spring Stiffness K [N/mm]	Damping Constant C [N/mm/s]
0.1175	0.000275

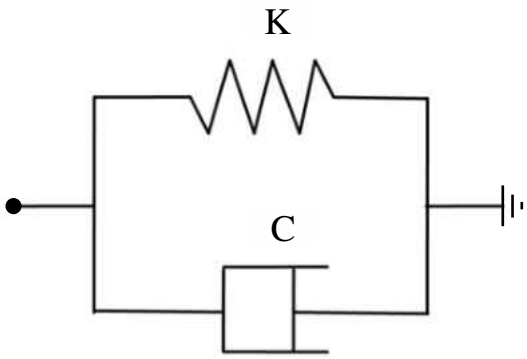

Figure 38 - Parallel spring/damper grounded constraint.

Figure 39 shows the spring/damper constraints applied at the LSA on the outer perimeter of the boundary, grounded by the local CS. In addition, the reference points used to generate the x-y plane of the local CS can be seen.

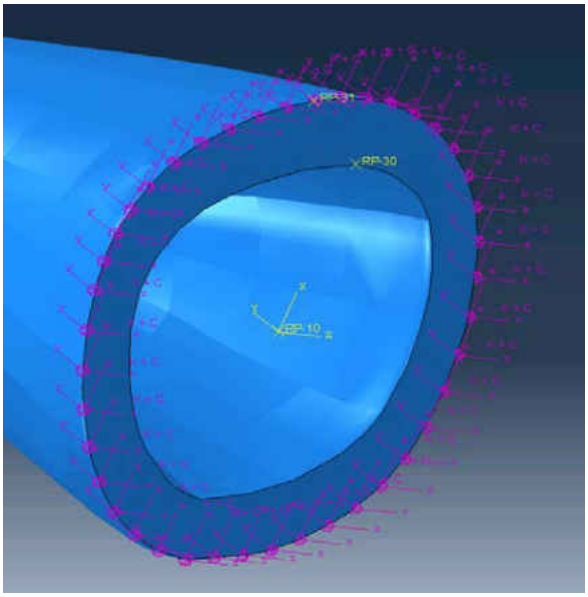

Figure 39 - LSA spring/damper constraint relative to local CS.

Given the complex topology, the magnitude of the normal loads applied by the fluid unto the interface and the proximity of vessels, there is the strong likelihood of vessel-vessel contact. This interaction must be modelled to ensure that first the meshes do not intersect causing nodes to and elements to overlap leading to a solver failure. Moreover,

this interaction leads to a whole new type of observed phenomenon that can be allegorically described as a “vessel thumb-war”. To regulate this interaction the outer surface of the arterial wall was set to be not-self intersecting with a hard contact collision model. This model essentially ensures minimal element overlap upon contact based on node distance residuals.

3.9. Fluid Structure Interaction

Once each portion of the full-scale simulation has been set up, the multi-dimensional coupling scheme must be approached. A compete schematic of the flow loop is provided below which displays an implicit time-step based coupling for the CFD-FEA 3D model and a cardiac cycle based 0D – 3D coupling. Abaqus and StarCCM+ have simple protocols to share data regarding pressure (from CFD to FEA) and nodal displacement (from FEA to CFD) based on a user defined time-step specification. A no-slip condition (63, 64) is maintained at the fluid–solid interface (Γ) where stresses are equal and the interface position is computed as $x_\Gamma = x_{ref} + D_\Gamma$.

$$u_\Gamma = \frac{d}{dt}(D_\Gamma) \tag{63}$$

$${\sigma_\Gamma}^s \cdot \hat{n} = {\sigma_\Gamma}^f \cdot \hat{n} \tag{64}$$

At the end of each 3-D coupled simulation (which may include up to 3 cardiac cycles) a java macro regulates the coupling between the LPM and CFD by: 1) exporting flow rate and pressure across the fluid domain, 2) computing domain resistance (4), 3) updating CFD domain resistances in the LPM, 4) solving the system of ODEs and 5) returning the resulting BC to the CFD.

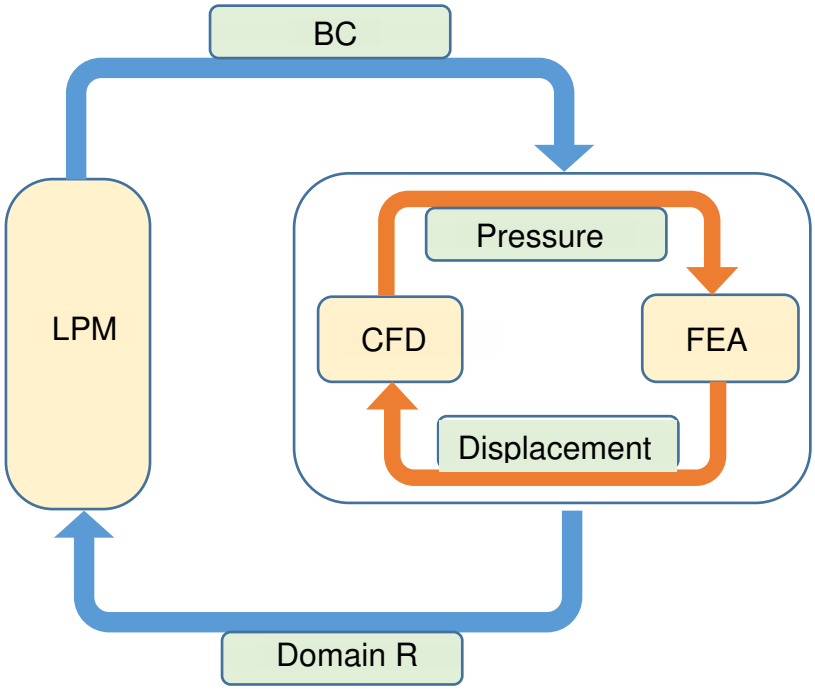

Figure 40 - Multi-scale model schematic.

3.9.1. Fluid-Solid Coupling

The entire simulation is intended to be unsteady, hence at time-step governs the discrete time increments to the total physical time. StarCCM offer adaptive time stepping schemes based on the CFL criteria as well as constant time-step settings. The latter is used to maintain the Courant number close to one in order to achieve time accurate CFD solutions. The fluid-solid coupling is set to be implicit to ensure stability since an explicit approach would strongly depend on the choice of time-step, resulting in a severe restriction on the time step. The implicit coupling allows the partitioned solvers to exchange data multiple times within a time-step adjusting the loads and calculated displacement at the interface to get a converged solution at the time-step level. The Aitken Relaxation scheme can be used to under-relax the FSI coupling and regulate stability. Since the problem is partitioned, each solver run independently allowing the user to

specify a separate sub-time-step in Abaqus. Figure 41 (top) shows the generic scheme in which Abaqus leads the simulation by (1) resolving the interface loads and deforming the wall domain, (2) mapping interface displacements to the fluid domain which (3) solves the flow field in StarCCM+ and (4) returns the loads at the interface back to Abaqus. It must be emphasized that both data streams may be under-relaxed separately.

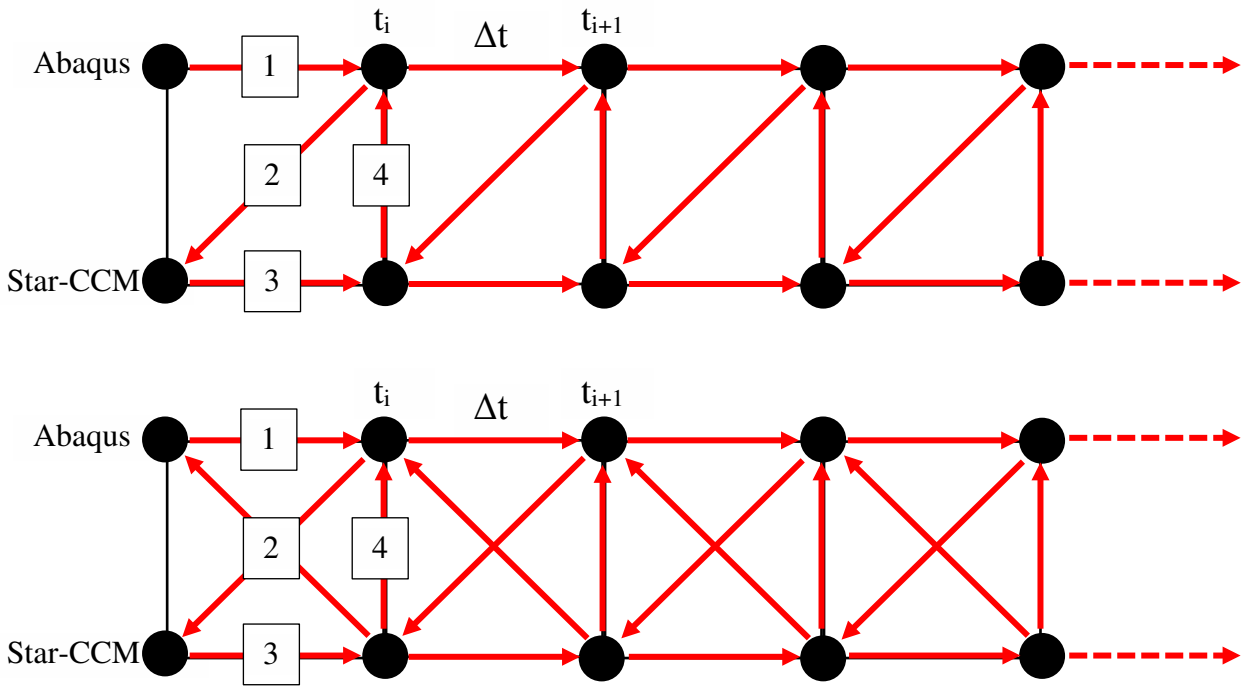

Figure 41 - Generic coupling scheme (top) and implicit coupling scheme (bottom).

The implicit coupling is shown in Figure 41 (bottom) and it regulates the sub-time-step data exchange (2). The user may control the exchange frequency depending on the solution stability and to optimize computational expenses.

As mentioned the need for FSI in this type of studies is justified in part by the fact that the wall loads generated by having a rigid geometry result in overestimation. This aspect has strong repercussions when initiating the coupling due to inertial effects, high wall compliance and other such quantities. As these exaggerated interface loads are

relayed to Abaqus the resulting displacements are heavily overestimated and may excessively distort both fluid and solid meshes. Beyond under-relaxation StarCCM+ offers the option of regulating the export of the traction field by applying pressure ramping within a time-step (Figure 42).

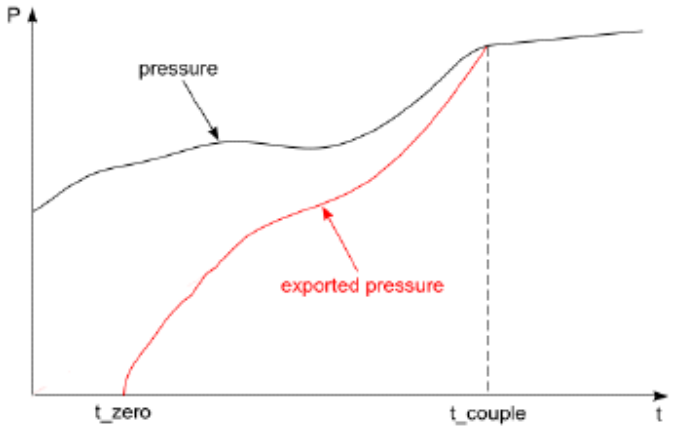

Figure 42 - Pressure ramping scheme [31].

Where for $t_{zero} < t < t_{couple}$ the pressure and shear stress are interpolated between 0 and the final value computed in StarCCM+. This allows Abaqus to smoothly adjust to the interface loads in the initial stages of the simulation where excessive loads are present.

A similar ramping approach can be applied within Abaqus as the applied load amplitude can be ramped throughout a time-step. This command is issued in the input file as *amplitude=RAMP.

3.9.2. Mapping

The fluid-solid interface surface mesh is not conformal in this study given the difficult topology, hence mapping may not be straightforward.

StarCCM+ offers a variety of mapping techniques suitable for surface-to-vertex and surface-to-surface mapping. Among them, nearest neighbor mapping, least squares

interpolation, exact/approximate imprinting and shape functions. The approached used to map the FSI interface between Abaqus and StarCCM+ in this case was chosen to be based on shape functions.

The shape function scheme is applicable only for tetrahedral and hexahedral meshing elements when working in 3D. As we map with shape functions from an Abaqus mesh to a STAR-CCM+ mesh, STAR-CCM+ recognizes the element type in the alien mesh and uses the applicable shape function for interpolation. When interpolating from Abaqus, StarCCM+ can project all the nodes in a high-oder element (in our case quadratic). However, the reverse map is achieved only with the element vertex nodes (finite volume mesh).

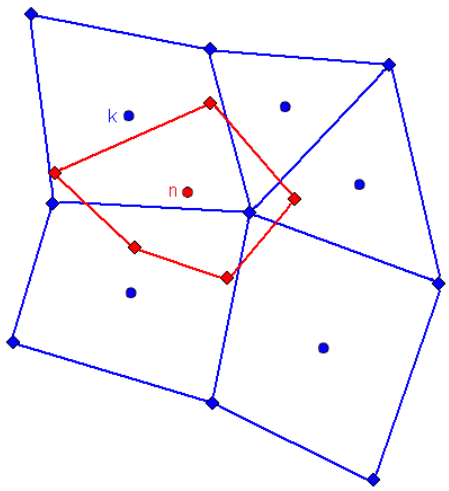

Figure 43 - Interface mesh mapping, the blue mesh is being mapped to the red one [31].

Given Figure 43, consider mapping data from vertices of the blue source mesh to faces of the red target mesh using shape function interpolation. Note that the element with centroid *n* of the receiving mesh lies within the boundaries of the element with

centroid *k* in the pilot mesh. The general formulation of the shape function interpolant is of the following form:

$$T_n = \sum_{m \in N(k)} T_m N_m(\xi_n, \eta_n, \chi_n) \tag{65}$$

where *N* is the shape function relative to the *n* element coordinates (ξ_n, η_n, χ_n) in the *k* element and *T* is the interpolated quantity. When mapping the user can control the initial mapping by defining a "search distance" which the solver uses to generate a mapping interface.

3.9.3. Morphing

In StarCCM+ when applying morphing to a mesh domain, a set of control vertices associated a displacement vector is created. The user can manipulate the percentage of control vertices used in each time-step as well as make the scheme adaptive. This determines the accuracy as well as the computational expense involved in this operation.

Multi-quadratic theory is implemented to generate interpolations fields based on imported displacements used by the morpher to deform the native mesh. A system of equations based on known displacements for each control vertex is created to define the interpolation field. The vertex-level displacement is expressed as radial basis function interpolation:

$$d_i' = \sum_{j=1}^{N} f_{b,j}(r_{ij})\lambda_j + \alpha \tag{66}$$

$$f_{b,j}(r_{ij}) = \sqrt{{r_{ij}}^2 + {c_j}^2} \tag{67}$$

where $r_{ij} = |x_i - x_j|$ defines the distance between to vertices, $f_{b,j}$ (with $c_j = 0$ in StarCCM+) is a radial basis function, x_i the position of a vertex, N is the number of control

vertices and α satisfies the condition $\sum_{j=1}^{N} \lambda_j = 0$. The linear system of equations is then solved for all $f,\ \lambda\ and\ \alpha$.

Morphing retains good accuracy even for large displacements as long as no negative volumes result from the deformation. When negative volume cells appear, remeshing is required.

3.10. Investigation

This study will be divided in 3 phases, one in which the multi-scale model is operated to obtain a settled periodic sustained solution (and a consistent flow field), a following in which the FSI coupling is activated to generate the pre-stressed geometry and one in which the Lagrangian model is implemented to release particles and tracked throughout the domain. The method described provides for a stable multi-step experimental procedure that can be repeatedly carried out for various patients, with the ultimate goal of supplementing the surgical planning process.

In Table 7 there is summary of the element count for each mesh region (solid and fluid).

Table 7 - Mesh report.

Region	Elements	Element type
Fluid	975481	Tetrahedron
Solid	432000	Quadratic Tetrahedron

After the pre-stressed configuration is attained, the fluid domain may require remeshing. Again, tetrahedral elements were employed due to the highly irregular topology and base size were matched at the interface surface to facilitate nodal mapping.

High flow resolution is critical at the interface for a FSI, hence the computation cost incurred in a localized element count increase is justified by a potentially more stable solution.

Hypothesis: This study aims at determining whether FSI is necessary in studies aimed at determining optimal implantation configuration for the outflow cannula graft in order to reduce stroke risk. Hence the second and third phases are the most important: when the FSI and Lagrangian schemes are activated. As mentioned previous particles are released from selected locations other investigations revealed to be the known origins as each of the following locations: (1) the VAD itself, (2) dislodged clots from the aortic root walls, (3) or the native ventricle [2,4]. Particles are introduced by injection grids placed in the cannula and the aortic root (Figure 44).

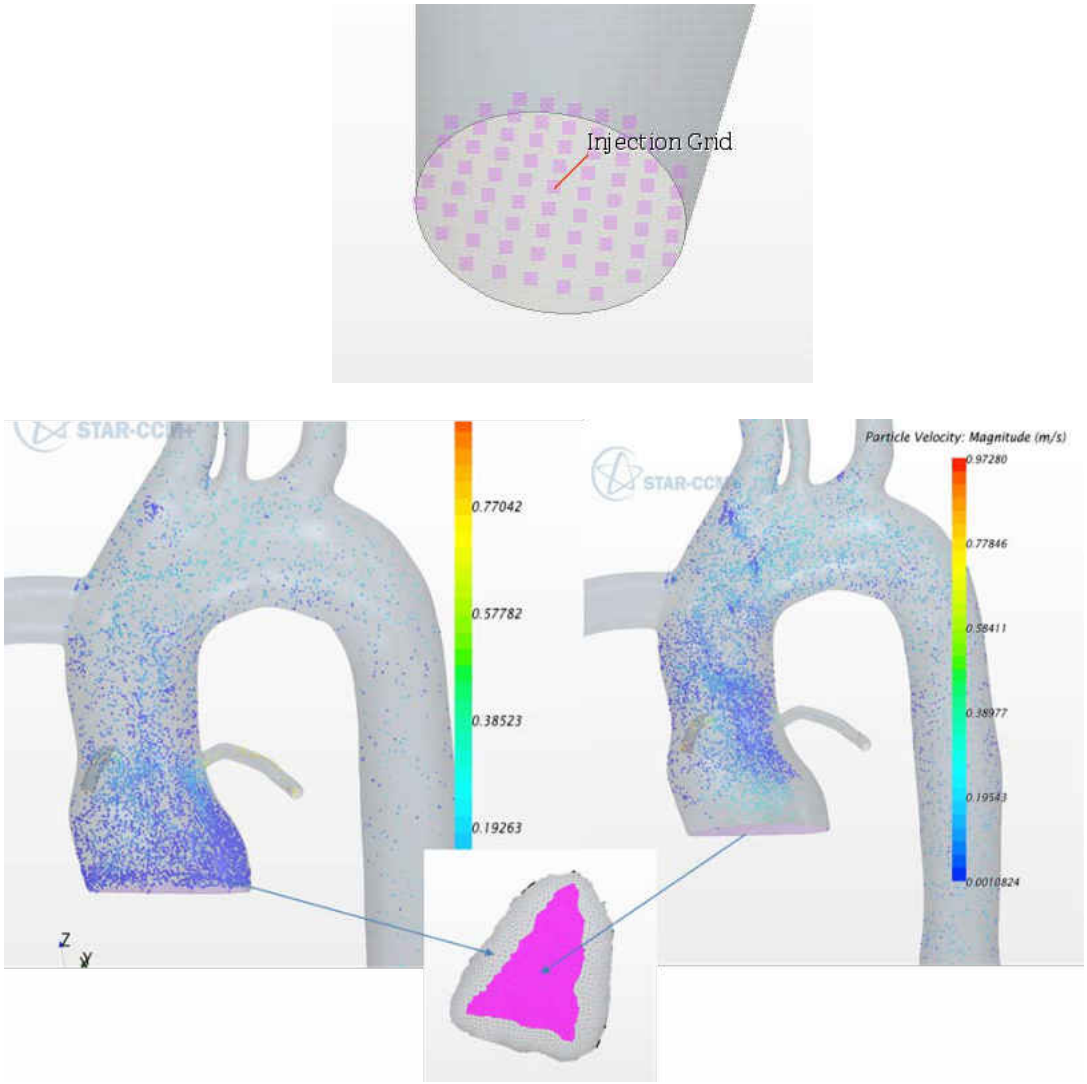

Figure 44 - Cannula injection grid (top) and aortic root injection scheme (bottom).

Due to geometrical simplifications, our geometry does not include the portion of the aortic root directly attached to ventricle housing the aortic valve hence we apply a specific flow profile to particle generating at the base of the aortic root dependent on the aortic root blood velocity. In an annular region extending from the aortic walls particles are released with zero initial velocity to simulate particles dislodging from the wall while in an internal circular region equal, in size, to the open valve diameter, emboli are released with a turbulent (uniform) velocity profile as if generating from the ventricle itself.

StarCCM+ expresses the per-node grid release of a particle through a probability function (point inclusion probability). For particles released at either the VAD or the aortic root wall this value is set to a constant (between 0-1). For ventricular ejection, however one must account for aortic valve closure. Equation 68 employs local pressure measurements versus valve opening pressure to introduce an artificial valve effect on the Lagrangian phase and is formulated as

$$p_t = p_o \left[ceil \left(\left(\frac{max(P_{aortic\,root}(t), P_{critical})}{92} \right) \right) - 1 \right] \tag{68}$$

where p_o is the nominal probability, $ceil$ is a function to round up a value and p_t is the transient probability.

Spatial randomness is dictated by the point inclusion probability that determines how many nodes in the grid will be injecting a particle at each time-step which can be re-randomized at each time-step. Randomness in time is introduced by generating a time-dependent particle release table.

3.11. Statistical Analysis

In this study, the statistical analysis will be carried out in two steps: first the body of data relative to thrombus transport will be elaborated to produce means and standard deviations to show consistency throughout runs and compare geometries then the pooled statistics were compared to similar solutions carried out with steady state rigid wall simulations and unsteady rigid wall simulations.

Each run produced concise tables of particle transition at every outlet including data recording particle injection into the domain. Particle percentages were then computed with the following expression:

$$Particle\% = \frac{number\ of\ particles\ at\ outlet}{number\ of\ all\ outlet\ particles} 100 \quad (69)$$

Once all runs were analyzed, for each particle size and geometry means and standard deviation were evaluated for each outlet and specifically cerebral vessels a statistical method comparing two means was employed to compare steady state simulation and unsteady simulations results to determine whether steady modeling would suffice in order to engage in depth studies on stroke incidence.

The Z-score was calculated based on the probability of a clot transitioning through carotid and vertebral arteries in the steady and unsteady cases as:

$$Z = \frac{\mu_1 - \mu_2}{\sqrt{p \cdot q\left(\frac{1}{n_1} + \frac{1}{n_2}\right)}} \quad (70)$$

$$p = \frac{\mu_1 n_1 + \mu_2 n_2}{n_1 + n_2} \quad (71)$$

Where $\mu_1$and $\mu_2$represent the means of the two populations, $n_1$and n_2 represent the populations sizes, p is the overall probability and $q = 1 - p$ [33]. The Z-score is intended to quantify the amount of deviation from a mean based on standard deviations. In a normal distribution 68% of a population resides within a standard deviation, 95% of a population resides within two standard deviations and 99.7% of a population resides with three standard deviations. A representation of such a distribution in captured in Figure 45. The formal expression found in Equation 70 is intended to make inferences of two different populations considering their proportions. More precisely this approach offers a comparison of a random sample collected from each population.

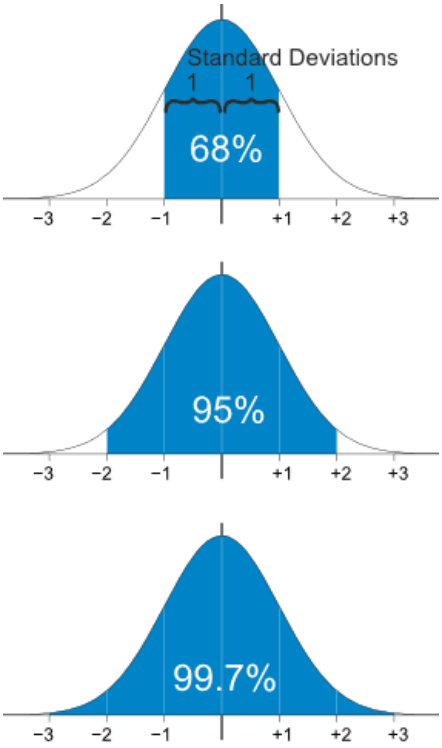

Figure 45 - Normal distribution bell curve.

We employ a two tailed, two means Z-score, which compares values from two different populations and determines criteria for comparison. A null hypothesis rests on the two populations being very similar, the alternative hypothesis having the two populations being different. A Z-score falling within the confidence interval dictated by standard deviation interval of choice would lead to the rejection of the alternative hypothesis.

Table 8 - Testing criteria for null hypothesis μ_1-μ_2=0.

Alternative hypothesis	Reject null hypothesis if:
$\mu_1 - \mu_2 \neq 0$	Z > 1.96 or Z < -1.96

3.12. Job Parallelization

Given the elevated element count for both the solid and fluid domains this simulation requires parallelization. The current Abaqus implementation for an implicit dynamic analysis using a direct sparse solver forced the adoption of different allocation scheme since only a single processor per compute node can be used. In other words, thread-based parallelization cannot be exploited. Once specified the designated machines to carry the simulation, to allocate a single processor per compute node a round-robin rule (RR) allocation scheme must be utilized instead to a fill-up rule. This means that assuming a job request for N number of slots on a cluster, the queuing system will go to the first machine and grab 1 slot if available, move the following machine and grab 1 slot if available, wrapping around all the designated machines multiple times if necessary to fill all N requested slots. Appendix A has a sample batch file employing this approach.

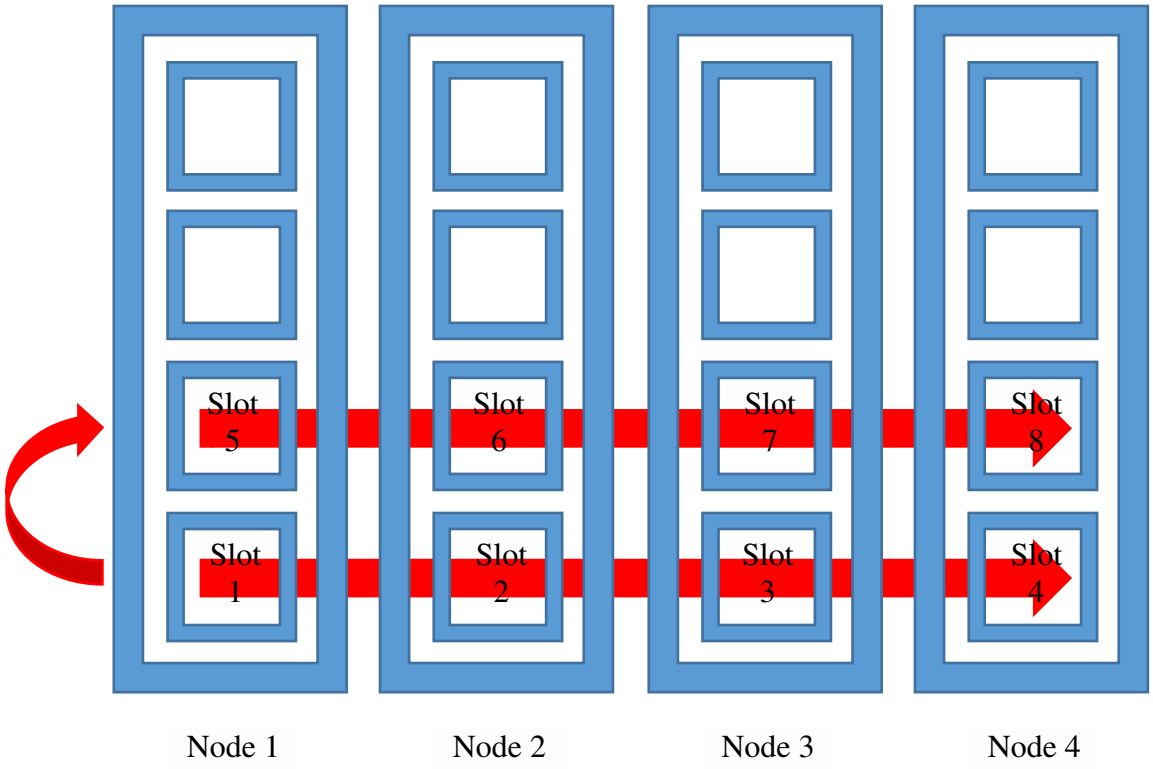

Figure 46 - Sample 8 slot RR rule allocation for a 4-machine cluster.

The command –pe mpich-rr N sets up the parallel environment implementing a RR rule for allocation where N indicates the number of CPUs the job requires. StarCCM+ is run as a server job by the command starccm+ once the correct module is loaded by invoking “module load starccm+/(StarCCM+ version)”, in addition to split and allocate the N number of slots to both Abaqus and StarCCM+ this command is followed by “–np m,n” (indicating the number of processors), where m are the slots given to StarCCM+ and n the slots allocated to Abaqus (hence m + n = N).

Before starting the simulation however, the Abaqus mp-hostlist should be specified otherwise the default will be generated by StarCCM+ which would employ a fill-up rule allocation for Abaqus. The host list is generated once the simulation is started but can be modified by a macro or by user input. Under Co-Simulations → Abaqus Co-Simulation [#]

→ Values → Abaqus Execution → Host List the user must specify host-name:1, where host-name refers to the compute node and 1 is the number of slots allocated (this may be automated by a macro). The user may also specify the domain-to-CPU split to impose to Abaqus which in turn determines the speed of the simulation. In the auxiliary files generated by Abaqus once the run is started, the user can see estimates relative to FLOPs per iteration and minimum memory requirements for each thread (sample found in Table 9).

Table 9 - Sample Abaqus job allocation statistics.

Process	Flops per iteration	Minimum memory required (Mb)	Memory to minimize i/o (Mb)
1	5.31E+11	758	2808
2	4.23E+11	695	2425
3	4.18E+11	754	2413
4	2.35E+11	629	2306
5	6.09E+11	755	2543
6	3.56E+11	662	2283
7	2.98E+11	582	2333

Once the simulation is started the Abaqus solver is initialized, the user can confirm a successful parallelization by consulting the abaqus_v6.env file which summarizes the Abaqus environment set up, in particular the CPU allocation on the cluster. Alternatively, to check appropriate slot allocation the user may log remotely into each machine separately and check for consistency the number of threads generated using the top command.

4 CHAPTER: RESULTS

4.1. Preliminary Results and Discussion

4.1.1. LPM

The tuned circuit provides output waveforms as BC to the CFD. In Figures 47-48 there is displayed a sample of all waveforms for 3 heart cycles. The case at hand is that of an acute heart failure with approximately 4-1 (L/min) flow ratio between LVAD and the LV hence the expected flow rates thought the model ought to show a significant residual flow even during diastole.

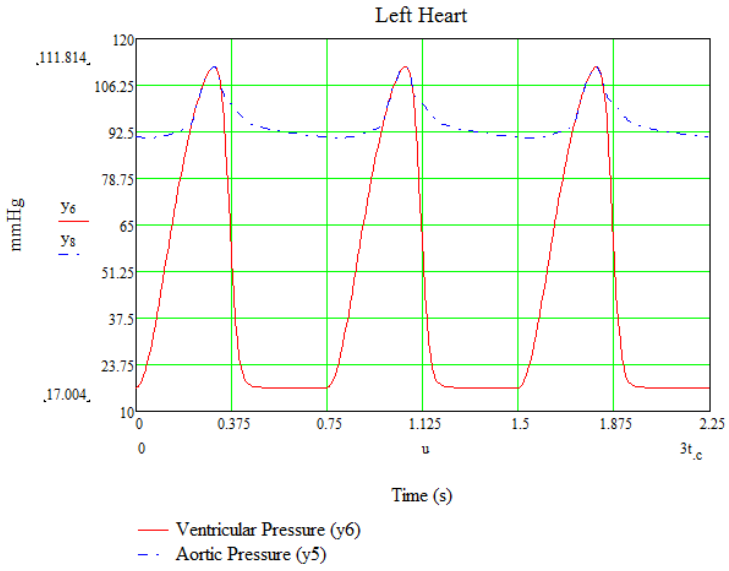

Figure 47 - Pressure waveforms for acute HF.

In a healthy individual, the ventricular pressure may typically vary between 100-140 mmHg during systole and 3-12mmHg during diastole while the aortic pressure may oscillate between 140-80 mmHg throughout the cycle. As the LV fails the ventricular pressure decreases leading to a reduction in aortic pressure and critically low flow rates

in the main vessels. The introduction of the LVAD supports the ventricle by incrementing the pressure head and returning the aortic pressure to a healthy value. In Figure 47 the additional pressure head provided by the LVAD shows to return the aortic pressure to the desired pressure interval as well as the failing left ventricle.

Given a continuous flow VAD, the flow rates expected at each of the cerebral vessels that would typically be averaging at zero in normal conditions are in fact experiencing mean flows during diastole. Figure 48 displays such a phenomenon for each of the main cerebral vessels taken into account in our CFD simulations (Carotids, Subclavian and Vertebral). Also for physiological correctness a flow split ratio of 70-30 % between left and right coronaries has been imposed as documented by Sankaran's group [34]. Also, the coronary arteries display out of phase flow with respect to other arteries which reflects physiological conditions. This is implemented via a non-linear resistance that is a function of the ventricular pressure that effectively allows coronary steal to occur in diastole.

It can be observed in Figure 47 that despite the acuteness of the HF, a degree of pulsatility is maintained in the circuit. For completely failed heat the native ventricle would not induce pulse waves into the VAD.

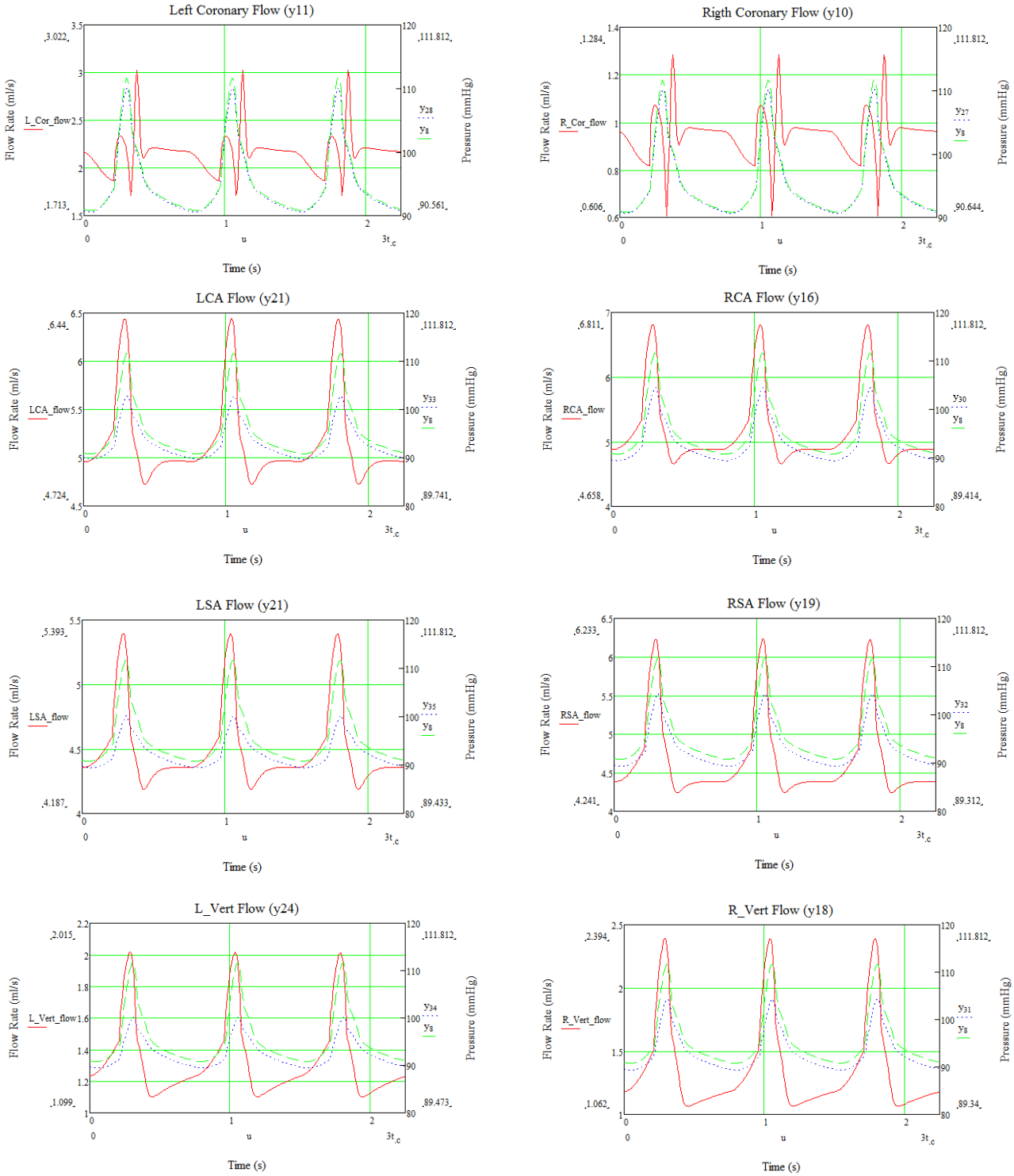

Figure 48 - Outlet waveforms provided by the LPM as BC to the CFD (LCA = Left Carotid Artery, RCA = Right Carotid Artery, LSA = Left Subclavian Artery, RSA = Right Subclavian Artery, L_Vert = Left Vertebal Artery and R_Vert = Right Vertebral Artery). In red the mass flow rate, in blue the local pressure and in green the aortic pressure.

4.1.2. Rigid Wall CFD

Preliminary runs for the LPM-CFD coupling have been conducted the verify convergence of flow fields and data have been collected for non-interacting particles released in a rigid domain from 3 prescribed regions. Table 8 summarizes the embolization rates for all the outlets present in the model. Data are separated for particle size and release location.

Figures 49-51 display a combination of stream lines and particles for the three different injection origins over a single heart cycle. The most important flow feature displayed is the oscillatory nature of the VAD jet due pulsatile flow generating from the native ventricle. As the jet oscillates, recirculatory flow becomes dominant in the coronary region causing particles to get trapped and potentially embolize to the coronaries. Coronary particle ingestion is induced by the fact that coronary flow increases in diastole as the jet flow impinges on the ascending aorta distal wall generating recirculation. As the cycle peaks in systole, the VAD jet is pushed towards the apex of the aortic arch allowing the jet to push particles towards the right-sided vessels and the descending aorta.

It can be observed particle originating in the VAD in peak systole can be directly aimed towards the distal potion of the arch (Figure 49). However, at the same time, the jet itself turns into a solid volume of fluid from which particles originating from the aortic root must either circumvent or punch through. Only particle with enough momentum would be capable of crossing the jet “cylinder”, namely the ones ejected by the ventricle (Figures 49-51). This could indicate that further studies aimed at incrementing jet momentum diffusion could be very beneficial for future VAD designs.

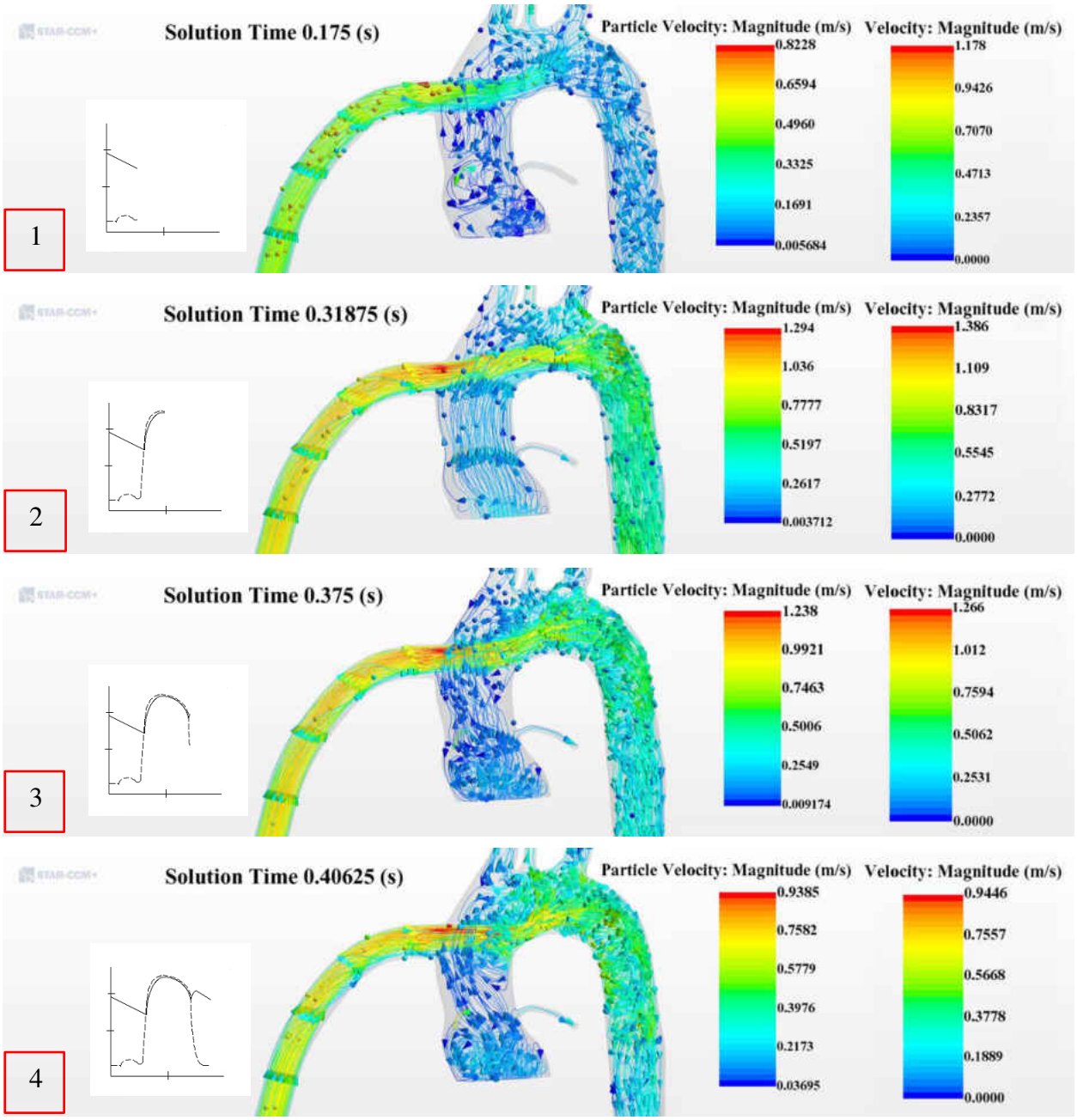

Figure 49 - 2mm particle injection emanating from the LVAD combined with streamlines.

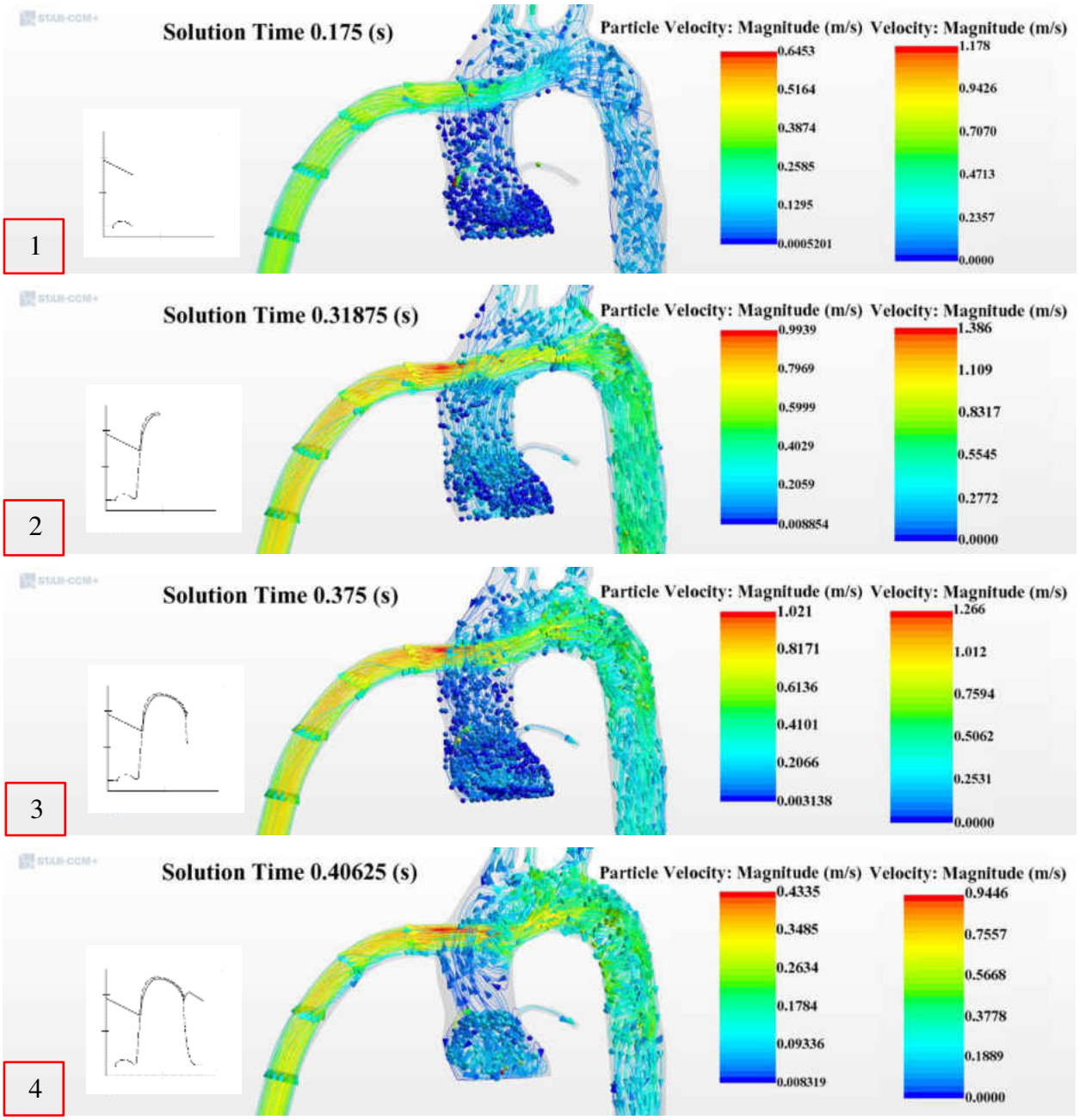

Figure 50 - 2mm particle injection emanating from the Ventricle combined with streamlines

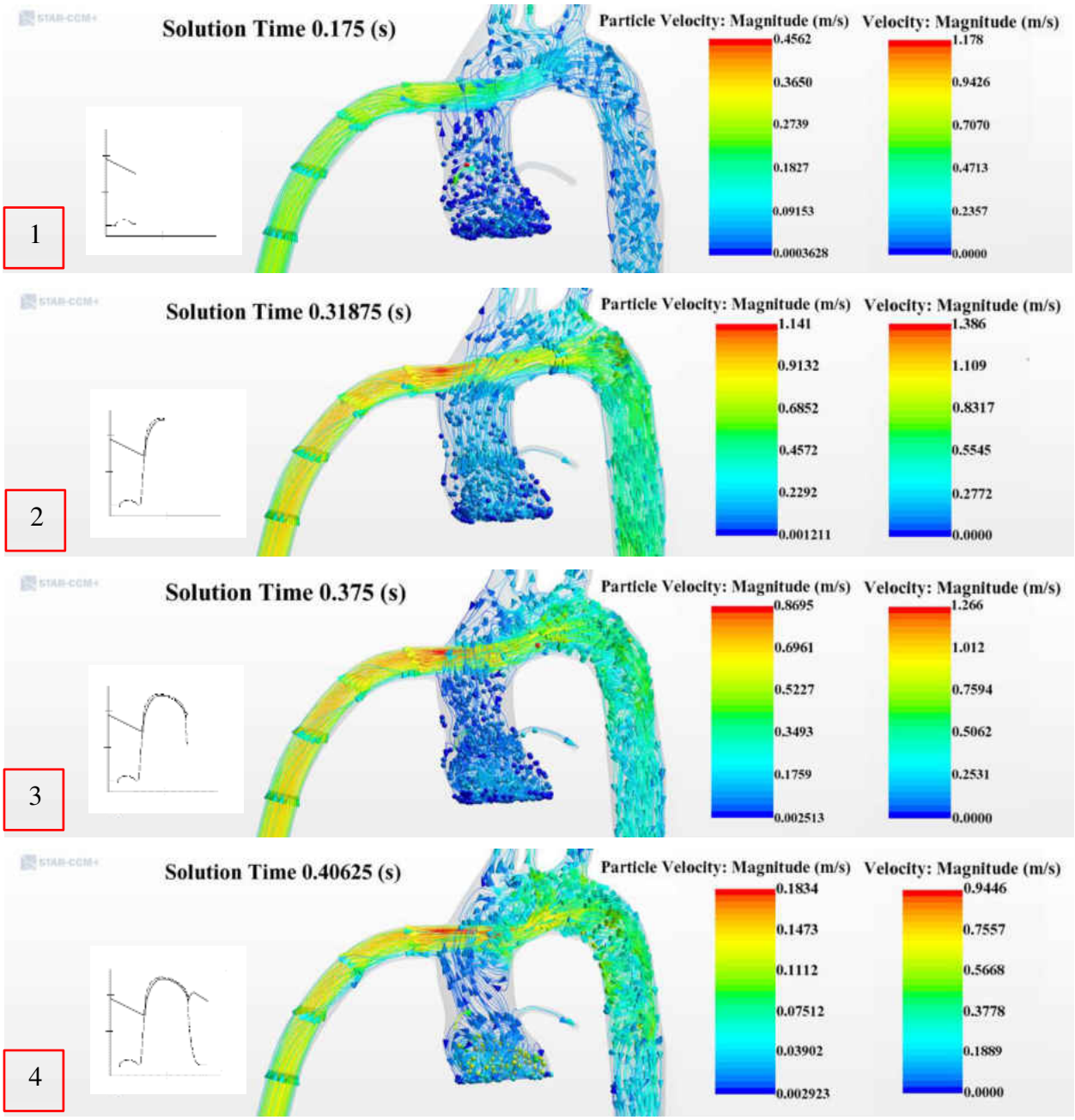

Figure 51 - 2mm particle injection emanating from the aortic root wall combined with streamlines.

In literature, it has been found that in patients implanted with LVADs, cerebrovascular lesions have a right hemispheric predominance [35]. Results provided in Table 10 do in fact show larger embolization rates for right-sided vessels for each release location. Also, due to the presence of the cannula jet, particle originating for the aortic

wall which simply dislodge (hence zero initial velocity) have significantly lower embolization rates to the cerebral vessels. Embolization rates for the coronaries are high for particles released from the AO root or the ventricle due to the proximity of the release origin as well as recirculation due to flow impingement. Inertial effects tied to particle size become evident for particles originating from the ventricle as embolization rates for 4mm particles are significantly larger than for 2mm particles. This could be due to the larger particles' momentum overcoming the jet induced recirculation flow patterns which prevents smaller particles to pass.

Table 10 - Preliminary data on embolization rates to cerebral vessels (DA=Descending Aorta, LcorA=Left Coronary Artery, RcorA=Right Coronary Artery, LvertA=Left Vertebral Artery, LCA=Left Carotid Artery, LSA=Left Subclavian Artery, RvertA=Right Vertebral Artery, RCA=Right Carotid Artery, RSA=Right Subclavian Artery) for 3 release locations (AR Wall=Aortic Root Wall, LVAD=Left Ventricular Assist Device, Ventricle=Ventricular ejection).

		DA [%]	LcorA [%]	RcorA [%]	LvertA [%]	LCA [%]	LSA [%]	RvertA [%]	RCA [%]	RSA [%]
AR Wall	2mm Particles	0.89	17.51	22.90	0.13	1.19	0.75	0.16	1.49	1.09
	4mm Particles	4.75	14.23	19.51	0.32	3.28	3.24	0.78	4.69	5.51
LVAD	2mm Particles	42.06	0.21	0.44	2.62	11.43	11.61	2.97	15.04	13.54
	4mm Particles	55.02	0.14	0.10	1.81	8.55	10.31	2.19	10.83	11.00
Ventricle	2mm Particles	15.25	37.08	10.88	1.14	7.84	4.82	2.43	10.24	10.03
	4mm Particles	16.50	28.06	2.30	1.22	10.15	5.32	3.31	15.58	16.94

4.1.3. Solid geometry modal analysis

Many non-conservative physical systems display a degree of energy dissipation due to material properties that may cause damping, induced by inertial, viscous or frictional effects, so does the aortic wall. Implementing damping in a model can be challenging as it can be difficult to identify all sources of damping, equation 59 includes the damping term with $[C]$ the damping matrix. In this particular case damping can be

mainly attributed to inertial effects (due to bulk motion of the solid) and to internal/viscous effects. It must be kept in mind however that surrounding tissues play also a major role in applying and alleviating mechanical loads. Two potential ways of accounting for the surrounding tissue is to model spring-damper constraints (Figure 38-39) for all surface nodes or to adjust the proportional contribution of mass induced damping to include additional energy loss. The Rayleigh damping model allows one to introduce mass-proportional and stiffness-proportional damping included in the damping matrix as in equation 72 where $[M]$ is the mass matrix, $[K]$ is the stiffness matrix, α the mass-proportional damping coefficient and β the stiffness-proportional damping coefficient.

$$[C] = \alpha[M] + \beta[K] \tag{72}$$

$$\xi_n = \frac{\alpha}{2\omega_n} + \frac{\beta\omega_n}{2} \tag{73}$$

In order to introduce damping, values for α and β have to be evaluated. These are related to the desired damping ratio and the modes of the structure (Equation 73). It can be observed material property contributes to the overall damping based on mode-frequency. As frequency increases the mass contribution drops while the stiffness contribution grows and the expression then reassembles a linear curve (which would justify the application of a linear interpolation for damping ratio at higher modes). By means of Abaqus a separate simulation intended to extract the eigen-frequencies and eigen-modes of the structure was carried out. Appendix D has a sample of the simulation step set up to compute for the first 60 modes. The frequency of the first mode was found to be 5.57 Hz while the last mode investigate was found to be 141.1Hz. Only the first 6-15 natural frequencies are typically of importance for most engineering structures, but

nevertheless the evaluation of the damping coefficient will be applied using the all modes. By means of equation 73 the damping coefficients can be evaluated by comparing a linear interpolation of the damping ratio to the frequency with a damping ratio obtained from computed damping coefficients on various mode ranges.

$$\xi_i = \frac{\xi_m - \xi_1}{\omega_m - \omega_1}(\omega_i - \omega_1) + \xi_1 \tag{74}$$

The linear interpolation based damping ratio is obtained using equation 74 for a chosen damping ratio ξ_1 on ω_1 and ξ_m on the mth relevant natural frequency. Once the values for this baseline case have been evaluated, to better model damping at higher frequencies the damping coefficients can be computed for increasing ranges of frequencies $(1 < m < 60)$. In appendix B, tables 14 and 15 contain the full set of data relative to the modal analysis for isotropic and anisotropic materials.

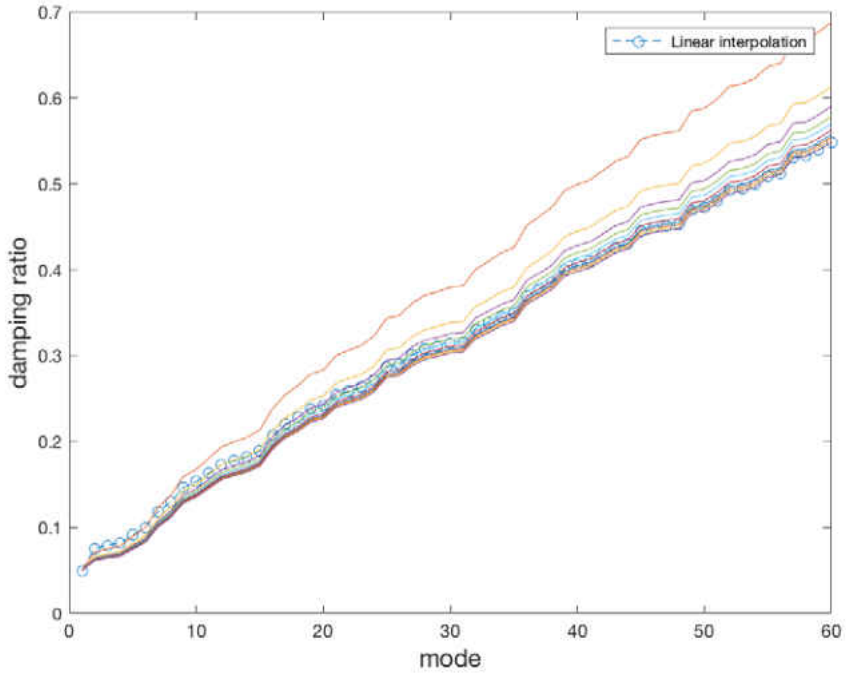

Figure 52 - Damping ratio approximation for 10 different damping coefficient values for an isotropic material.

Figure 52 shows a comparison between the linear interpolation for given damping ratios at set frequencies and damping ratio for larger mode ranges. As the mode inclusiveness is incremented, the damping coefficients yield curves closer to the linear interpolation. The mean difference for damping ratio at each mode can be computed to find which coefficients best fit the linear interpolation.

Table 11 - Damping coefficients for various mode ranges for an isotropic material model.

Mode interval	$\alpha \left[\frac{1}{s}\right]$	$\beta\ [s]$	Mean deviation
1-6	1.60034	0.00155	0.06738
1-12	1.80762	0.00138	0.02787
1-18	1.87197	0.00133	0.01704
1-24	1.90440	0.00130	0.01237
1-30	1.92698	0.00128	0.00981
1-36	1.94785	0.00127	0.00845
1-42	1.96174	0.00126	0.00811
1-48	1.96993	0.00125	0.00832
1-54	1.97894	0.00124	0.00908
1-60	1.98687	0.00123	0.01032

Table 11 summarizes the computed values for the damping coefficients for various ranges and the associated mean deviation for the linear interpolation data. For a range spanning 1-42 modes, it appears that the deviation can be minimized to 0.00811 for $\alpha = 1.96174$ and $\beta = 0.00126$. In addition, the chosen mass-proportional damping coefficient while minimizing the mean deviation also imparts additional damping to the structure which could account for the surrounding tissue induced damping. If necessary the values can be further refined by reducing the interval size.

A similar analysis is conducted for the anisotropic material to determine the optimal damping coefficient values. The same number of modes was considered.

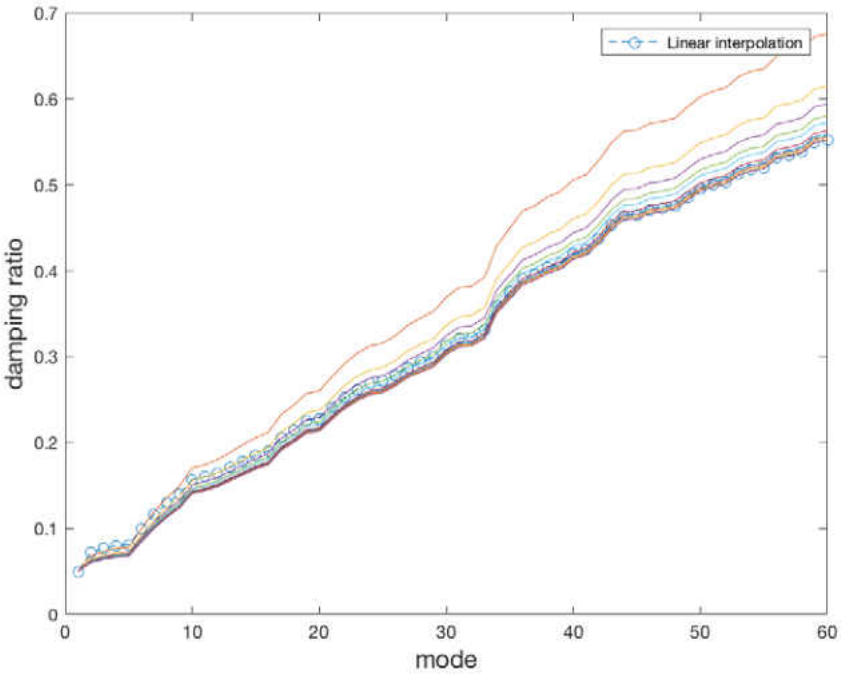

Figure 53 - Damping ratio approximation for 10 different damping coefficient values for an anisotropic material.

Figure 53 shows a similar trend compared to the isotropic material model. Variability appears decreased most likely due to the presence of fibers in the arterial wall which oppose any tension load developed in the analysis. Table 12 summarizes the computed damping coefficients for the anisotropic material model for various modal ranges. Again, the aim is to minimize the deviation from the linear interpolation obtained from user defined damping ratio at a chosen mode. The deviation can be minimized for a range spanning 1-42 modes, to 0.00763 with coefficients $\alpha = 1.96174$ and $\beta = 0.00126$.

Table 12 - Damping coefficients for various mode ranges for an anisotropic material model.

Mode interval	$\alpha \left[\frac{1}{s}\right]$	$\beta\ [s]$	Mean deviation
1-6	0.5169	0.00428	0.06039
1-12	0.5821	0.00413	0.02797
1-18	0.6051	0.00403	0.01783
1-24	0.6199	0.00398	0.01218
1-30	0.6284	0.00391	0.00974
1-36	0.6384	0.00389	0.00789
1-42	0.6426	0.00387	0.00763
1-48	0.6456	0.00385	0.00776
1-54	0.6482	0.00384	0.00837
1-60	0.6501	0.00428	0.00914

4.1.4. Arterial Wall pre-stressing and equilibrium

Once the appropriate damping coefficients have been evaluated the FSI solution must be run preliminarily to generate the residual stresses in the arterial wall. This becomes necessary also since the solid region involves a dynamic implicit solver which would yield an equilibrium state for the coupled geometries and this model presents a non-negligible vessel-diameter variability (given that we have both vessel distention and contraction along with structural bulk motion). The large disparity in adjacent vessel diameters can generate very complex combinations of conduit expansion, contraction and bulk motion. An example of this are the coronary arteries which bifurcate from the aortic root. The structure in this region experience a sudden change of diameter, from ~24.23mm to ~2.98mm leading to a sharp vessel thickness decrease. Any radial expansion or contraction experience in the aortic root can induce a bulk motion of the coronaries. Similar observations ca be made about other branching vessels.

The geometry obtained from CT-scans is assumed to be sampled during diastole, hence the loads applied to the solid geometry are introduced by applying BCs for diastolic mass flow rates and pressures. The BCs are kept constant throughout the run as the flow field adjusts to the interface movement. The loads applied at the interface are not user-defined in the FEM-solver, they develop as the flow field settles while the fluid-solid equilibrium is reached. Hence these loads vary axially and azimuthally throughout the model geometry. In order to monitor the simulation and ensure equilibrium, pressures and flow rates are sampled at representative cross-sections in all conduits (such as in Figure 19). The simulation is then allowed to run until all measured quantities display no fluctuations due to fluid-solid interface motion.

The result of this pre-stressing process is displayed in Figure 54 for both pressure and mass flow rates. It can be observed how due to dynamic fluid-solid coupling the measured quantities display strong fluctuations due mostly to conduit contraction and expansion. After approximately 0.4s, the model no longer experiences large radial-deformation induced variation.

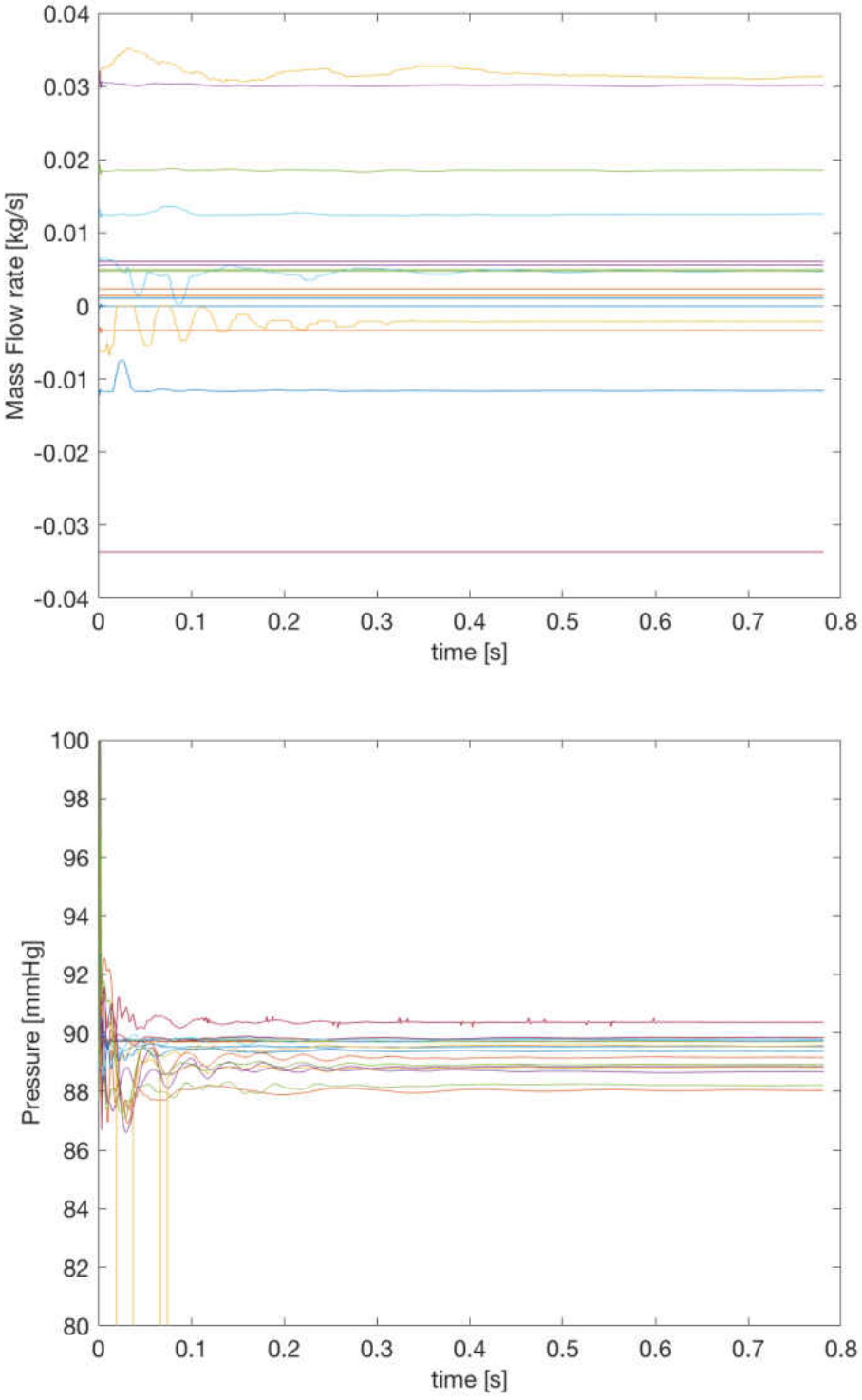

Figure 54 - Cross-sectional mass flow rates (top) and pressures (bottom) during pre-stressing process.

However, it must be noted that while local radial deformation subsided after ~0.4s, bulk motion is still partially present due to some residual periodic inertial motion (Figure 55). Although bulk motion is non-negligible, it hardly affects the flow field at equilibrium. In the first portion of the simulation, the structure experiences a mild momentum build up as the loads are applied. This in turn generates as previously mentioned complex bulk motions as a result of the vessel segments interactions.

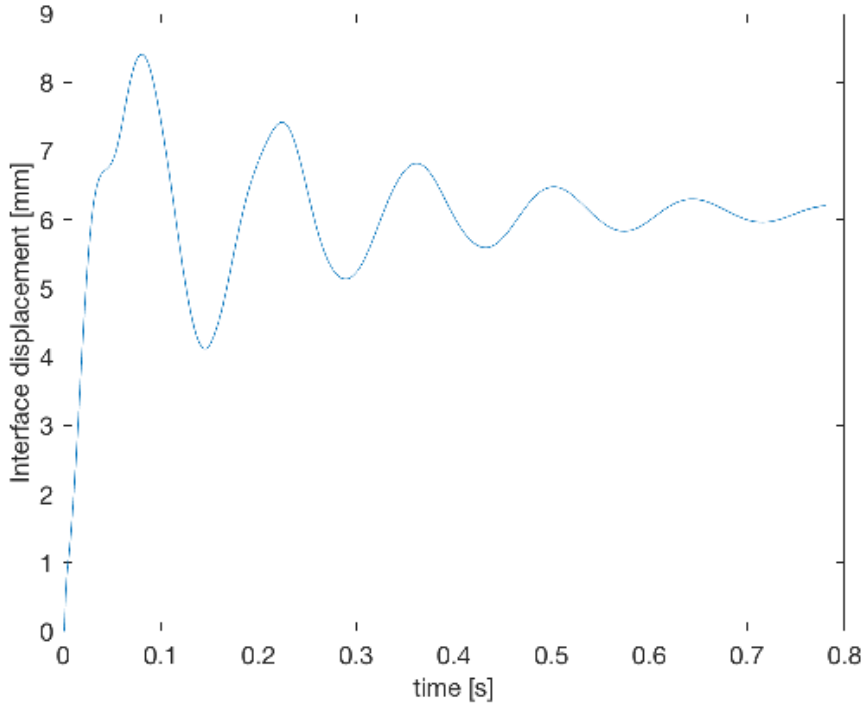

Figure 55 - Fluid-Solid interface average nodal displacement during pre-stressing process.

The example of the coronary-aorta “push and pull” is a clear illustration such motions. Similarly, to a lesser the degree upper vessels experience a bulk motion induced by the bulk motion and radial expansion of the aortic arch. It is important to observe that the motion imparted by the aortic arch generates twofold complex motions at each bifurcation. Interactions between vessels can be categorized as parent-child and child-

child (Figure 56). Innominate artery, (right and left) carotid artery, (right and left) subclavian artery, (right and left) coronary and (right and left) vertebral artery are all the conduits involved in such interactions.

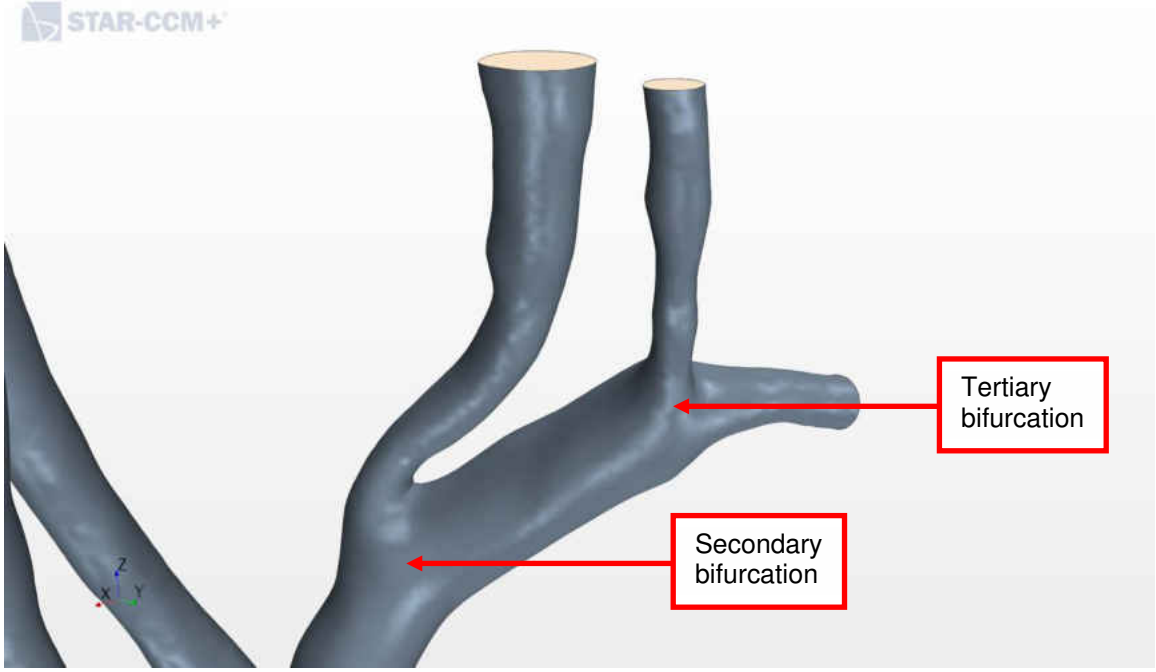

Figure 56 - Right upper vessels bifurcations (right carotid artery, right vertebral artery and right subclavian artery).

Figure 57 offers some insight on the degree of bulk motion experienced by the solid geometry focusing on the coronaries and the upper right vessels. The left coronary artery has shown to move for up to 6mm for its original position while the right subclavian and right carotid were displaced up to 20mm. Such large displacement is due to the displacement build up at each bifurcation and the dynamic behavior of the structure reaching equilibrium. In section 3.7.2, the surface hard contact set up was outlined to regulate any outer wall interaction.

Figures 58 reveals another interesting aspect of the solid model, the contact modelling implemented is shown to be successful as the right carotid artery collides with

the segment spanning from the secondary to the tertiary bifurcation without causing the mesh to overlap.

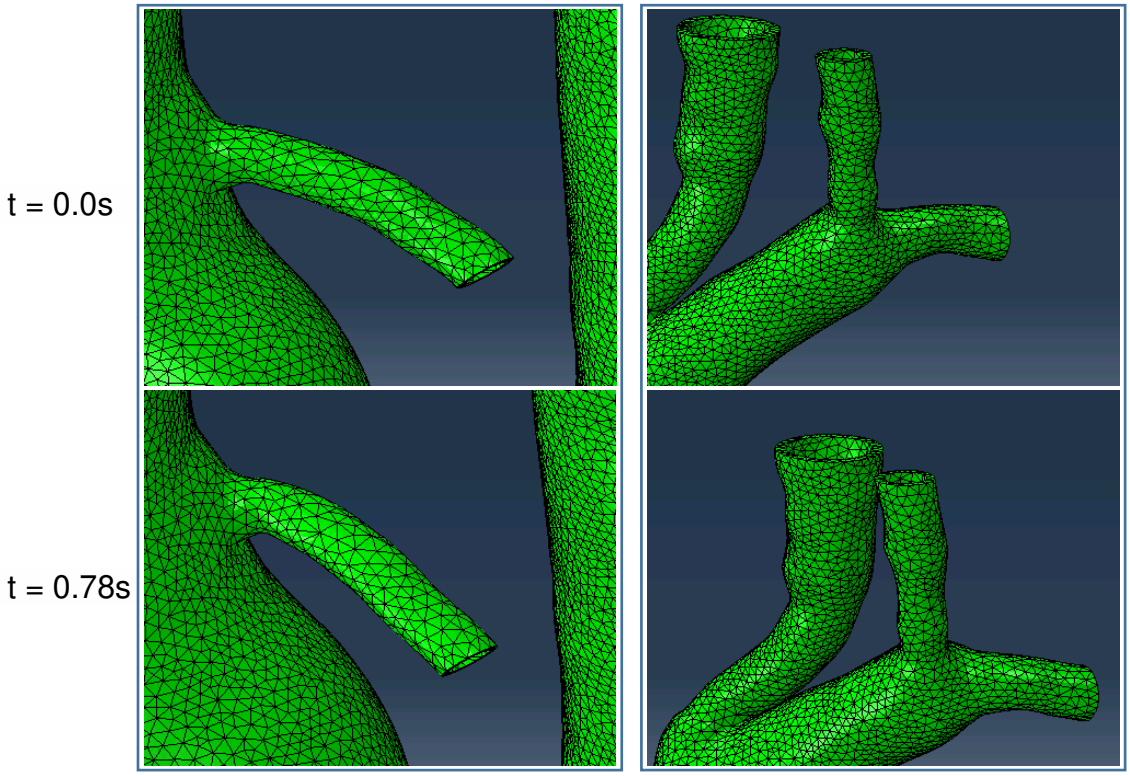

Figure 57 - Bulk motion of left coronary artery (right) and upper right vessels (left) from beginning to end of pre-stressing procedure.

Upon closer in section in figure 57, one can clearly observe contact between the outer surface of several vessels. In the case of the right coronary artery there is an evident stress build up in the contact region which dissipates azimuthally. The localized radial deformation is proof once again of the correct implementation of a hard contact model preventing any mesh failure.

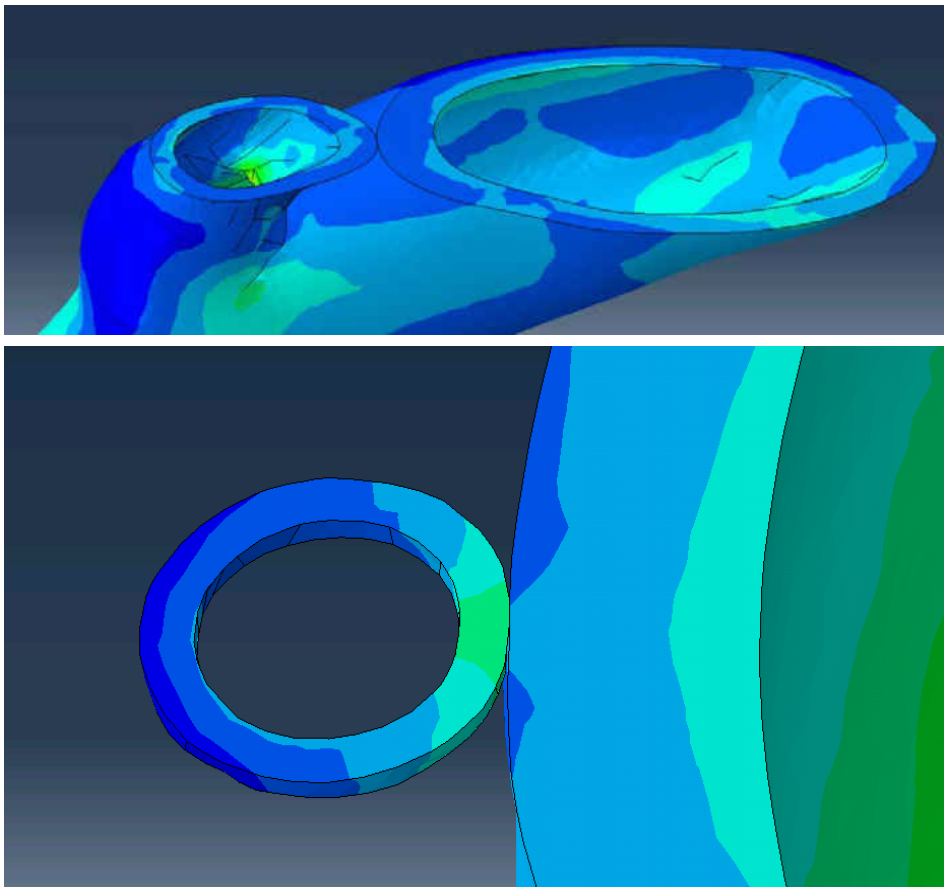

Figure 58 - Local conduit contact for right carotid artery (top) and right coronary artery (bottom).

4.2. Validation

The degree of complexity of this problem requires validation to ensure that every aspect the results obtained can be reliably be put forward as usable in further analysis. The criteria to determine the validity of this model relies on wall shear stress reduction induced by arterial wall compliance, residual stress analysis and expansion/contraction distance relative to in vivo and in vitro (similar simulations) data. In addition to the anisotropic material model implemented is test for a much simpler case of a periodically loaded cylinder mimicking the thoracic aorta. The successful verification of these samples should provide strong basis a validation claim.

4.2.1. Thoracic Aorta Test Model

As material model validation procedure to test the validity of the parameters, a simplified coupled model is tested. The vessel geometry is idealized as a straight tube to avoid any meshing issues especially in the arterial wall portion (Figure 59). The diameter of the cylinder is of 18mm while the length is 50mm. The arterial wall thickness is set to be 10% of the lumen diameter to keep consistent to the patient-specific configuration (for a wall thickness of 1.8mm).

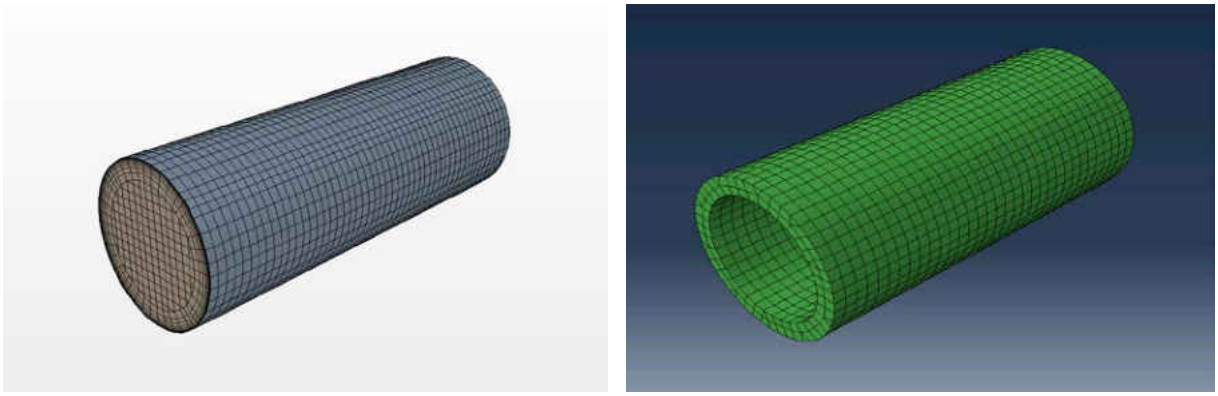

Figure 59 - Idealized thoracic aorta section with fluid domain (left) and solid domain (right).

The solver parameters for both the fluid domain and the solid are kept the same as for the patient-specific model. The fluid is assumed to be non-Newtonian, incompressible and under pulsatile flow conditions. The solid domain is solved by a dynamic implicit solver with HTT scheme and the material is assumed to have constant density. The fluid and solid are coupled implicitly at the time-step level (morphing at inner iterations allowed). The only difference is the boundaries are fully constrained (pinned), in order to clearly identify and quantify the interface motion. For this simple case, only the single layer anisotropic material model is tested, hence the material orientation and properties remain unchanged. There are two families of fibers, each fiber orientation

references to a single coordinate system along the centerline of the cylinder. The meshes are generated in the native software. As the domain allows it, a structured mesh is generated in both domains, in StarCCM+ hexahedral volume elements. To ensure proper solution propagation through the thickness of the solid domain, 2 layers of quadratic hexahedron elements and wedge elements are employed. The solid model was partitioned and the base size chosen to enhance interface vertex mapping. The fluid domain is discretized to 27764 cells while the solid contains 2904 cells.

Figures 60-62 and 66-69 display sequences of images throughout a single cycle for several different computed quantities in both the fluid and solid domains. Figures 61 and 62 display the pressure and velocity fields during a single heart cycle. The plotted scenes show a stable solution indicating that the fluid-solid coupling was successful. It is interesting to note that whereas for a rigid wall simulation the pressure-velocity field would present a seemingly symmetrical pattern, in the compliant wall case during diastole small low pressure regions form proximally and distally.

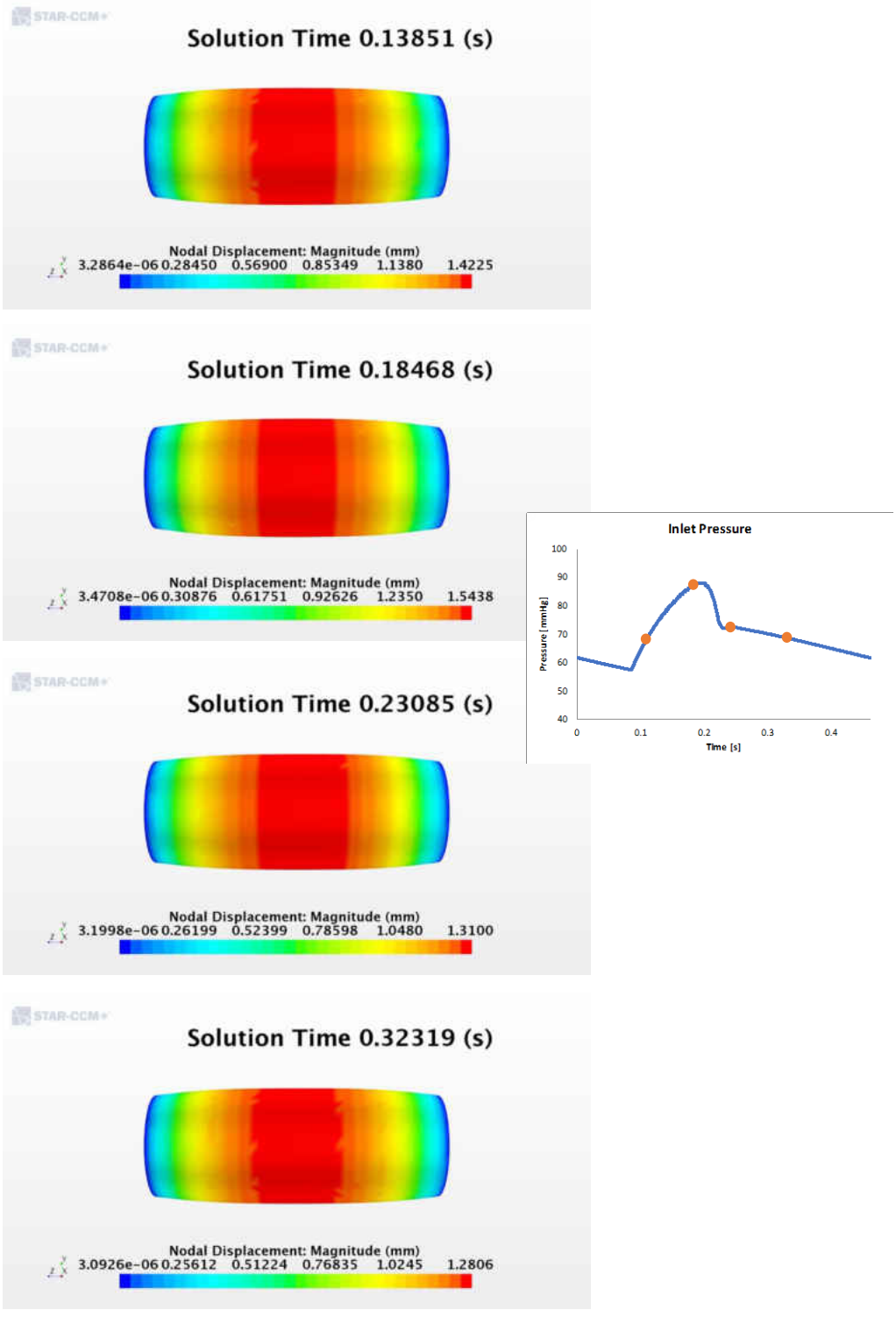

Figure 60 - Interface displacement through one heart cycle.

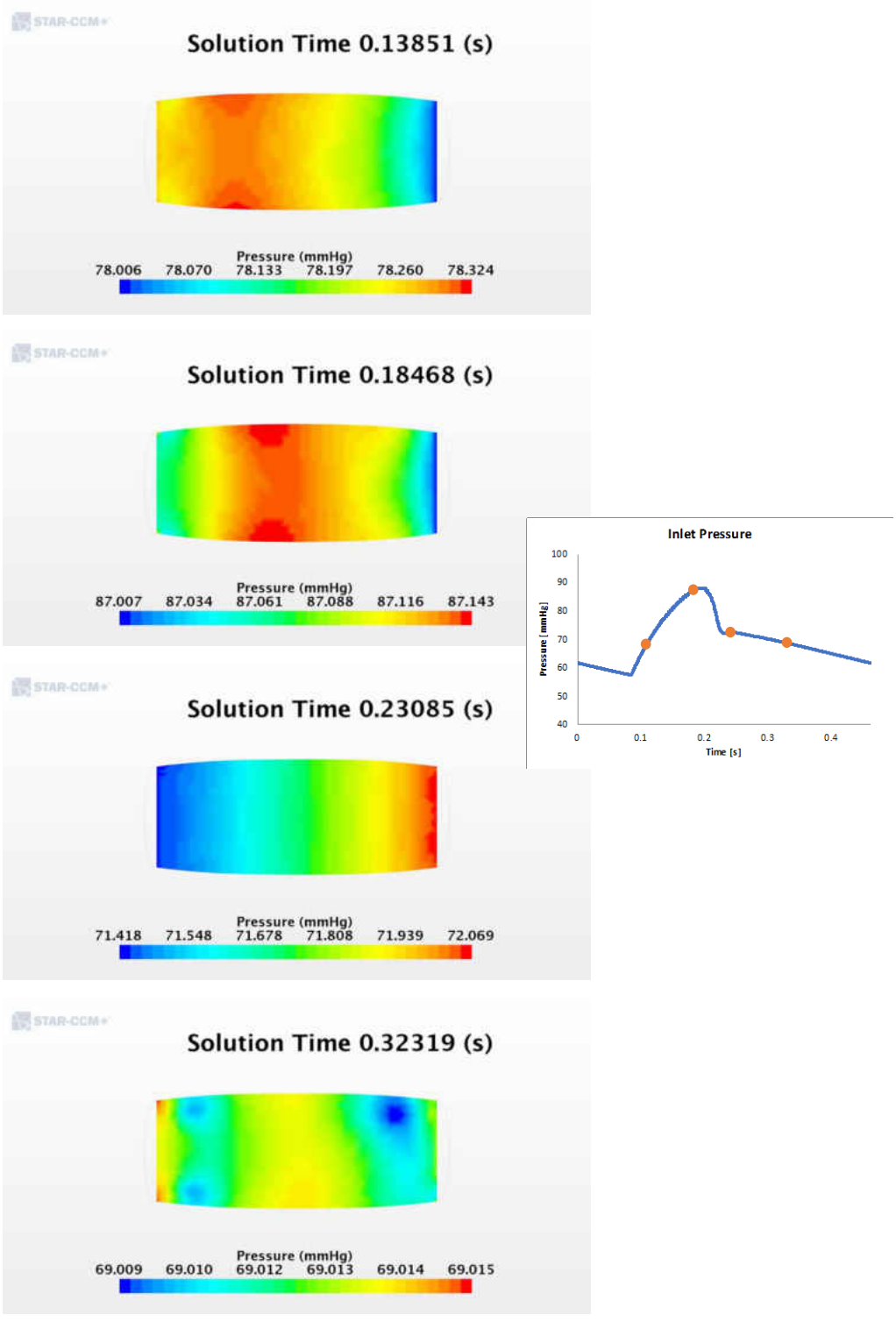

Figure 61 - Longitudinal cross-section displaying pressure distribution in the fluid domain.

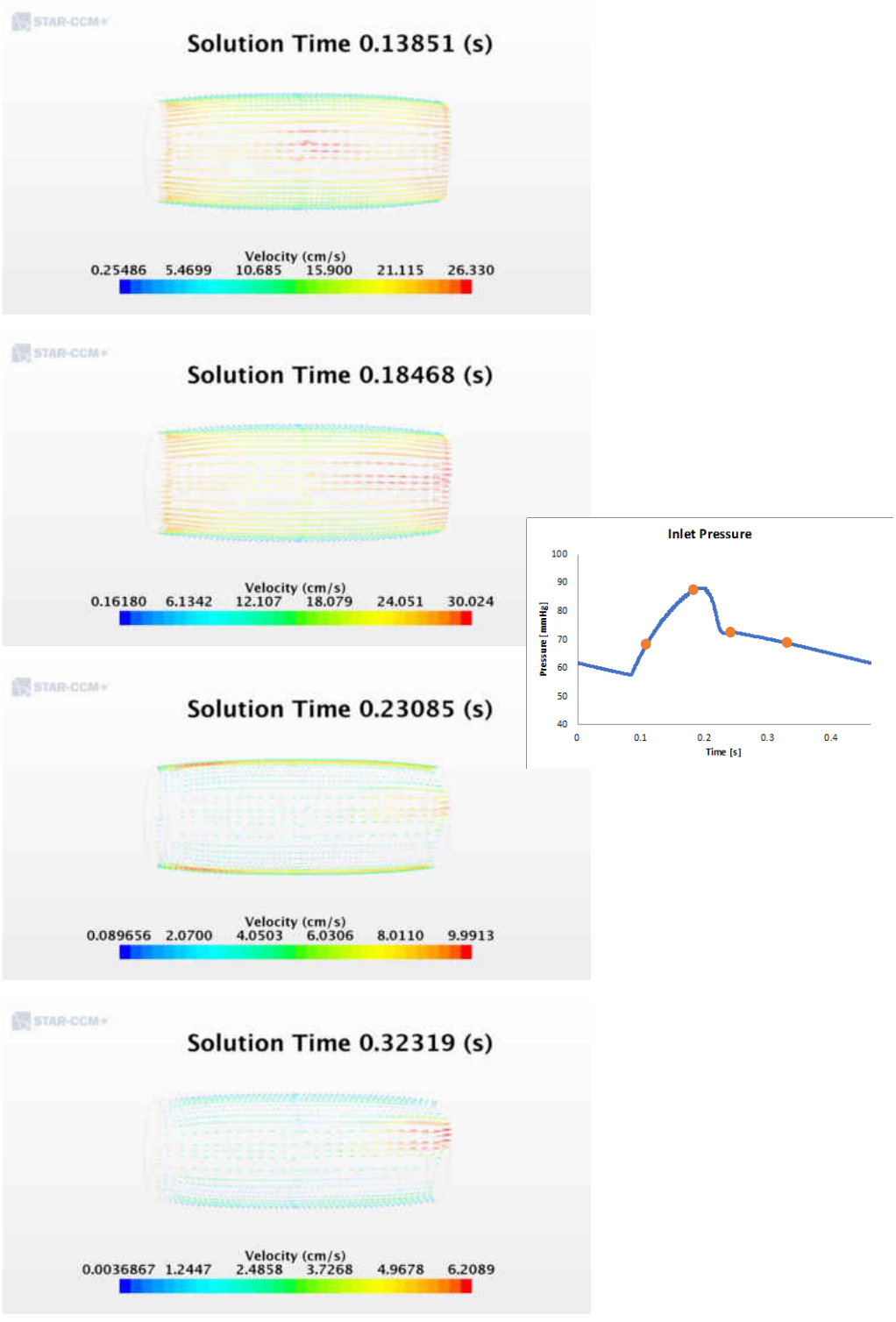

Figure 62 - Longitudinal cross-section displaying velocity field in the fluid domain.

The main feature of a FSI is the motion imparted to the coupled meshes. A simple way to verify whether the solid material model has been implemented correctly is to monitor the fluid-solid interface displacement and determine if the magnitudes appear realistic. It must be noted that similar models employed in other studies, typically have strong constraints to the solid model to prevent excessive motion and use a static solver. In this study solid domain accounts for the full equation of motion. This entails that bulk motion is present in the model as previously discussed. In this simple validation model, we limit the bulk motion of the solid by fully constraining the model at the boundaries.

Figure 60 displays the interface displacement in the fluid domain during early and peak systole (first two sequence images) and during early and late diastole. Based on the described solid domain constraints, it can be readily observed that the pinned boundary conditions imposed at the inlet and outlet have been successfully applied as no displacement is registered. At the center of the volume, the largest displacements are measured as expected. In this location, a cross-sectional plane is placed to record the interface nodal displacement display in figure 63. The displacement pattern can be seen to be symmetric about the center of the tube as expected. Due to the length of the tube, pressure wave propagation cannot be readily seen in Figure 60. However, by introducing intermediate monitor planes across the volume (Figure 64) the wave propagation time can be approximated and the wave velocity can be computed (Figure 65).

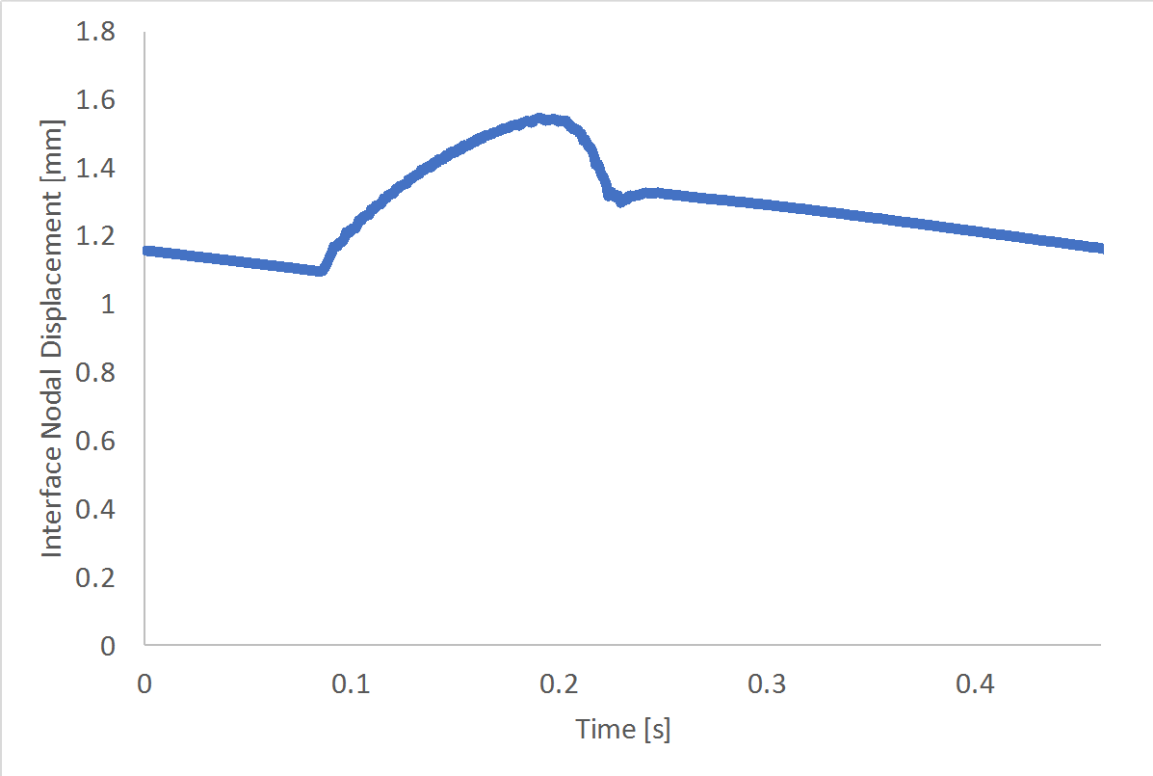

Figure 63 - Maximum interface nodal displacement.

With a maximum dilation measured at 1.55mm during peak systole, the stretch was computed to be at most of 8.60%. The typical range of stretch observed is between 5-20% depending on the state of the tissue, hence the value computed seems to be in good agreement with documented findings.

For the purpose of comparison, there are analytical solutions for the elastic deformation of a thin and thick walled cylinder under a uniform pressure load that mostly depend on the wall thickness to tube radius ratio. In this study, each solid domain considered is generated with a thickness equal to 10% of the local hydraulic diameter. Hence, we have the ratio is 0.2. Based on analysis for a thin-walled straight tube, given the assumption that $R \gg t$ (or $\frac{t}{R} \ll 0.1$) where R is the radius and t is the wall thickness,

the static force equilibrium can yield an expression (Equation 75) that approximates the radial displacement for a given pressure load P [36].

$$\Delta R = \frac{PR^2}{tE} \tag{75}$$

Where E represents the Young's modulus of the tube material. A similar expression can be obtained from the analysis of a thick-walled tube ($\frac{t}{R} \geq 0.1$). The displacement expression at the fluid-solid interface ($R = R_1$) is found to be

$$\Delta R = \frac{PR_1(1+\nu)}{E\left({R_2}^2-{R_1}^2\right)}\left[(1-2\nu){R_1}^2 + {R_2}^2\right] \tag{76}$$

Where R_1 is the inner radius, R_2 is the outer radius and ν is the Poisson's ratio [36]. Equations 75 and 76 can be used to provide an analytical estimation of the radial dilation for an isotropic material. The peak systolic pressure is about $90mmHg$, the Young's modulus is taken to be $0.4MPa$, and $\nu = 0.48$ [25]. The maximum dilation is found to be 1.35mm from Equation 75 and 1.34mm from Equation 76 for a 15% deviation from the FSI results. It must be noted the data relative to a linear elastic estimation of material properties based stress-strain curves obtained from in-vivo experiments are subject to approximation. For a linear elastic approximation, the hyperelastic curve is assumed to have two regimes separated by a transition point. The transition point is defined as the point separating the mechanical response were fibers are active. Hence, one regime prior to the transition point where the modules is rather small and a second regime where the modules grows in some cases 9-fold. The assumed Young's modulus is in essence an average of these two regimes for a linear elastic approximation.

A thin-walled cylinder analytical solution is available for the hyperelastic Holzapfel material model [37]. Based on the strain density energy function and its two invariants

defined in equations 77-79, a static force equilibrium yields a set of 2 non-linear equations (Equation 80 and 81) that can be solved by a numerical approach such as a Newton-Raphson method.

$$\psi(\lambda_\theta, \lambda_z) = c_{10}(\bar{\mathrm{I}}_1(\lambda_\theta, \lambda_z) - 3) + \frac{\mathrm{k}_1}{2\mathrm{k}_2}\{\exp[\mathrm{k}_2[k\bar{\mathrm{I}}_1(\lambda_\theta, \lambda_z) + (1-3k)\bar{\mathrm{I}}_4(\lambda_\theta, \lambda_z, \gamma) - 1]^2] - 1\} \tag{77}$$

$$\bar{\mathrm{I}}_1(\lambda_\theta, \lambda_z) = {\lambda_\theta}^2 + {\lambda_z}^2 + \frac{1}{(\lambda_\theta\lambda_z)^2} \tag{78}$$

$$\bar{\mathrm{I}}_4(\lambda_\theta, \lambda_z, \gamma) = {\lambda_\theta}^2\cos^2(\gamma) + {\lambda_z}^2\sin^2(\gamma) \tag{79}$$

$$\lambda_z \frac{\partial\psi(\lambda_\theta,\lambda_z)}{\partial\lambda_z} - \frac{\lambda_z\left(\lambda_\theta R - \frac{h}{2\lambda_\theta\lambda_z}\right)^2}{2hR} P = 0 \tag{80}$$

$$\lambda_\theta \frac{\partial\psi(\lambda_\theta,\lambda_z)}{\partial\lambda_\theta} - \left(\frac{{\lambda_\theta}^2\lambda_z R}{h} - \frac{1}{2}\right) P = 0 \tag{81}$$

Where $\lambda_\theta \; and \; \lambda_z$ are the circumferential and axial stretches. Once the stretches are computed for a given internal pressure and material parameters, the circumferential strain can be approximated as $\epsilon_\theta = \lambda_\theta - 1$. The radial displacement can be then computed as $\Delta\mathrm{R} = \epsilon_\theta R$ for a given radius R. The computed radial displacement for the tube is calculated to be $2.53mm$. The computed displacement seems much larger that the analytical result for a thin-walled tube, however as aforementioned the modulus of elasticity used was approximated and depending on the patient data can be an overestimation. By dropping the modulus to a value of $0.2MPa$ the resultant radial displacement is of $2.70mm$ for a 6.29% deviation. This observation gives the results an additional level of confidence.

To further corroborate the results of this test model the pressure wave propagation velocity across the tube can be measured and compared to an analytical solution under

the assumption of a thin-walled cylinder containing an incompressible and inviscid fluid that also neglects vessel wall inertia and that is given by the expression.

$$c_o = \sqrt{\frac{tE}{2\rho R}} \tag{82}$$

Equation 80 is known as the Moens-Korteweg relationship [36], where c_o is the propagation velocity and ρ is the fluid density taken to be $1060\frac{kg}{m^3}$. The rest of the parameters are kept the same as for the results obtained from Equations 75 and 76. This expression shows that the propagation velocity is directly proportional to the square root of the Young's modulus and directly proportional to the square root of the ratio of the wall thickness to the radius. Wave propagation increases for large stiffness and wall thickness while decreases for reduced wall thickness or large radius. In the FSI model, wall displacement data was collected at two monitor planes near the inlet and the outlet of the fluid domain at distance of 25mm from one another (Figure 64).

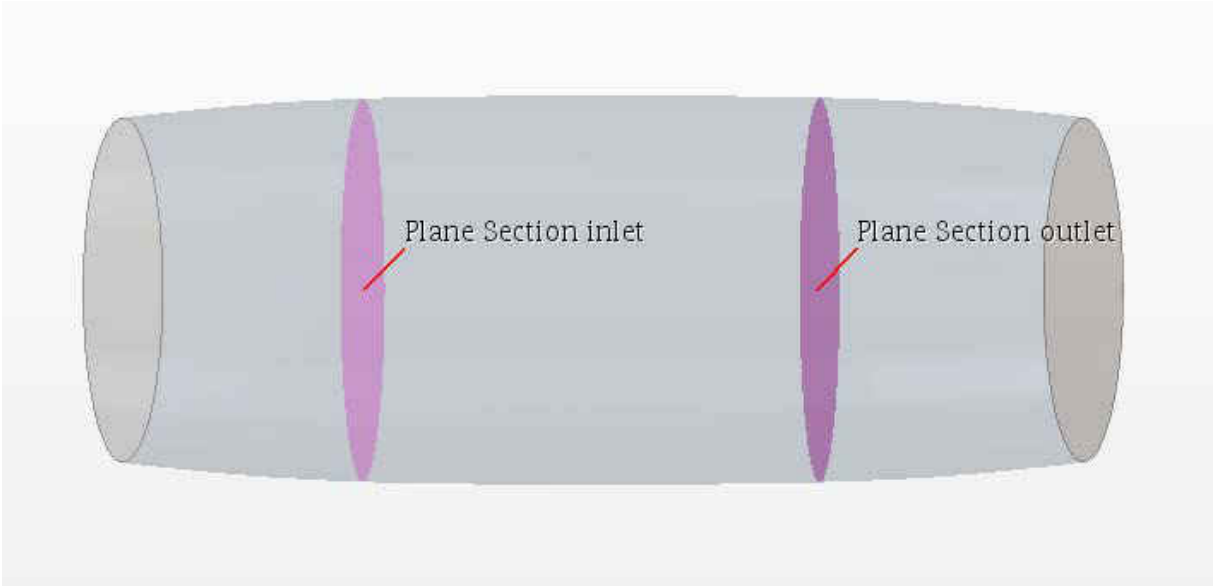

Figure 64 - Monitor planes near inlet and outlet.

The raw data collected at each monitor plane was imported into Matlab to apply smoothing due to localized outliers near the peak causing miscalculations of the time-delay (Figure 65). A 1D Gaussian-weighted moving average was used to smooth displacement data (Equations 83 and 84). In the following expressions P_M is the current data point and w_i are the Gaussian weights.

$$P_M = \frac{\sum_{i=0}^{2n} w_i P_{M-n+i}}{\sum_{i=0}^{2n} w_i} \tag{83}$$

$$w(x) = e^{-\frac{x^2}{2\sigma^2}} \tag{84}$$

The post-processed displacement data arrays were then analyzed to determine that maximum displacements.

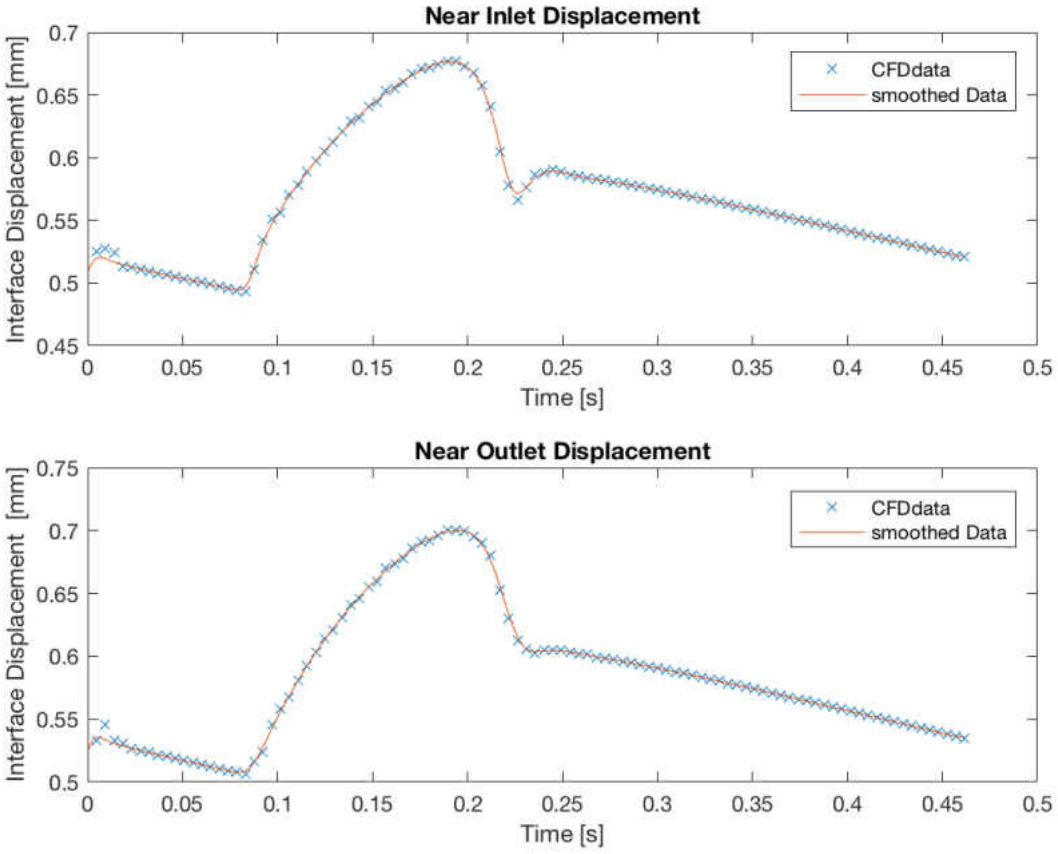

Figure 65 - Maximum displacements measured at each cross-section.

By monitoring the peak displacement values over a single heart cycle, it was possible to determine the time-delay of peak values between the two sections. Given the fixed distance between the planes wave propagation velocity can simply evaluated as $V_{prop} = \frac{\Delta x}{\Delta t}$, where Δx is the distance between the planes and Δt is the measured time-delay. The simulation yields a wave propagation velocity of $5.41 \frac{m}{s}$ while the Moens-Korteweg relationship analytical solution computes to $6.14 \frac{m}{s}$, for a 11.85% deviation. This result is consistent as the Moens-Korteweg velocity neglects inertial vessel wall damping and neglects viscous flow damping and is thus expected to yield a faster wave speed

than that FSI solution. Hence the results obtained fare rather well with the analytical solution and follow the expected mechanical behavior.

Figures 66 and 67 plot the arterial wall displacement through single cycle for cross-section in the circular and longitudinal directions. Once again in agreement with the fluid domain interface displacement there is not boundary displacement while the maximum displacement is registered at the center of the model. The additional insight these two figures offer is the displacement field across the thickness solid geometry. It can be observed that the displacement in the radial direction is not necessarily uniform across the thickness suggesting a mild amount of bulk compression. The inner surface experiences a larger displacement than the outer surface.

Figures 68 and 69 display the magnitude of the stress field in unit of MPa in the circular and longitudinal cross-sections. Due to the enforced boundary constraint at the inlet and outlet as shown in Figure 69 these two regions become stress concentrators. As expected the region of largest stress is at the fluid-solid interface in the center of the domain. Figure 66 provides additional insight on the stress magnitude distribution in the radial direction.

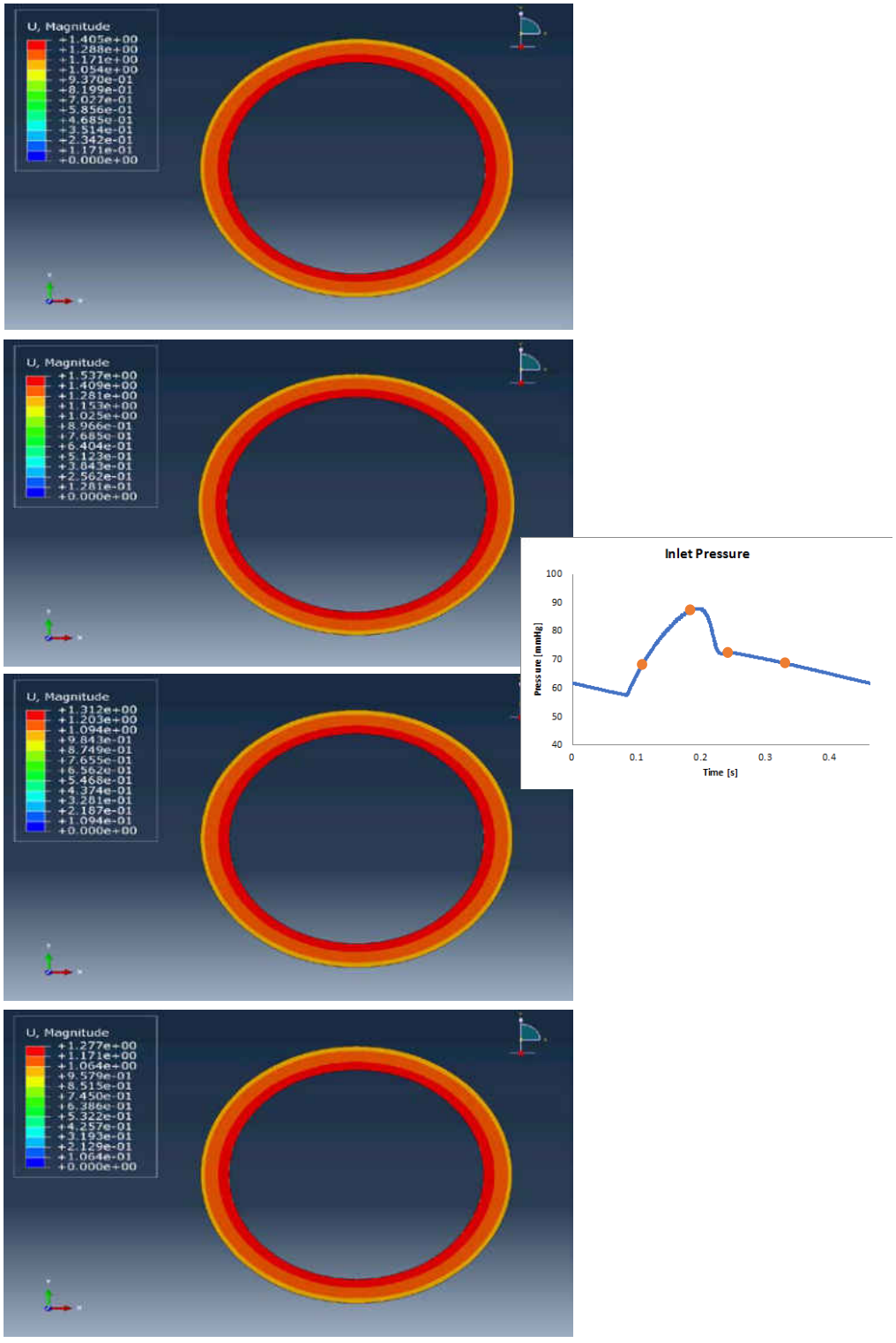

Figure 66 - Axial cross-section displaying displacement field [mm] in the solid domain [mm].

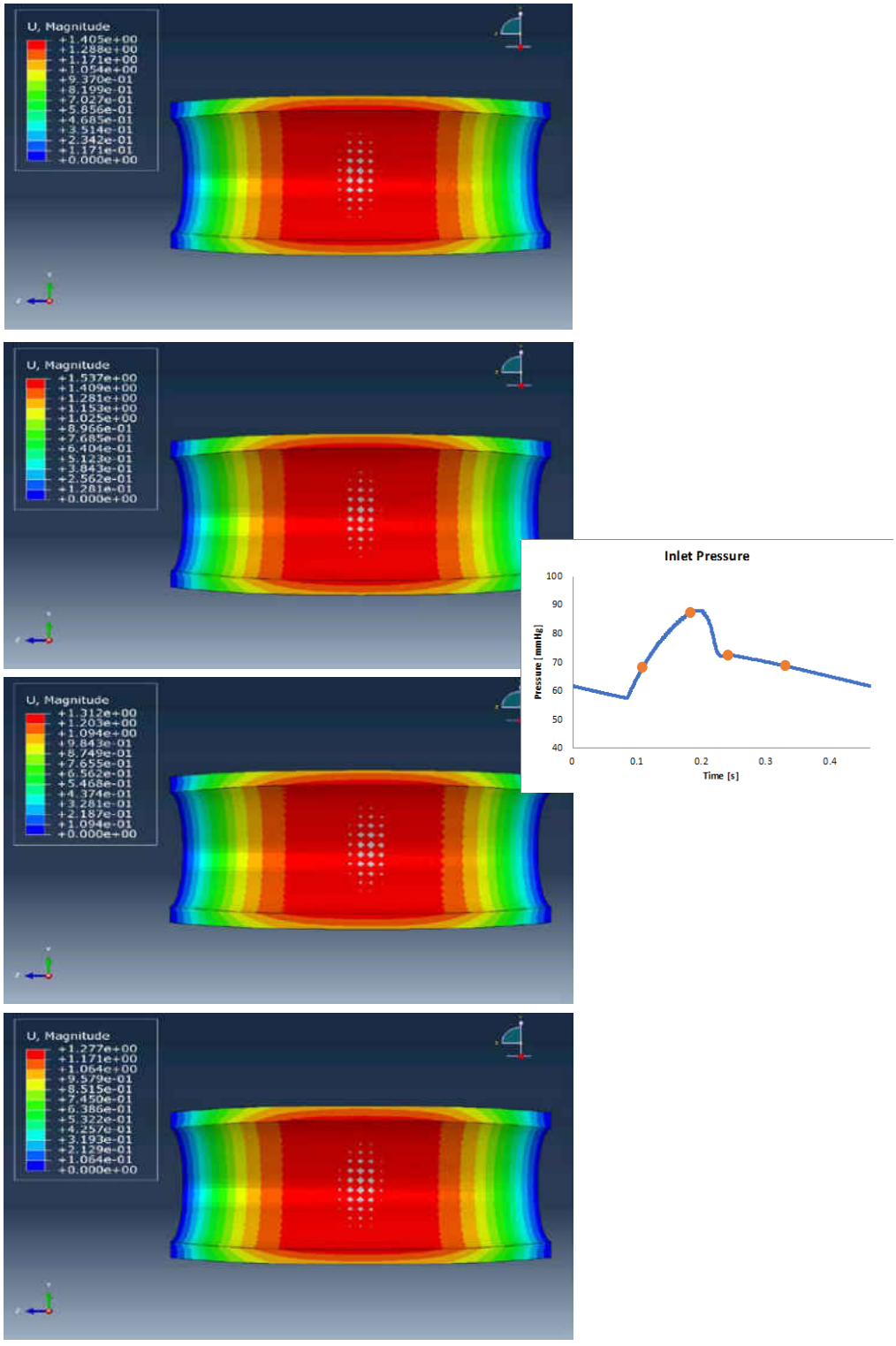

Figure 67 - Longitudinal cross-section displaying displacement field [mm] in the solid domain.

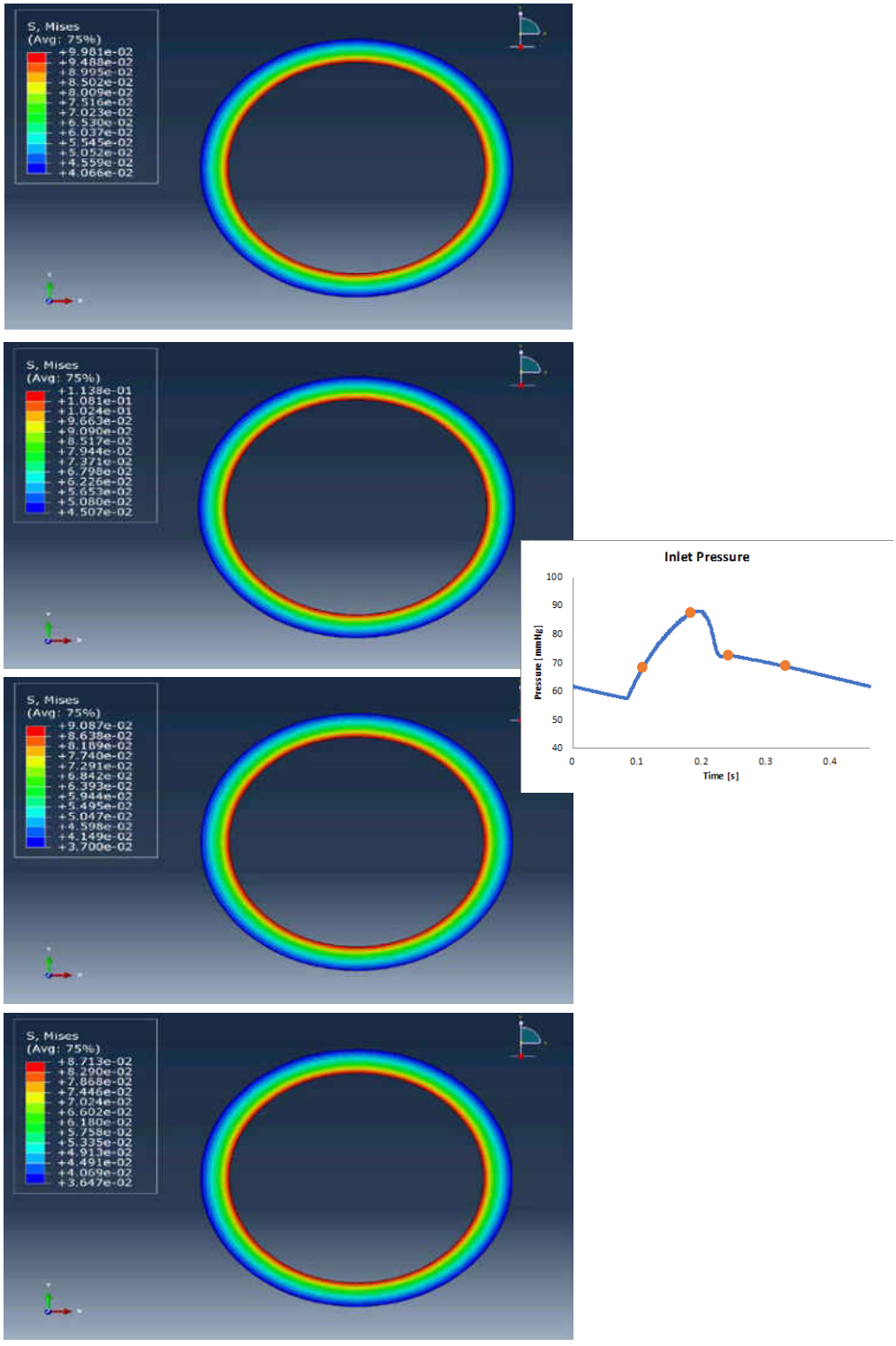

Figure 68 - Axial cross-section displaying stress distribution [MPa] in the solid domain.

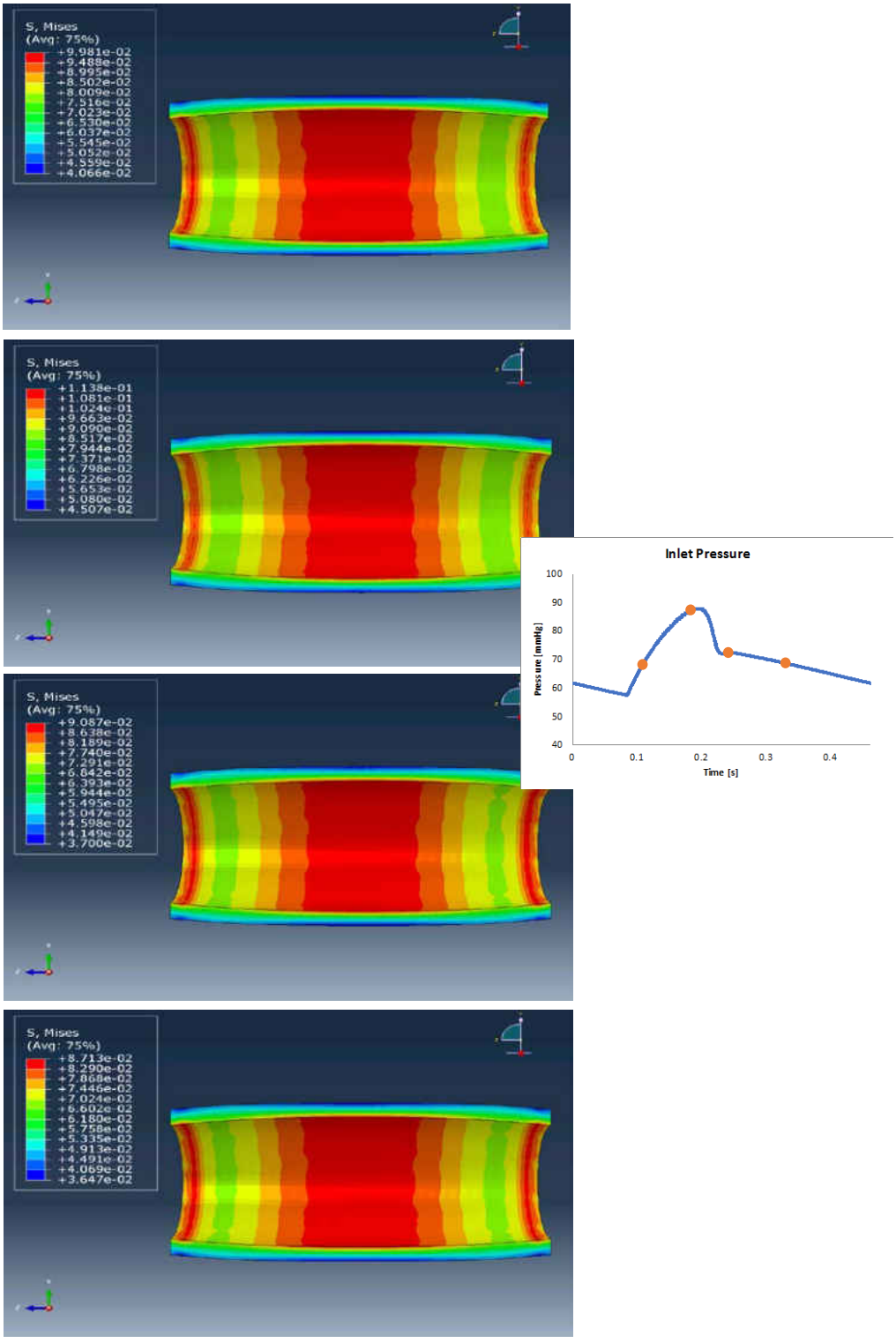

Figure 69 - Longitudinal cross-section displaying stress distribution [MPa] in the solid domain.

Several studies offer various ways of generating a pre-stressed aortic wall configuration preceding the fluid-structure coupling. In principle, the pre-stressing algorithm entails an unloaded configuration and target deformed configuration with residual stresses [17, 25, 38, 39]. The target configuration represents the anatomical geometry at a specific point in the heart cycle (typically systole) obtained by means of medical imaging. The intention is to iteratively apply pressure loads on the fluid-solid interface of the arterial wall to induce the formation a stress field and deformation. The deformation is then compared to the target configuration. At each step the equilibrium is determined by the interface pressure load and the stress field generated.

The residual stress field can also be traced for each component $\sigma_{rr}, \sigma_{\theta\theta}$ and σ_{zz}. Figure 70 provides a map of the residual stress distribution at the center of the solid domain. Here peaks are measured to be $\sigma_{rr} = 0.9898\, kPa$, $\sigma_{\theta\theta} = 43.93\, kPa$ and $\sigma_{zz} = 28.06\, kPa$. These values are in fair agreement with residual stress fields for similar models found in literature [38].

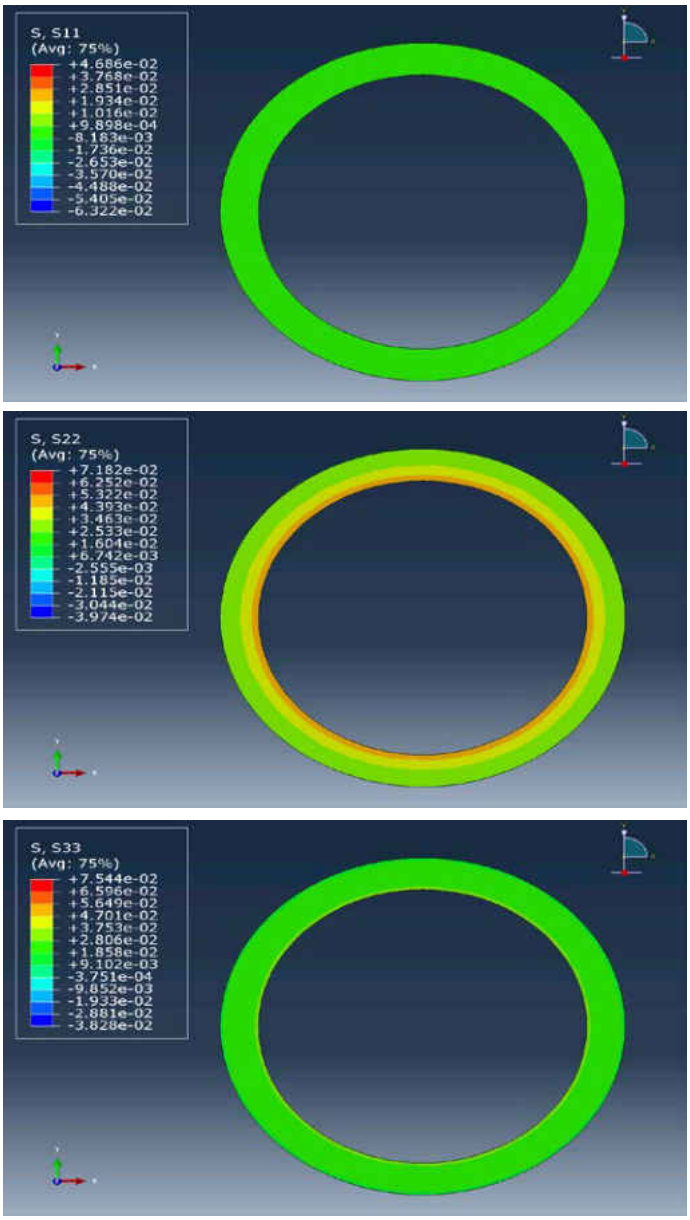

Figure 70 - Residual stresses in radial, azimuthal and axial directions.

Failure to correctly assign material orientation can results in the failure to generate a solution or results can be generated, however such results can be unreliable. The fiber orientations are defined by two 2D unit vectors which ideally lie in the θ-z plane. If the reference coordinate system is chosen to be cylindrical, as shown in the current results, the solution is accurate. If the CS implemented is anything other than cylindrical, the fiber

orientation risks to be non-uniform in the 2D plane where the unit vectors are defined. Figure 71 displays the displacement field for a material model whose orientation is defined with a Cartesian CS, the dilation is clearly non-uniform despite there being a uniform azimuthal load. In this case, the fiber orientation results correct at the top and the bottom of the geometry, however at the sides both family fiber are oriented in the radial direction. By comparing the peak displacement with the ideal case a nearly 5-fold increase in displacement is measured. Based on the analytical solution, a maximum displacement of about 1.35mm is be expected, however a peak displacements of more than 7mm are computed. Even compared to the model with fibers oriented correctly the displacement is found to be 1.55mm.

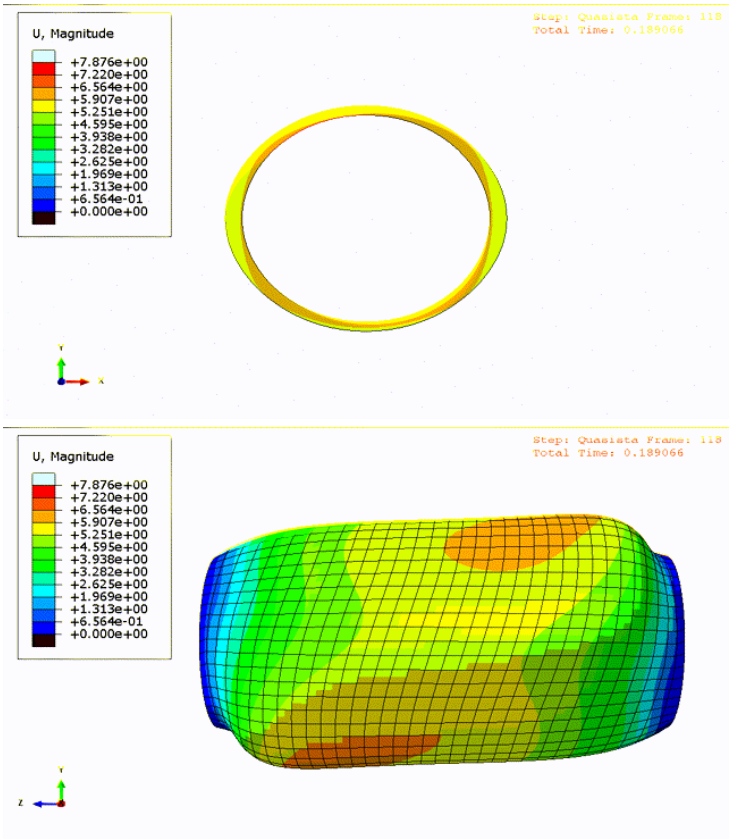

Figure 71 - Peak Systolic wall displacement for failed hyperelastic material model.

4.3. Full Aortic Model Results

The full-scale FSI simulation was ran on a total of 56 CPUs. 42 CPUs were dedicated to StarCCM+, hence 3 CPUs per machine were allocated to the fluid domain. 14 CPUs were assigned to Abaqus according to the round-robin scheme, with 1 CPU per machine allocated to solid domain. This CPU subdivision maximizes the computing power and expedites the simulation at the best of its abilities.

The material model that was implemented presents a combination of the hyperelastic and liner elastic models. The linear elastic model is enable at locations where defining a material orientation becomes excessively difficult. Such locations are for instance bifurcations and region where the conduit has a large curvature.

Given the mobility of the fluid domain, data relative to the flow field are represented through streamlines for both velocity and pressure fields. This viewing option allows to show the flow origin which in the following image sequences can clearly be identified as the LVAD outflow cannula and the aortic root. Figures 72-73 offer insight on the flow patterns during a single heart cycle (0.75 s), with a pressure wall plot to show sampling instant. In the second and third images in the sequences (Figures 72-73) it can be clearly seen that portions of the flow generate from the native ventricle during systole. In diastole, given a continuous flow pump has been implanted, flow only generates from the cannula. The image sequences display similar pathological flow fields as in the rigid wall model (Figure 49-51) such as flow stagnation and recirculating flow in the aortic root in diastole, cannula jet impingement on the distal aortic wall during diastole and cannula jet oscillation due to the pulsatile nature of the flow generating from the aortic root. In figure 69 it can be observed that the velocity field can range from $0\ \frac{cm}{s}$ (stagnant flow) to peaks of about

$130\ \frac{cm}{s}$ which can be considered physiologically accurate. In addition, similarly to the rigid wall case, the cannula retains a non-negligible degree of pulsatility. Figure 73 offers a closer look to the pressure distribution in fluid domain. In conjunction with figure 72, it helps identify the source of pressure head which as expected is the outflow cannula. It must be emphasized that the cannula has been omitted form the solid model geometry as it is assumed to be completely rigid hence no compliance is expected in at the anastomosis boundary and reduced dilation is expected in the nearby region.

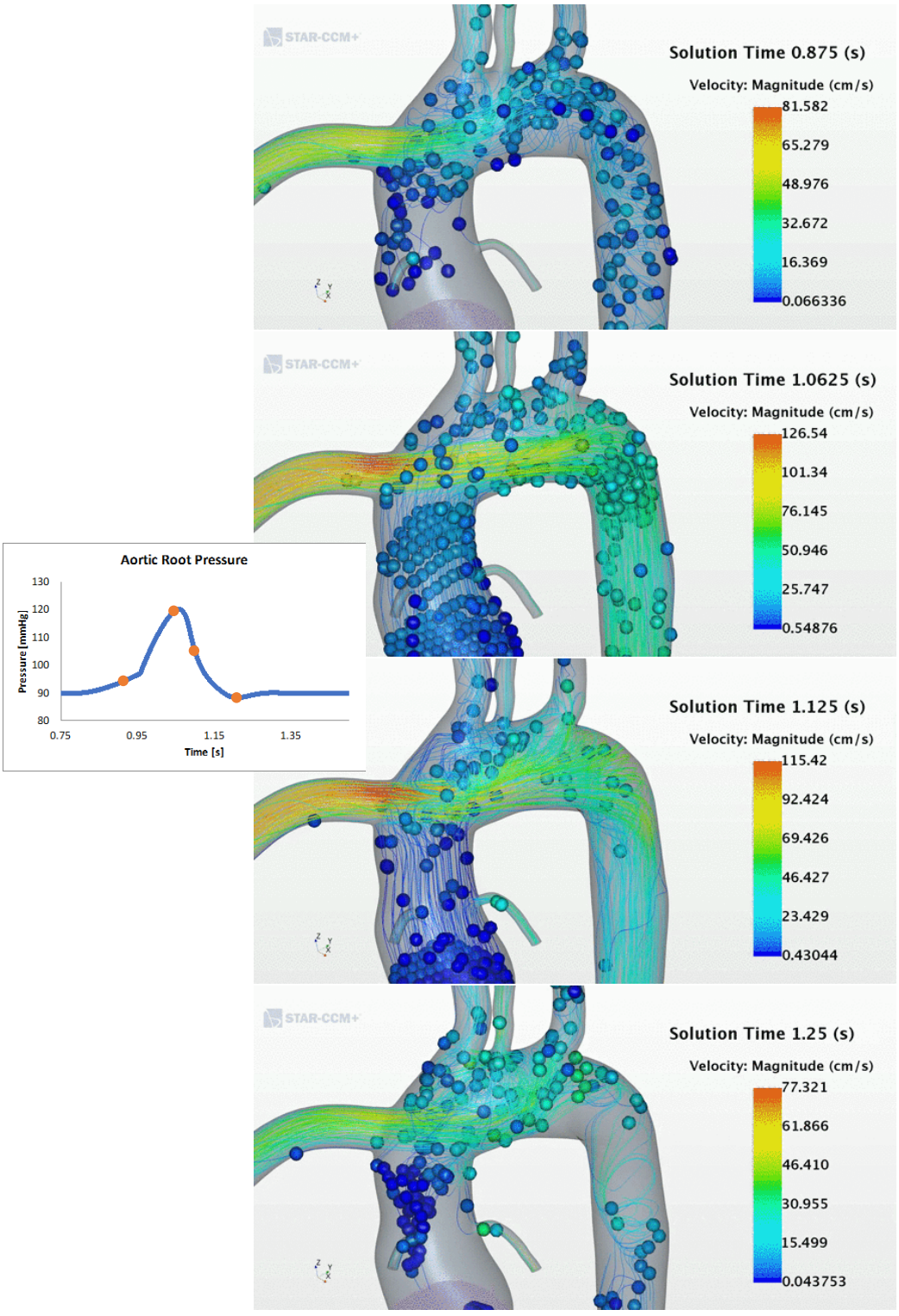

Figure 72 - Velocity Streamlines for compliant model throughout 1 heart cycle.

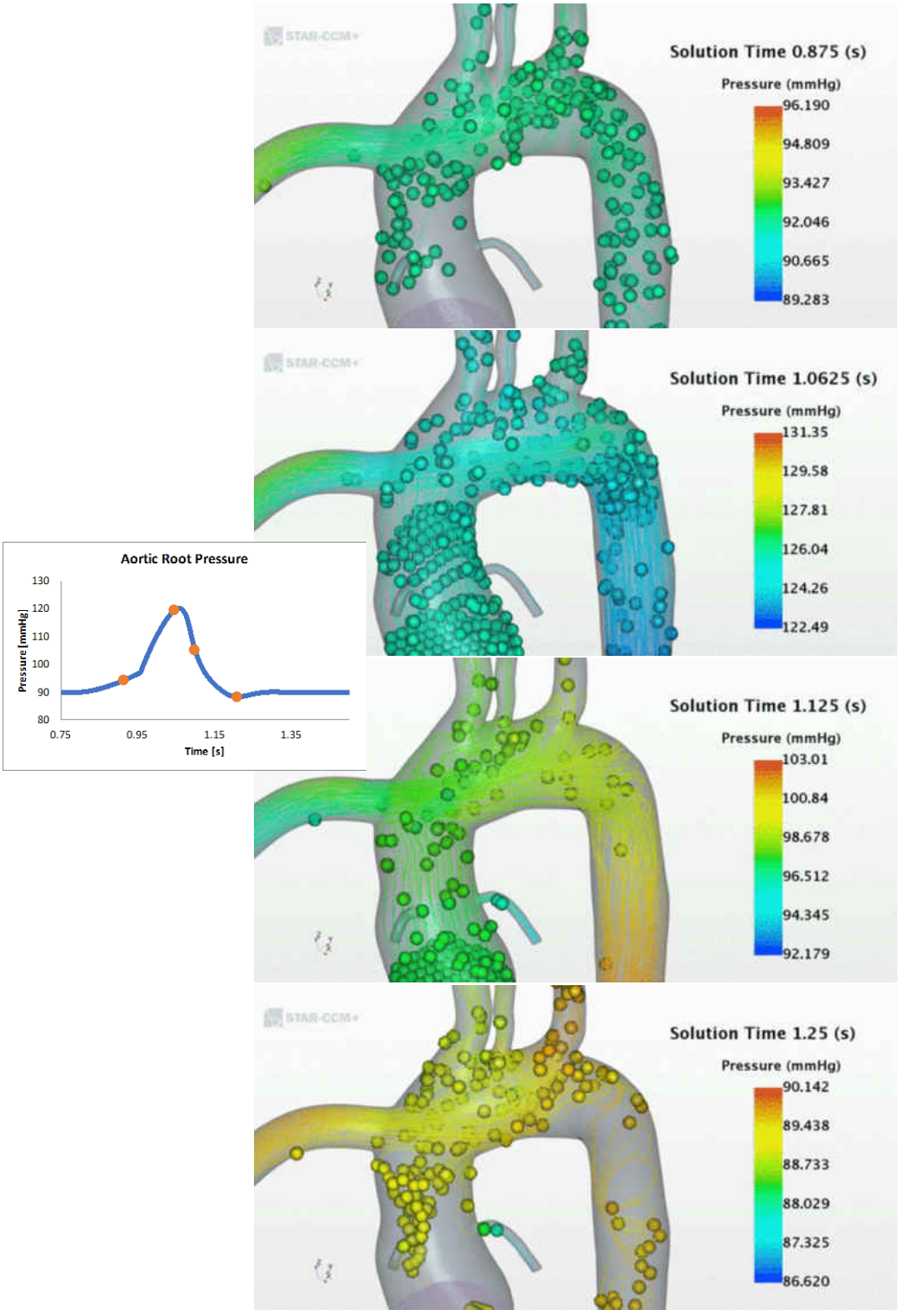

Figure 73 - Pressure Streamlines for compliant model throughout 1 heart cycle.

Similarly to the simplified straight tube model, displacement is sampled a different locations along the aortic arch. Figure 74 reports the displacement during a single hear cycle. The largest displacement occurring in systole is measured to be 3.55mm located in the descending aorta. The stretch is calculated to be of about 14.20% which, as for the simplified model, falls within the physiological range of 5-20%. As previously mentioned, the LVAD boundary was fully constrained, hence displacement in the nearby region would be reduced. In Figure 74, the orange and dark blue curves represents the displacement monitor for planes closely located to the LVAD boundary. As expected the maximum displacement registered in these two regions is markedly lower compared to the rest.

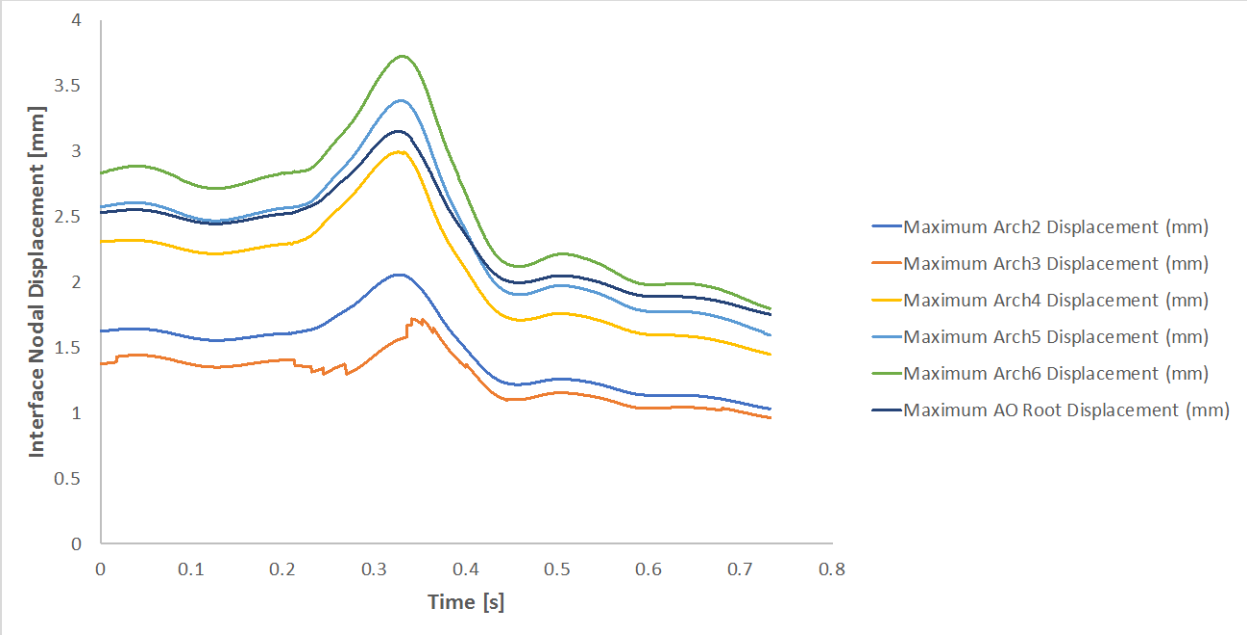

Figure 74 - Displacement at 6 cross-sections along the aortic arch.

It is possible to compare these results to the analytical solution previously used for the verification model. In the patient-specific model, we isolated wall displacement for a relatively straight section, namely the descending aorta. As previously noted from figure 74, the largest displacement in this portion was measured at 3.55mm. Based on the

analytical expression for a thin-walled cylinder composed of a hyperelastic material modeled according to the Holzapfel implementation (Equations 77-81) the expected wall displacement during peak systole can be of 3.13mm. With a deviation of about 13.42% from the computational results it can be inferred that the model is behaving appropriately.

To run the full FSI simulation, the rigid wall coupled problem with converged BCs must run to generate the flow field. Due to the nature of this initial simulation very large and unrealistic loads are generated at the wall. As a result, compliance may cause as much as 50% in shear-stress reduction in WSS for instance [17]. This WSS reduction can be quantified by measuring the average WSS and by monitoring WSS peaks across the domain throughout a single heart cycle. Figure 75 provides some insight in the WSS distribution tracked for a single heart cycle in a model with rigid walls. The sequence displays both the surface distribution along with the surface averaged WSS value. Upon observation, clear WSS peaks can be identified:

- Wall LVAD-jet impingement which can be tracked throughout the cycle;
- Coronary WSS caused by large velocity gradients in the region;
- RCA, LSA caused by a converging-diverging nozzle effect which accelerates the flow;
- Bifurcations.

The rigid wall model registers peaks ranging between 240-300 $\frac{dyne}{cm^2}$ which are unrealistic loads mainly due to stress concentration at stagnation points. From a physiological standpoint, the realistic range of WSS experience at the interface should range between 10-40$\frac{dyne}{cm^2}$. It must be emphasized the severely large WSS measured a

very limited to very small areas hence a surface averaged value of WSS may be more appropriate.

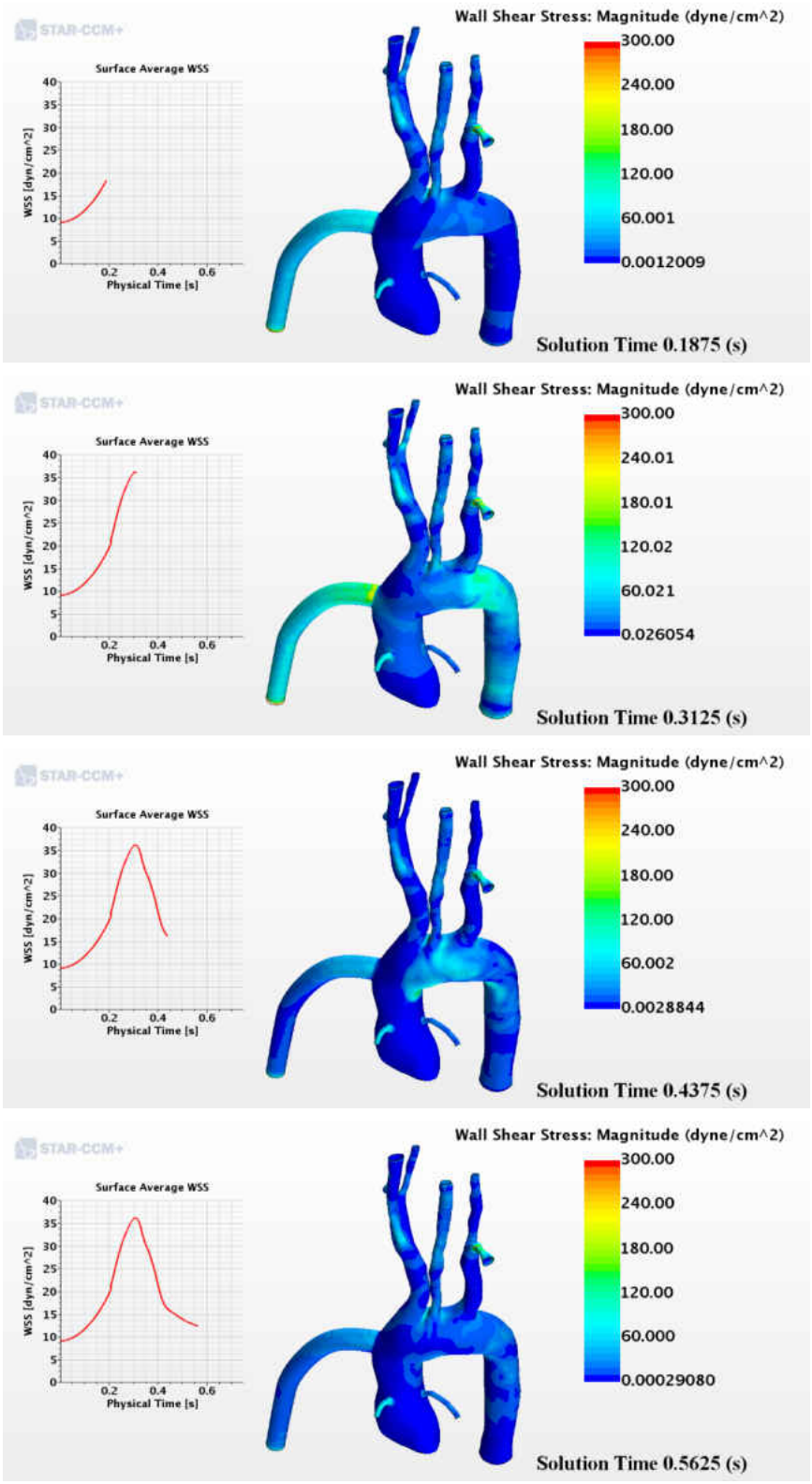

Figure 75 - WSS distribution for rigid wall model.

If the surface average WSS at the interface is measured, more realistic loads are found. In figure 76 for a single heart cycle of the rigid wall model (blue curve) the average WSS can vary between 10-37 $\frac{dyne}{cm^2}$. These values are physiologically realistic. When compared to the compliant model case (orange curve), a decrease in surface averaged WSS can be observed throughout the cycle (range is 10-34 $\frac{dyne}{cm^2}$). The largest drop computed at 7.22% occurs at peak systole. In addition, the peak WSS value for the compliant model have also been computed to display a 50.54% drop from the rigid wall case in agreement with what is stated in literature.

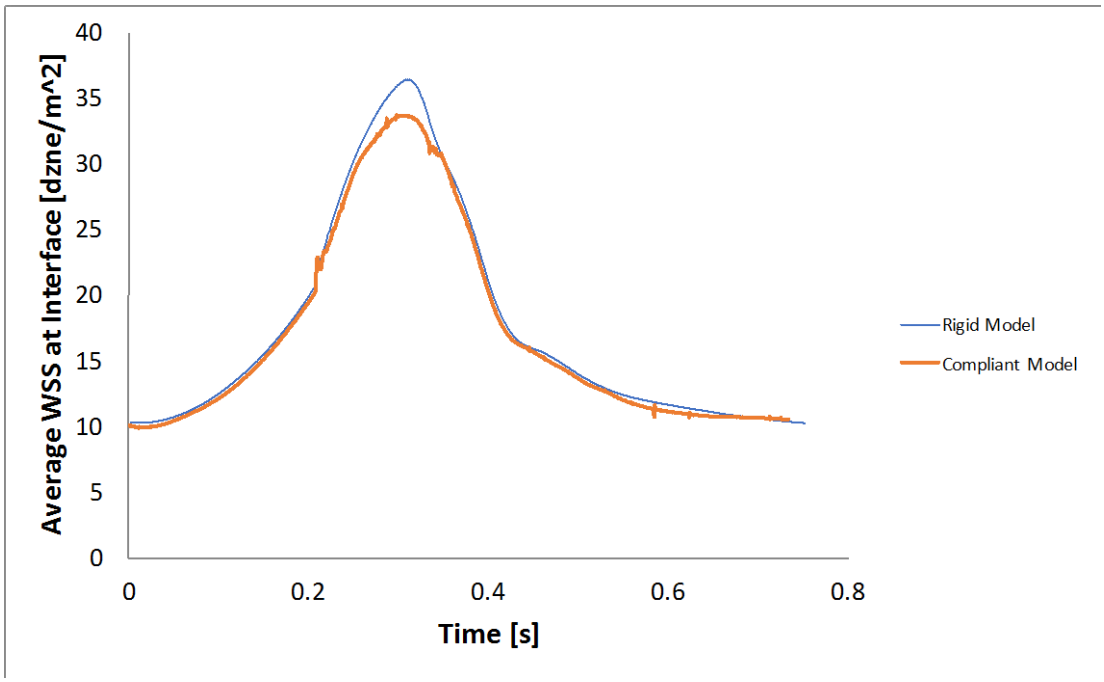

Figure 76 - Average WSS at fluid-solid interface.

5 CHAPTER: CONCLUSIONS

5.1. Conclusions

The FSI paradigm proposed in this study provides for a rather complete and dynamic model accounting for pulsatile flow conditions, patient specific non-Newtonian blood model, and arterial wall compliance.

With this model, the user can freely swap the patient specific geometry in both the fluid and solid domains. In the solid domain, the arterial wall geometry can be generated with a variable thickness to reflect 10% of the local hydraulic diameter. Various blood disorders can potentially be taken into account based on clinical data can be easy curve fitted. The model can also reduce complexity with a Newtonian fluid assumption. Arterial wall properties can be modified to simulate healthy or malfunctioning tissue. By incrementing or decrementing fiber orientation dispersion in conjunction with manipulation the isotropic matrix properties it is possible to induce material failure that could amount to an aneurism. The LPM that provides the BC imposed to the CFD can also be manipulated to alter physiological flow conditions spanning from a heathy cardiac output to a severely failed heart. The model provides are rather solid tool to make stroke-related inference on a patient specific basis. In addition in this investigation we altered the core allocation scheme to accommodate for the inability to generate multiple threads on a single machine for the FE software and successfully maximized the computational speed given the resources.

The validation model of a simple straight tube representing the thoracic aorta generated results in agreement with documented quantities. With a maximum radial

displacement of 1.55mm the computed stretch is found to lie within the physiological range of 5-20%. The residual stress field in diastole for the principal directions for a single layer hyperelastic material is found to be in fair agreement with similar results for a 3-layer hyperelastic material. In addition, the comparison to analytical solutions for a thin-walled and thick walled elastic tube yield a 15% deviation, further validating the model.

The FSI managed to retain stability despite the large variability in length scales and large deformation the 3D domain underwent. The incremental loading across a time step, fluid mesh morphing at inner iterations, structural damping and hard contact modeling successfully maintained stability and improved the model's reliability.

5.2. Limitations

This project may find limitations in the models employed to regulate particle interactions in the fluid domain. These relationships are based on restitution coefficients which even given the range may not entirely capture the full spectrum of interactions. As such, StarCCM+ has a model capable of tracking particle movements and interactions in a more detailed fashion, the Dynamic Fluid-Body Interaction model (DFBI model). This option however turns out to be rather computationally taxing.

This multi-scale study also does not include any modelling of thrombus generation; it implies thrombus are simply dislodged in either of the three-region at a specific size which does not change. That said, given the introduction of particle-to-particle interactions this model does in fact contemplate the possibility of cluster generation and growth thought the domain as well as particle deposition.

An additional limitation is found in the anisotropic material model. This model presents the contribution of an isotropic and an anisotropic portion to the strain energy

function. The fiber contribution occurs mostly during tensile deformation and is strongly depended on fiber orientation [40, 41]. For a simple idealized geometry fiber orientation can be easily implemented and complication may when bifurcations are investigated. However, for a patient specific model with a large number of branching vessels and a large hydraulic dimeter variability partitioning the model to generate local orientations can become tedious and may to certain degree lead localized computational errors.

5.3. Future Work

Due to the computational expenses involved, embolization probability data for the current configuration has been partially gathered. However, the population size has been deemed too small to warrant any further statistical analysis. More runs are necessary to ensure statistical significance. In addition, due to the bulk motion of the fluid region, particle injection grids in the artic root accounting for particles emanating from the ventricle and dislodging from the aortic root wall resulted incomplete. Once the injection grids are generated, these are fixed in space. Hence in case of large deformation, not only portions of the injection lumen will no longer function as such, there may be the potential for no particles to be injected at all. A similar issue has been observed in calculating the local Stokes number. As this quantity requires the evaluation of the local cross-sectional area and perimeter, failure to retain a consistent cross-sectional plane results in poor Stokes number measurements. Hence the original strategy to monitor Stokes number at a local level must account for potential bulk motion.

The same procedure described should be repeated for various suture configurations (Figure 77) for a more comprehensive study to determine outflow graft orientation to reduce stroke incidence.

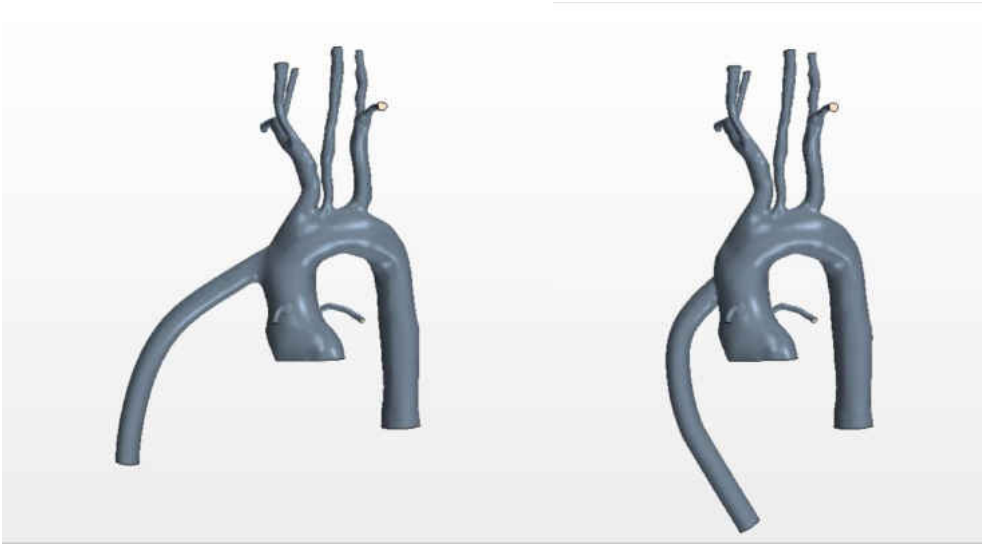

Figure 77 - Other viable geometries.

Also, it could be possible to reduce the sample size of particle released in the domain to use more accurate particle transport models such as the DFBI model. This would allow a more in depth study aimed at understanding and quantifying the importance of particle interaction in stroke incidence. An additional update to the particle model may include considering different particle geometries (not only spherical) which from a qualitative point of view would generate rather different results considering drag and lift effects.

To avoid any issues regarding fiber orientation, the material model could potentially be interfaced with scheme that tracks the conduit centerline in real time. The centerline can be used to trace local coordinate with the axial-axis tangent to the centerline for each element in the vicinity minimizing the distance from a node to the centerline (Figure 78). This approach would entire avoid any pre-processing requiring geometry partitioning, generating/offsetting local coordinate systems and defining multiple material sections.

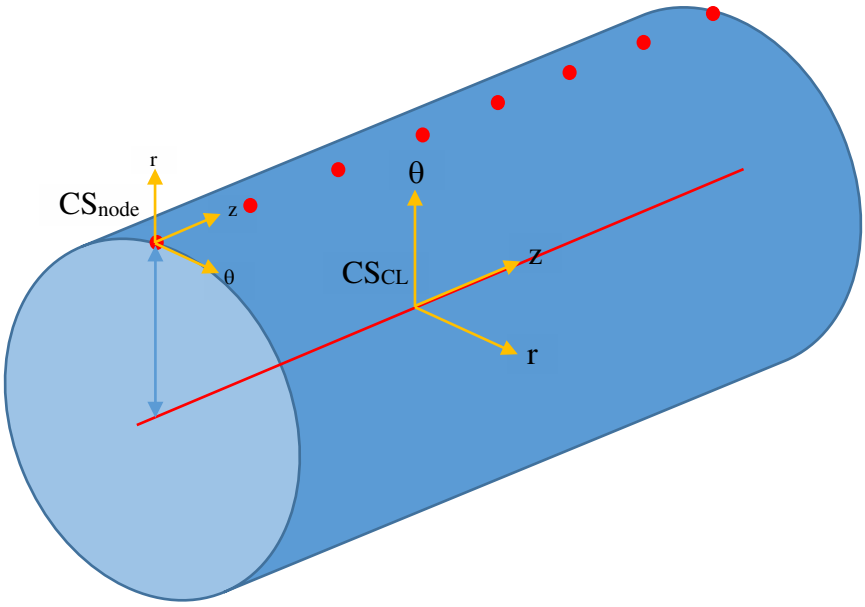

Figure 78 - Centerline based local coordinate system generation scheme.

5.4. List of Current Publications

Abstracts

Prather, R., Divo, E., Kassab, AJ, Argueta, I.R., and DeCampli, W.M, “A multi-scale CFD analysis of Patient Specific Geometrics for different LVAD implantation configurations under Pulsatile Flow conditions: An investigation into Thrombo-Embolism formation to reduce stroke risk” - Coupled Problem 2015- VI International Conference on Computational Methods for Coupled Problems in Science and Engineering , Papadrakakis, M., Onates, E., and Scheffler, B., (eds), San Servolo, Venice, Italy – 18 - 20 May, 2015 (Abstract and Oral Presentation).

Prather, R., Seligson, J., Divo, E., Kassab, AJ, Argueta, I.R., and DeCampli, W. M. “Muti-Scale CFD analysis of Patient Specific Hybrid Norwood Geometries: A Study to determine optimal shunt size to reduce stroke incidence”, EF2016 – the 5th International Conference in Engineering Frontiers in Pediatric and Congenital Heart Disease, June 9-10, 2016. (Abstracts and Poster Presentations).

Prather, R., Koochakzadeh, S., Divo, E., Kassab, AJ, Argueta, I.R., and DeCampli, W.M. “Assessment of Effects of VADs on Cerebral Embolization Rates for Clots Generating in the Ventricle, the Aortic Root, and VAD”, EF2016 – the 5th International Conference in Engineering Frontiers in Pediatric and Congenital Heart Disease, June 9-10, 2016 (Abstracts and Poster Presentations).

Mazzeo, M., Norfleet, J., Palata, K., **Prather, R.**, “Constitutive Analyses of Human

Pleura Tissue Properties", IMSH2017 – Society for Simulation in Healthcare Research Summit, January 27-28, 2017.

Prather, R., Ni, M., Kassab, A., Divo, E., and DeCampli, W.M.., "Multiscale Computational Fluid Dynamics Assessment of Post-LVAD Implantation to Reduce Stroke", BMES-2017, October 11-14, 2017 (Abstract and Poster).

Prather, R., Seligson, J., Ni, M., Kassab, A., Divo, E., and DeCampli, W.M.., "Patient Specific Assessment of Critical Embolization Rates in the Hybrid Norwood Procedure", BMES-2017, October 11-14, 2017 (Abstract and Oral Presentation).

Ni, M., **Prather, R.**, Kassab, A., Divo, E., and DeCampli, W.M.., "Computational Investigation of a Self-Powered Fontan Circulation", BMES-2017, October 11-14, 2017.

Publications

Prather, Ray O et al. "Multi-Scale Pulsatile CFD Modeling of Thrombus Transport In A Patient-Specific LVAD Implantation". *International Journal of Numerical Methods for Heat & Fluid Flow* 27.5 (2017), Vol. 27, No. 5, pp. 1022-1039.

Ray Prather, **Error! Bookmark not defined.**Marcus Ni, Eduardo Divo, Alain Kassab, and William DeCampli. Pulsatile Multi-Scale Fluid Structure Interaction Modeling for Optimal Left Ventricular Assist Device Implantation. *3rd Thermal and Fluids Engineering Conference*, March 4-7, 2018, Fort Lauderdale, Florida.

Marcus Ni, **Ray Prather**, Kyle Beggs, Giovanna Rodriguez, Rachel Quinn, Eduardo Divo, Mark Fogel, Alain Kassab, and William DeCampli. Computational Investigation of Patient-Specific Self-Powered Fontan Circulations. *3rd Thermal and Fluids Engineering Conference*, March 4-7, 2018, Fort Lauderdale, Florida.

Ni, M., **Prather, R.**, Rodriguez, G., Quinn, R., Divo, E., Fogel, M., Kassab, A. and DeCampli, W. (2018). Computational Investigation of a Self-Powered Fontan Circulation. *Cardiovascular Engineering and Technology*, published online Feb. 20, 2018, https://doi.org/10.1007/s13239-018-0342-5.

Prather, R., Seligson, J., Ni, M., Divo, E., Kassab, A. and DeCampli, W. (2018). Patient-Specific Multiscale Computational Fluid Dynamics Assessment Of Embolization Rates In The Hybrid Norwood: Effects of Size and Placement of the Reverse Blalock-Taussig Shunt . *Canadian Journal of Physiology and Pharmacology*. (under review)

APPENDIX A: CODES

Matlab Script for blood model curve fitting

```
% This code is meant to fit Carreau-Yasuda NonNewtonian fluid
model and
% compute the required coefficient for StarCCM+ simulations
% given a viscosity-shear-rate curve for various Hermatocrit
values

% First: import data
table = xlsread('Blood Data.xlsx');

% Second: state percentage hermatocrit percentage (based on
Manning Paper)
% - 1 = 20%
% - 2 = 40%
% - 3 = 60%
hermatocritPercentage = 2;

if (hermatocritPercentage == 1)
    H = table(:,1:2);
elseif (hermatocritPercentage == 2)
    H = table(:,3:4);
elseif (hermatocritPercentage == 3)
    H = table(:,5:6);
end

% Third: extrapolated data fitting
x = H(:,1);
y = H(:,2);

% Carreau-Yasuda model: 3 variables (a=2, n=-1/3)
modelfun = @(b,x)b(1)+(b(2)-b(1))./((1+(b(3).*x).^(2)).^((1/3)));

% Initial guesses
beta0 = [5 18.5 1.54];

% Solver
mdl = NonLinearModel.fit(x,y,modelfun,beta0);
```

Job Submission batch file

```
#$ -cwd
#$ -l mem_free=3G

#$-q all.q@compute-2-4.local,all.q@compute-2-
2.local,all.q@compute-2-1.local,all.q@compute-2-
0.local,all.q@compute-0-17.local,all.q@compute-2-
3.local,all.q@compute-1-16.local

#$ -pe mpich-rr 112
rm ../Abaqus/abaqus_v6.env
##module load /share/apps/abaqus/Commands/abq6133
##echo -n "mp_host_list=[" > abaqus_v6.env

starccm+ -np 105,7 -batchsystem sge -rsh ssh -server -collab
LVAD_Unsteady_CO_4-1_shift_up_FSI_v12@7.50000e-01.sim

##starccm+ -batchsystem sge -server -collab LVAD_Unsteady_CO_4-
1_shift_up_FSI_v12@7.50000e-01.sim

##starccm+ -batchsystem sge -server -collab LVAD_Unsteady_CO_4-
1_shift_up_FSI_v12@7.50000e-01.sim
##starccm+ -batchsystem sge -server -collab -cpubind off -np
28,12 LVAD_Unsteady_CO_4-1_shift_up_FSI_OverSetMesh_v2@7.50000e-
01.sim
```

APPENDIX B: TABLES

Table 13 - Non-Newtonian blood model data.

20% H		40% H		60% H	
Shear Rate [1/s]	Viscosity [cP]	Shear Rate [1/s]	Viscosity [cP]	Shear Rate [1/s]	Viscosity [cP]
187.50	2.79	187.50	4.59	187.50	7.70
143.91	2.87	143.91	4.67	143.91	7.95
110.26	2.87	109.94	4.75	110.26	8.28
84.94	2.87	84.94	4.84	84.94	8.52
65.06	2.95	65.06	4.92	65.06	8.93
50.00	2.87	50.00	5.08	50.00	9.51
38.14	2.87	38.14	5.25	37.82	10.00
29.17	2.87	29.17	5.41	29.17	10.49
22.44	2.95	22.44	5.66	22.44	11.07
17.31	2.95	17.63	5.74	17.31	11.72
13.14	3.11	13.14	5.90	13.14	12.46
10.26	3.20	10.26	6.07	9.94	13.36
7.69	3.20	7.69	6.39	7.69	14.18
6.41	3.28	6.09	6.80	6.09	15.16
4.81	3.36	4.81	7.21	4.81	16.31
3.53	3.44	3.53	7.54	3.53	17.38
2.24	3.52	2.24	7.95	2.88	18.11
0.96	3.52	1.28	8.20	1.92	18.85

Table 14 - Linear elastic material modal analysis data.

Mode	Frequency		Mode	Frequency	
	[Cycles/s]	[rad/s]		[Cycles/s]	[rad/s]
1	5.57	34.97	31	77.85	489.17
2	12.50	78.57	32	81.89	514.51
3	13.58	85.32	33	83.81	526.61
4	14.23	89.41	34	85.80	539.09
5	16.83	105.75	35	87.08	547.14
6	19.16	120.38	36	92.35	580.25
7	24.20	152.05	37	94.49	593.69
8	27.33	171.72	38	96.80	608.19
9	31.84	200.09	39	100.75	633.02
10	33.69	211.67	40	102.21	642.23
11	36.41	228.77	41	103.28	648.93
12	39.05	245.38	42	105.49	662.79
13	40.30	253.24	43	107.76	677.06
14	41.44	260.37	44	108.94	684.47
15	43.23	271.64	45	113.03	710.18
16	48.33	303.68	46	113.97	716.09
17	51.78	325.32	47	114.59	719.98
18	53.91	338.72	48	115.03	722.77
19	56.67	356.09	49	119.77	752.56
20	57.74	362.80	50	120.42	756.59
21	61.15	384.21	51	122.72	771.04
22	62.40	392.09	52	125.75	790.12
23	63.62	399.71	53	126.32	793.72
24	65.90	414.07	54	127.62	801.88
25	70.12	440.55	55	130.47	819.78
26	70.79	444.78	56	131.25	824.65
27	73.79	463.65	57	136.37	856.84
28	75.70	475.64	58	136.80	859.51
29	76.54	480.90	59	138.72	871.60
30	77.57	487.37	60	141.09	886.51

Table 15 - Anisotropic material modal analysis data.

Mode	Frequency		Mode	Frequency	
	[Cycles/s]	[rad/s]		[Cycles/s]	[rad/s]
1	1.98	12.41	31	25.62	160.99
2	3.86	24.28	32	25.74	161.75
3	4.32	27.14	33	26.48	166.36
4	4.60	28.87	34	28.97	182.05
5	4.69	29.44	35	30.35	190.69
6	6.33	39.77	36	31.68	199.08
7	7.71	48.46	37	32.15	201.98
8	8.91	56.01	38	32.84	206.32
9	9.82	61.68	39	33.25	208.93
10	11.30	71.01	40	34.16	214.66
11	11.57	72.69	41	34.57	217.19
12	11.97	75.20	42	35.68	224.20
13	12.56	78.90	43	37.11	233.14
14	13.14	82.54	44	38.02	238.91
15	13.73	86.28	45	38.10	239.39
16	14.18	89.07	46	38.61	242.62
17	15.54	97.67	47	38.78	243.67
18	16.34	102.68	48	39.05	245.38
19	17.27	108.49	49	39.91	250.74
20	17.46	109.70	50	40.75	256.03
21	18.58	116.75	51	41.18	258.72
22	19.64	123.39	52	41.45	260.46
23	20.45	128.48	53	42.29	265.73
24	21.01	132.01	54	42.73	268.51
25	21.24	133.44	55	42.94	269.79
26	21.87	137.41	56	43.94	276.07
27	22.68	142.48	57	44.15	277.41
28	23.23	145.98	58	44.49	279.52
29	23.75	149.21	59	45.46	285.61
30	24.91	156.54	60	45.71	287.18

APPENDIX C: FIGURES

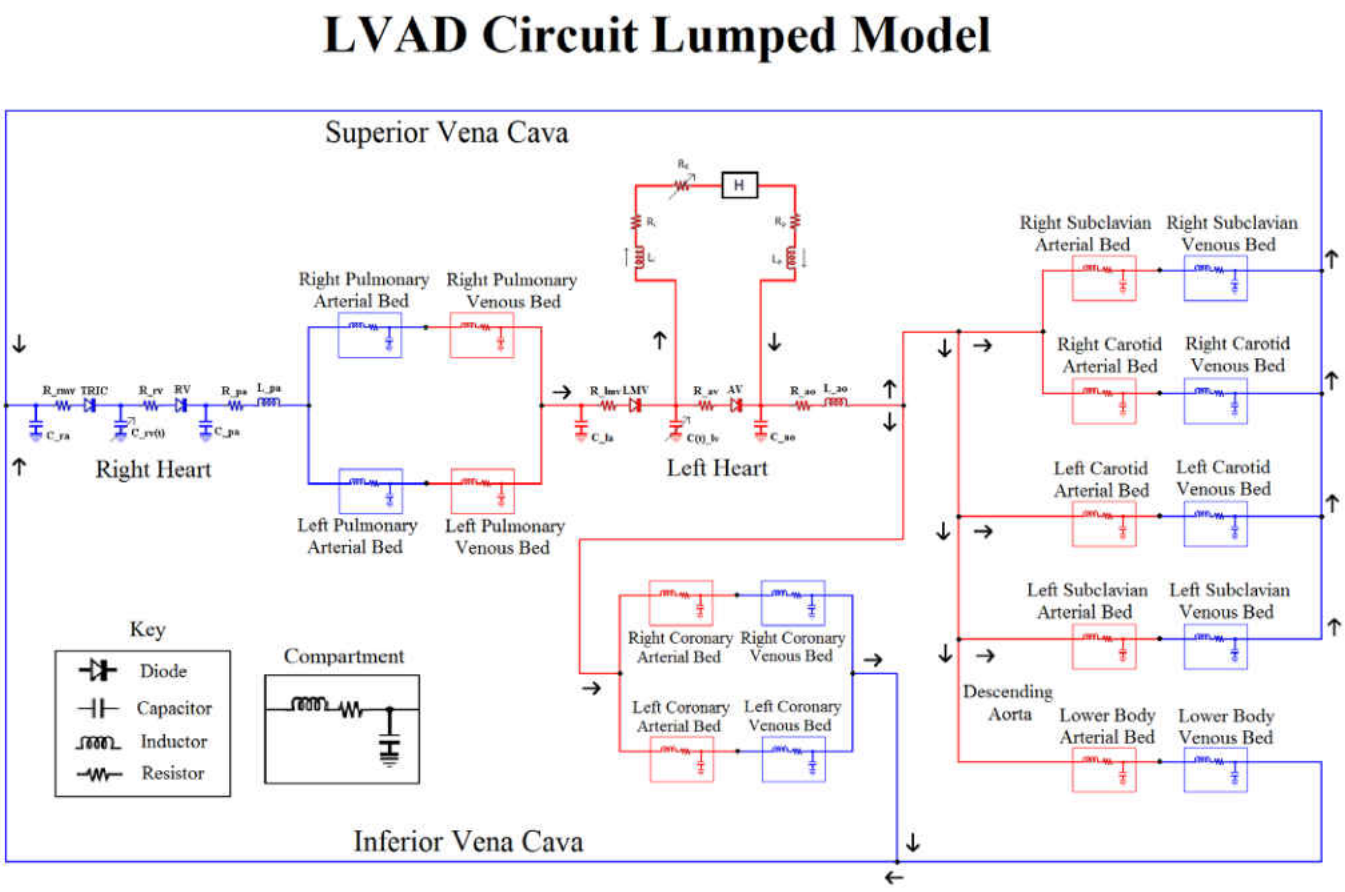

Figure 79 - Full LVAD circuit schematic.

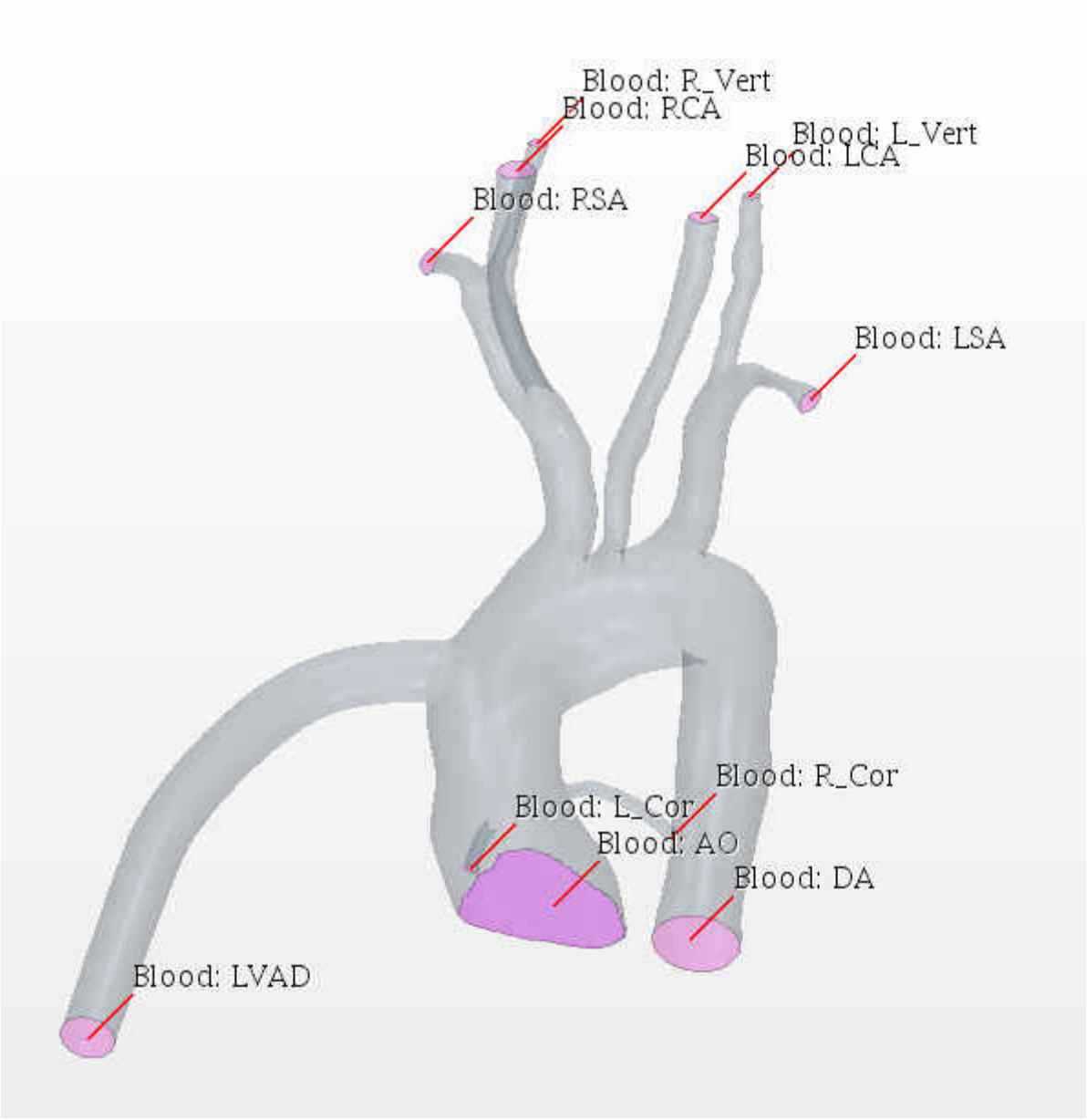

Figure 80 - Fluid domain with labelled boundaries (AO=Ascending Aorta, LVAD=Left Ventricular Assist Device inflow cannula, L_Cor=Left Coronary Artery, R_Cor=Right Coronary Artery, DA=Descending Aorta, RSA=Right Subclavian Artery, RCA=Right Carotid Artery, R_Vert=Right Vertebral Artery, LCA=Left Carotid Artery, L_Vert=Lef Vertebral Artery and LSA=Left Subclavian Artery).

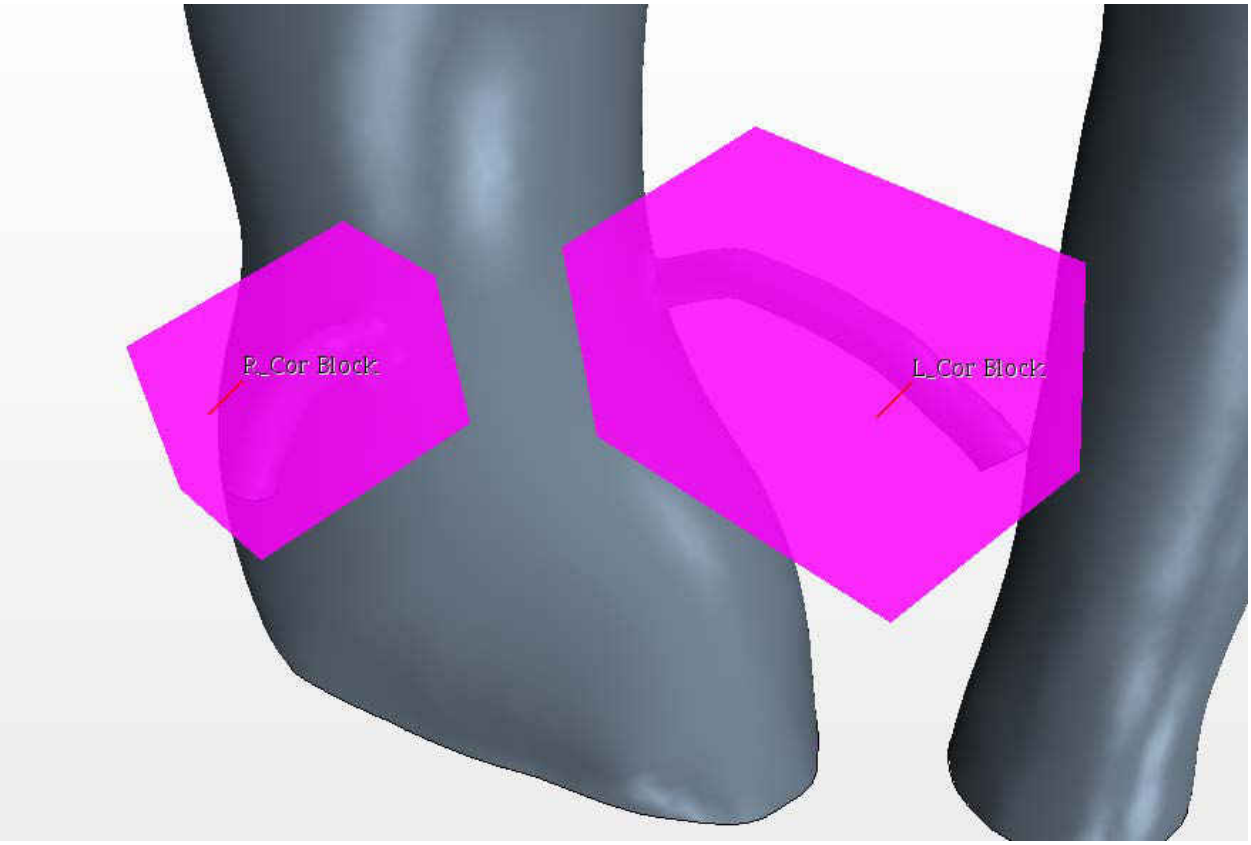

Figure 81 - Volumetric mesh refinement around the coronaries.

APPENDIX D: INPUT FILES

```
*Heading
 Hyperelastic model of aortic wall for FSI coupling
** Job name: Aortic_Wall-Job Model name: Aortic_Arch
** Generated by: Abaqus/CAE 6.14-2
*Preprint, echo=NO, model=NO, history=NO, contact=NO
**
** PARTS
**
*Part, name=Aortic_Wall
*End Part
**
**
** ASSEMBLY
**
*Assembly, name=Assembly
**
*Instance, name=Aortic_Wall-1, part=Aortic_Wall
*Node
**
OMITTED (element vertex coordinates)
**
*End Assembly
**
** MATERIALS
**
*Material, name=Aortic_Wall
*Density
 1.08e-09,
**
**OPTION 1: HYPERELASTIC MODEL
**
**Anisotropic Hyperelastic, holzapfel, local direction=2
** 0.0085, 1e-06,  0.56, 16.21,  0.18
**
**OPTION 2: LINEAR ELASTIC MODEL
**
*Material, name=Aortic_Wall_LinearElastic
*Damping
*Density
 1.08e-09,
*Elastic
 0.4, 0.48
```

```
**
** INTERACTION PROPERTIES
**
*Surface Interaction, name=IntProp-1
1.,
*Friction
0.,
*Surface Behavior, pressure-overclosure=HARD
**
** INTERACTIONS
**
** Interaction: Int-1
*Contact Pair, interaction=IntProp-1, type=SURFACE TO SURFACE
OUTER_WALL,
** ----------------------------------------------------------------
**
** STEP: Step-1
**
**
**Step, name=Step-2, nlgeom=YES, extrapolation=PARABOLIC, inc=1000000
**Static, stabilize, factor=0.002, allsdtol=0, continue=NO
**6.25e-07, 2.25, 1e-07, 6.25e-06
**
*Step, name=Step-1, nlgeom=YES, inc=1000000, amplitude=RAMP,
extrapolation=VELOCITY PARABOLIC
*Dynamic,alpha=-0.3,haftol=1e+06,application=MODERATE DISSIPATION,initial=NO
6.25e-05,2.25,1e-08,0.000625
**
** BOUNDARY CONDITIONS
**
**OPTION 1: AXISYMMETRIC BC
**
** Name: AO_1 Type: Symmetry/Antisymmetry/Encastre
*Boundary
AO, ZSYMM
** Name: DA_1 Type: Symmetry/Antisymmetry/Encastre
*Boundary
DA, ZSYMM
** Name: LCA_1 Type: Symmetry/Antisymmetry/Encastre
*Boundary
LCA, ZSYMM
** Name: LSA_1 Type: Symmetry/Antisymmetry/Encastre
*Boundary
LSA, ZSYMM
** Name: LVAD_1 Type: Symmetry/Antisymmetry/Encastre
```

```
*Boundary
LVAD, PINNED
** Name: L_COR Type: Displacement/Rotation
*Boundary
L_COR, 4, 4
L_COR, 5, 5
L_COR, 6, 6
** Name: L_VERT_1 Type: Symmetry/Antisymmetry/Encastre
*Boundary
L_VERT, ZSYMM
** Name: RCA_1 Type: Symmetry/Antisymmetry/Encastre
*Boundary
RCA, ZSYMM
** Name: RSA_1 Type: Symmetry/Antisymmetry/Encastre
*Boundary
RSA, ZSYMM
** Name: R_COR_1 Type: Symmetry/Antisymmetry/Encastre
*Boundary
R_COR, ZSYMM
** Name: R_VERT_1 Type: Symmetry/Antisymmetry/Encastre
*Boundary
R_VERT, ZSYMM
**
**OPTION 2: CARTESIAN BC
**
** Name: AO Type: Displacement/Rotation
*Boundary
AO, 3, 3
AO, 4, 4
AO, 5, 5
AO, 6, 6
** Name: DA Type: Displacement/Rotation
*Boundary
DA, 3, 3
DA, 4, 4
DA, 5, 5
DA, 6, 6
** Name: LCA Type: Displacement/Rotation
*Boundary
LCA, 3, 3
LCA, 4, 4
LCA, 5, 5
LCA, 6, 6
** Name: LSA Type: Displacement/Rotation
*Boundary
```

LSA, 3, 3
LSA, 4, 4
LSA, 5, 5
LSA, 6, 6
** Name: LVAD Type: Displacement/Rotation
*Boundary
LVAD, 1, 1
LVAD, 2, 2
LVAD, 3, 3
LVAD, 4, 4
LVAD, 5, 5
LVAD, 6, 6
** Name: L_COR Type: Displacement/Rotation
*Boundary
L_COR, 4, 4
L_COR, 5, 5
L_COR, 6, 6
** Name: L_VERT Type: Displacement/Rotation
*Boundary
L_VERT, 3, 3
L_VERT, 4, 4
L_VERT, 5, 5
L_VERT, 6, 6
** Name: RCA Type: Displacement/Rotation
*Boundary
RCA, 3, 3
RCA, 4, 4
RCA, 5, 5
RCA, 6, 6
** Name: RSA Type: Displacement/Rotation
*Boundary
RSA, 3, 3
RSA, 4, 4
RSA, 5, 5
RSA, 6, 6
** Name: R_COR Type: Displacement/Rotation
*Boundary
R_COR, 3, 3
R_COR, 4, 4
R_COR, 5, 5
R_COR, 6, 6
** Name: R_VERT Type: Displacement/Rotation
*Boundary
R_VERT, 3, 3
R_VERT, 4, 4

```
R_VERT, 5, 5
R_VERT, 6, 6
**
** LOADS
**
** Name: External_Pressure   Type: Pressure
*Dsload
Aortic_Wall-1.OUTER_WALL, P, 0.006666
**
** OUTPUT REQUESTS
**
*Restart, write, frequency=0
**
** FIELD OUTPUT: F-Output-1
**
*Output, field, variable=PRESELECT, time interval=0.00125
**
** FIELD OUTPUT: F-Output-2
**
*Output, field, variable=PRESELECT
**
** HISTORY OUTPUT: H-Output-1
**
*Output, history, variable=PRESELECT
**
*Co-simulation, name=Aortic_Wall-Job, program=MULTIPHYSICS
*Co-simulation Region, type=SURFACE, export
ASSEMBLY_FSI_INTERFACE, U
*Co-simulation Region, type=SURFACE, import
ASSEMBLY_FSI_INTERFACE, CF
**
*End Step
```

Analysis step is modified to:

*Step, name=Step-1, nlgeom=NO, perturbation
*Frequency, eigensolver=AMS, normalization=mass, acoustic coupling=off, damping projection=on
70, , 1000., , , ,

APPENDIX E: FULL LPM EQUATIONS

Current Auxiliary Equations

$$i_1(y) = y_4$$

$$i_2(y) = \frac{y_5 - y_6}{R_{la}} hev(y_5, y_6)$$

$$i_3(y) = \frac{y_6 - y_8}{R_{lv}} hev(y_6, y_8)$$

$$i_5(y) = \frac{y_{40} - y_{49}}{R_{dsb}}$$

$$i_6(y) = \frac{y_{43} - y_{49}}{R_{dcb}}$$

$$i_7(y) = \frac{y_{46} - y_{49}}{R_{dvb}}$$

$$i_8(y) = \frac{y_{48} - y_{49}}{R_{ivb}}$$

$$i_9(y) = \frac{y_{49} - y_{50}}{R_{ra}} hev(y_{49}, y_{50})$$

$$i_{10}(y) = \frac{y_{50} - y_1}{R_{rv}} hev(y_{50}, y_1)$$

$$i_{11}(y) = \frac{y_{37} - y_{49}}{R_{corvb}}$$

$$I_{in}(y) = i_5(y) + i_6(y) + i_7(y) + i_8(y) + i_{11}(y)$$

$$where \quad hev(x1, x2) = \begin{cases} 1 & if \quad x1 - x2 > 0 \\ 0 & if \quad x1 - x2 \leq 0 \end{cases} \quad is\ a\ heaviside\ step\ function$$

Voltage Auxiliary Equations

$$v_1(y) = \frac{i_7(y) + \left(\frac{y_1}{R_{rpa}} + \frac{y_3}{R_{lpa}}\right)}{\frac{1}{R_{rpa}} + \frac{1}{R_{lpa}}}$$

$$v_{vad}(y) = y_7 R_{star}(y_6, x1) + y_6$$

CFD Voltage Auxiliary Equations

$$v_{cfd\_1}(y) = y_8 - (y_{10} + y_{11} + y_{12})R_{ao}$$

$$v_{cfd\_2}(y) = v_{cfd\_1}(y) - (y_{14} - y_{13})R_{ia\_cor}$$

$$v_{cfd\_3}(y) = v_{cfd\_2}(y) - (y_{15} + y_{20})R_{ia\_vad}$$

$$v_{cfd\_4}(y) = v_{cfd\_3}(y) - (y_{17} + y_{16})R_{rca\_ia}$$

$$v_{cfd\_5}(y) = v_{cfd\_4}(y) - (y_{18} + y_{19})R_{ia\_rsa}$$

$$v_{cfd\_6}(y) = v_{cfd\_3}(y) - (y_{21} + y_{22})R_{lca\_ia}$$

$$v_{cfd\_7}(y) = v_{cfd\_6}(y) - (y_{26} + y_{23})R_{lsa\_lca}$$

$$v_{cfd\_8}(y) = v_{cfd\_7}(y) - (y_{24} + y_{25})R_{da\_lsa}$$

Circuit ODEs

$$y_1 = \frac{1}{C_{ap}}(i_{10}(y) - y_2)$$

$$y_2 = \frac{1}{L_{ap}}\left(y_1 - y_2 R_{ap} - y_5\right)$$

$$y_3 = \frac{1}{C_{vp}}(y_2 - y_4)$$

$$y_4 = \frac{1}{L_{vp}}\left(y_3 - y_4 R_{vp} - y_5\right)$$

$$y_5 = \frac{1}{C_{la}}\left(y_4 - i_2(y)\right)$$

$$y_6 = \frac{1}{C_{lv}(t)}(i_2(y) - i_3(y) - y_6 dC_{lv}(t) - y_7)$$

$$y_7 = VAD_{cond}\frac{1}{L_{star}}\left(y_6 - y_{29} - R_{star}(y_6, x1)y_7 + \gamma\frac{i_{vad}}{y_7}\right)$$

$$y_8 = \frac{1}{C_{ao}}(i_3(y) - y_9)$$

$$y_9 = \frac{1}{L_{ao}}\left(y_8 - y_9 R_{ao} - v_{cfd\_1}(y)\right)$$

$$y_{10} = \frac{1}{L_{cr}}\left(v_{cfd\_1}(y) - y_{10}R_{cr} - y_{27}\right)$$

$$y_{11} = \frac{1}{L_{cl}}\left(v_{cfd\_1}(y) - y_{11}R_{cl} - y_{28}\right)$$

$$y_{12} = \frac{1}{L_{ia\_cor}}\left(v_{cfd\_1}(y) - y_{12}R_{ia\_cor} - v_{cfd\_2}(y)\right)$$

$$y_{13} = VAD_{cond}\frac{1}{L_{cannula}}\left(y_{29} - y_{13}R_{cannula} - v_{cfd\_2}(y)\right)$$

$$y_{14} = \frac{1}{L_{ia\_vad}}\left(v_{cfd\_2}(y) - y_{14}R_{ia\_vad} - v_{cfd\_3}(y)\right)$$

$$y_{15} = \frac{1}{L_{rca\_ia}}\left(v_{cfd\_3}(y) - y_{15}R_{rca\_ia} - v_{cfd\_4}(y)\right)$$

$$y_{16} = \frac{1}{L_{rca}}\left(v_{cfd\_4}(y) - y_{16}R_{rca} - y_{30}\right)$$

$$y_{17} = \frac{1}{L_{ia\_rsa}}\left(v_{cfd\_4}(y) - y_{17}R_{ia\_rsa} - v_{cfd\_5}(y)\right)$$

$$y_{18} = \frac{1}{L_{r\_vert}}\left(v_{cfd\_5}(y) - y_{18}R_{r\_vert} - y_{31}\right)$$

$$y_{19} = \frac{1}{L_{rsa}}\left(v_{cfd\_5}(y) - y_{19}R_{rsa} - y_{32}\right)$$

$$y_{20} = \frac{1}{L_{lca\_ia}}\left(v_{cfd\_3}(y) - y_{20}R_{lca\_ia} - v_{cfd\_6}(y)\right)$$

$$y_{21} = \frac{1}{L_{lca}}\left(v_{cfd\_6}(y) - y_{21}R_{lca} - y_{33}\right)$$

$$y_{22} = \frac{1}{L_{lsa\_lca}}\left(v_{cfd\_6}(y) - y_{22}R_{lsa\_lca} - v_{cfd\_7}(y)\right)$$

$$y_{23} = \frac{1}{L_{da\_lsa}}\left(v_{cfd\_7}(y) - y_{23}R_{da\_lsa} - v_{cfd\_8}(y)\right)$$

$$y_{24} = \frac{1}{L_{l\_vert}}\left(v_{cfd\_8}(y) - y_{24}R_{l\_vert} - y_{34}\right)$$

$$y_{25} = \frac{1}{L_{lsa}}\left(v_{cfd\_8}(y) - y_{25}R_{lsa} - y_{35}\right)$$

$$y_{26} = \frac{1}{L_{da}}\left(v_{cfd\_7}(y) - y_{26}R_{da} - y_{36}\right)$$

$$y_{27} = \frac{1}{C_{rcorab}}\left(y_{10} - \frac{y_{27} - y_{37}}{R_{rcora}(t)}\right)$$

$$y_{28} = \frac{1}{C_{lcorab}}\left(y_{11} - \frac{y_{28} - y_{37}}{R_{lcora}(t)}\right)$$

$$y_{29} = \frac{1}{C_{cannula}}\left(y_7 - y_{13}\right)$$

$$y_{30} = \frac{1}{C_{rcb}}\left(y_{16} - y_{41}\right)$$

$$y_{31} = \frac{1}{C_{rvb}}\left(y_{18} - y_{44}\right)$$

$$y_{32} = \frac{1}{C_{rsb}}\left(y_{19} - y_{28}\right)$$

$$y_{33} = \frac{1}{C_{lcb}}\left(y_{21} - y_{42}\right)$$

$$y_{34} = \frac{1}{C_{lvb}}(y_{24} - y_{45})$$

$$y_{35} = \frac{1}{C_{lsb}}(y_{25} - y_{39})$$

$$y_{36} = \frac{1}{C_{da\_b}}(y_{26} - y_{47})$$

$$y_{37} = \frac{1}{C_{corvb}}\left(\frac{y_{27} - y_{37}}{R_{rcora}(t)} + \frac{y_{28} - y_{37}}{R_{lcora}(t)} - \frac{y_{37} - y_{49}}{R_{corvb}}\right)$$

$$y_{38} = \frac{1}{L_{rsb}}(y_{32} - y_{38}R_{rsb} - y_{40})$$

$$y_{39} = \frac{1}{L_{lsb}}(y_{35} - y_{39}R_{lsb} - y_{40})$$

$$y_{40} = \frac{1}{C_{dsb}}\left(y_{38} + y_{39} - i_5(y)\right)$$

$$y_{41} = \frac{1}{L_{rcb}}(y_{30} - y_{41}R_{rcb} - y_{43})$$

$$y_{42} = \frac{1}{L_{lcb}}(y_{33} - y_{42}R_{lcb} - y_{43})$$

$$y_{43} = \frac{1}{C_{dcb}}\left(y_{41} + y_{42} - i_6(y)\right)$$

$$y_{44} = \frac{1}{L_{rvb}}(y_{31} - y_{44}R_{rvb} - y_{46})$$

$$y_{45} = \frac{1}{L_{lvb}}(y_{34} - y_{45}R_{lvb} - y_{46})$$

$$y_{46} = \frac{1}{C_{dvb}}\left(y_{44} + y_{45} - i_7(y)\right)$$

$$y_{47} = \frac{1}{L_{da\_b}}\left(y_{36} - y_{47}R_{da\_b} - y_{48}\right)$$

$$y_{48} = \frac{1}{C_{ivb}}\left(y_{47} - i_8(y)\right)$$

$$y_{49} = \frac{1}{C_{ra}}\left(I_{in}(y) - i_9(y)\right)$$

$$y_{50} = \frac{1}{C_{rv}(t)}\left(i_9(y) - i_{10}(y) - y_{50}dC_{rv}(t)\right)$$

$$where \quad dC(t) = \frac{C(t+\Delta t) - C(t)}{\Delta t} \quad and\ \Delta t = 10^{-6}$$

$$(forward\ finite\ difference\ of\ time - varying\ capacitors)$$

REFERENCES

[1] Schmid, C., Weyand, M., Nabavi, D., Hammel, D., Deng, M., Ringelstein, E. and Scheld, H. (1998). Cerebral and Systemic Embolization During Left Ventricular Support With the Novacor N100 Device. *The Annals of Thoracic Surgery*, 65(6), pp.1703-1710.

[2] Tsukui, H., Abla, A., Teuteberg, J., McNamara, D., Mathier, M., Cadaret, L. and Kormos, R. (2007). Cerebrovascular accidents in patients with a ventricular assist device. *The Journal of Thoracic and Cardiovascular Surgery*, 134(1), pp.114-123.

[3] Osorio, A., Osorio, R., Ceballos, A., Tran, R., Clark, W., Divo, E., Argueta-Morales, I., Kassab, A. and DeCampli, W. (2013). Computational fluid dynamics analysis of surgical adjustment of left ventricular assist device implantation to minimise stroke risk. *Computer Methods in Biomechanics and Biomedical Engineering*, 16(6), pp.622-638.

[4] Argueta-Morales, I., Tran, R., Clark, W., Divo, E., Kassab, A. and DeCampli, W. (2010). Use of computational fluid dynamics (CFD) to tailor the surgical implantation of a ventricular assist device (VAD): A patient-specific approach to reduce risk of stroke. *Journal of the American College of Surgeons*, 211(3), pp. S26-S27.

[5] Argueta-Morales, I.R., Tran, R., Ceballos, A., Osorio, R., Clark, W., Divo, E., Kassab, A., William M. DeCampli, “Mathematical modeling of patient-specific ventricular assist device implantation to reduce particulate embolization rate to cerebral vessels”, ASME Journal of Biomechanical Engineering, 2014, 136(7).

[6] Nguyen, T., Argueta-Morales, I., Guimond, S., Clark, W., Ceballos, A., Osorio, R., Divo, E., De Campli, W. and Kassab, A. (2015). Computational analysis of pediatric ventricular assist device implantation to decrease cerebral particulate embolization. *Computer Methods in Biomechanics and Biomedical Engineering*, 19(7), pp.789-799.

[7] Rothenburger, Markus et al. Treatment Of Thrombus Formation Associated With The Micromed Debakey VAD Using Recombinant Tissue Plasminogen Activator. *Circulation*, vol 106, no. 12, 2002, pp. 189-192.

[8] Starling, R., Moazami, N., Silvestry, S., Ewald, G., Rogers, J., Milano, C., Rame, J., Acker, M., Blackstone, E., Ehrlinger, J., Thuita, L., Mountis, M., Soltesz, E., Lytle, B. and Smedira, N. (2014). Unexpected Abrupt Increase in Left Ventricular Assist Device Thrombosis. *New England Journal of Medicine*, 370(1), pp.33-40.

[9] Kirklin, J., Naftel, D., Kormos, R., Pagani, F., Myers, S., Stevenson, L., Acker, M., Goldstein, D., Silvestry, S., Milano, C., Baldwin, J., Pinney, S., Eduardo Rame, J. and Miller, M. (2014). Interagency Registry for Mechanically Assisted Circulatory Support (INTERMACS) analysis of pump thrombosis in the HeartMate II left ventricular assist device. *The Journal of Heart and Lung Transplantation*, 33(1), pp.12-22.

[10] Taghavi, S., Ward, C., Jayarajan, S., Gaughan, J., Wilson, L. and Mangi, A. (2013). Surgical Technique Influences HeartMate II Left Ventricular Assist Device Thrombosis. *The Annals of Thoracic Surgery*, 96(4), pp.1259-1265.

[11] Beck, Debra L., "Device Positioning May Be Culprit behind Post-LVAD Pump Thrombosis", Thoracic Surgery News. Frontline Medical Communications Inc., 11 July 2014. Web. 8 Aug. 2014.

[12] Acharya, D., Loyaga-Rendon, R., Morgan, C.J., Sands K.A., Pamboukian, S.V., Rajapreyar I., Holman, W.L., Kirklin, J.K., and Tallaj, J.A., INTERMACS Analysis of Stroke During Support With Continuous-Flow Left Ventricular Assist Devices: Risk Factors and Outcomes, JACC Heart Fail. 2017 Oct; 5(10):703-711. doi: 10.1016/j.jchf.2017.06.014

[13] Prather, R.O., A Multi-Scale CFD Analysis of Patient-Specific Geometries to Tailor LVAD Cannula Implantation Under Pulsatile Flow Conditions: an investigation aimed at reducing stroke incidence in LVADs, University of Central Florida, MSME Thesis, 2015.

[14] Freed BH, Jeevanandam V, Jolly N. “Aortic root and valve thrombosis after implantation of a left ventricular assist device”. *J Invasive Cardiol*. 2011;23(4):E63-65.

[15] Hansen, K. and Shadden, S. (2015). A reduced-dimensional model for near-wall transport in cardiovascular flows. *Biomechanics and Modeling in Mechanobiology*, 15(3), pp.713-722.

[16] Good, B., Deutsch, S. and Manning, K. (2015). Hemodynamics in a Pediatric Ascending Aorta Using a Viscoelastic Pediatric Blood Model. *Annals of Biomedical Engineering*, 44(4), pp.1019-1035.

[17] Takizawa, Kenji, Yuri Bazilevs, and Tayfun E. Tezduyar. "Space–Time And ALE-VMS Techniques For Patient-Specific Cardiovascular Fluid–Structure Interaction

Modeling". *Archives of Computational Methods in Engineering* 19.2 (2012): 171-225. Web.

[18] Gasser, T., Ogden, R. and Holzapfel, G. (2006). Hyperelastic modelling of arterial layers with distributed collagen fiber orientations. *Journal of The Royal Society Interface*, 3(6), pp.15-35.

[19] Holzapfel, G. A., Gasser, T. C., & Ogden, R. W. (2000). A new constitutive framework for arterial wall mechanics and a comparative study of material models. J. Elasticity, 61:1-48.

[20] Prather, Ray O et al. "Multi-Scale Pulsatile CFD Modeling of Thrombus Transport In A Patient-Specific LVAD Implantation". *International Journal of Numerical Methods for Heat & Fluid Flow* 27.5 (2017), Vol. 27, No. 5, pp. 1022-1039.

[21] Faragallah, G., Wang, Y., Divo, E. and Simaan, M. (2012). “A new control system for left ventricular assist devices based on patient-specific physiological demand”. *Inverse Problems in Science and Engineering*, 20(5), pp.721-734.

[22] Ferziger, Joel H, and M Perić. *Computational Methods For Fluid Dynamics*. Beijing: World Publishing Corporation, 2012. Print.

[23] Causin, P., Gerbeau, J. and Nobile, F. (2005). Added-mass effect in the design of partitioned algorithms for fluid–structure problems. *Computer Methods in Applied Mechanics and Engineering*, 194(42-44), pp.4506-4527.

[24] Idelsohn, S., Del Pin, F., Rossi, R. and Oñate, E. (2009). Fluid-structure interaction problems with strong added-mass effect. *International Journal for Numerical Methods in Engineering*, 80(10), pp.1261-1294.

[25] Crosetto, P., Reymond, P., Deparis, S., Kontaxakis, D., Stergiopulos, N. and Quarteroni, A. (2011). Fluid–structure interaction simulation of aortic blood flow. *Computers & Fluids*, 43(1), pp.46-57.

[26] Khamdaeng, T., Luo, J., Vappou, J., Terdtoon, P. and Konofagou, E. (2012). Arterial stiffness identification of the human carotid artery using the stress–strain relationship in vivo. *Ultrasonics*, 52(3), pp.402-411.

[27] ABAQUS, V6.12 .. (n.d.). Abaqus Analysis User's Manual: 22.5.3 Anisotropic hyperelastic behavior.

[28] Lantz, Jonas, Johan Renner, And Matts Karlsson. Wall Shear Stress In A Subject Specific Human Aorta — Influence Of Fluid-Structure Interaction. *International Journal Of Applied Mechanics* 03.04 (2011): 759-778. Web.

[29] Weisbecker, Hannah et al. Layer-Specific Damage Experiments And Modeling Of Human Thoracic And Abdominal Aortas With Non-Atherosclerotic Intimal Thickening. *Journal Of The Mechanical Behavior Of Biomedical Materials*, vol 12, 2012, pp. 93-106. *Elsevier BV*, doi:10.1016/j.jmbbm.2012.03.012.

[30] "Abaqus 6.13 Documentation". *Dsk.ippt.pan.pl*. N.p., 2017. Web. 6 June 2017.

[31] "STAR-CCM+11.04.010-R8". N.p., 2017. Web. 6 June 2017.

[32] "Getting Started With Abaqus: Interactive Edition (6.14)". *Abaqus.software.polimi.it*. N.p., 2017. Web. 6 June 2017.

[33] Devore, Jay L. Probability and Statistics For Engineering And The Sciences. 8th ed. Boston: Cengage Learning, 2010. Print.

[34] Sankaran, S., Esmaily Moghadam, M., Kahn, A., Tseng, E., Guccione, J. and Marsden, A. (2012). Patient-Specific Multiscale Modeling of Blood Flow for

Coronary Artery Bypass Graft Surgery. *Annals of Biomedical Engineering*, 40(10), pp.2228-2242.

[35] Kato, T., Ota, T., Schulze, P., Farr, M., Jorde, U., Takayama, H., Naka, Y., Yamashita, T. and Mancini, D. (2011). Asymmetric Pattern of Cerebrovascular Lesions in Patients After Left Ventricular Assist Device Implantation. *Stroke*, 43(3), pp.872-874.

[36] Chandran, K., Rittgers, S. and Yoganathan, A. (2012). *Biofluid mechanics*. Boca Raton: CRC Press, Taylor & Francis Group.

[37] Holzapfel, G. and Gasser, T. (2001). A viscoelastic model for fiber-reinforced composites at finite strains: Continuum basis, computational aspects and applications. *Computer Methods in Applied Mechanics and Engineering*, 190(34), pp.4379-4403.

[38] Pierce, D., Fastl, T., Rodriguez-Vila, B., Verbrugghe, P., Fourneau, I., Maleux, G., Herijgers, P., Gomez, E. and Holzapfel, G. (2015). A method for incorporating three-dimensional residual stretches/stresses into patient-specific finite element simulations of arteries. *Journal of the Mechanical Behavior of Biomedical Materials*, 47, pp.147-164.

[39] Bustamante, R. and Holzapfel, G. (2010). Methods to compute 3D residual stress distributions in hyperelastic tubes with application to arterial walls. *International Journal of Engineering Science*, 48(11), pp.1066-1082.

[40] Qi, N., Gao, H., Ogden, R., Hill, N., Holzapfel, G., Han, H. and Luo, X. (2015). Investigation of the optimal collagen fibre orientation in human iliac arteries. *Journal of the Mechanical Behavior of Biomedical Materials*, 52, pp.108-119.

[41] Jiu-sheng, R. (2012). Effects of dispersion of fiber orientation on the mechanical property of the arterial wall. *Journal of Theoretical Biology*, 301, pp.153-160.